Design, Development and Characterization of a Hand-Held Radiation Detector for Radio-guided Surgery

by

Muhammed Emin Bedir

A dissertation submitted in partial fulfillment of
the requirements for the degree of

Doctor of Philosophy

(Medical Physics)

at the

UNIVERSITY OF WISCONSIN – MADISON

2020

Date of final oral examination: 01/16/2020

The dissertation is approved by the following members of the Final Oral Committee:

Bruce R. Thomadsen, Ph.D., Professor, Medical Physics

Douglass L. Henderson, Ph.D., Professor, Engineering Physics

Bryan P. Bednarz, Ph.D., Associate Professor, Medical Physics

Oliver Wieben, Ph.D., Associate Professor, Medical Physics

Wesley Culberson, Ph.D., Associate Professor, Medical Physics

Steve Y Cho, MD., Associate Professor, Radiology

I dedicate this dissertation to God Almighty my creator, my strong pillar, my source of inspiration, wisdom, knowledge and understanding Who decrees in the Qur'an as:

……And indeed, he was a possessor of knowledge because of what We had taught him, but most of the people do not know.

[Yusuf,12:68]

Abstract

Surgery to remove breast cancer is performed almost 1,000 times a day in the United States. The current state-of-the-art surgery uses radioactive sources to indicate the center of the tumor and possibly a few points on the periphery as seen on mammography. Since such guidance is very coarse, tumor free margin is not achievable and a re-excision procedure is usually required. This approach provides no information about the margins of the tumor. Better radiation guidance could come from labeling all cancer cells directly with a breast tumor-seeking agent, such as CLR1404. The agent CLR1404 is taken up by breast cancer cells but not normal cells, labeled with radioactive ^{123}I could image the whole tumor not just points. ^{99m}Tc labelled nanoparticles locate sentinel lymph nodes. For the simultaneous detection and identification of photon energies 159 keV from ^{123}I and 141 keV from ^{99m}Tc, a radiation detector with high energy resolution, fine spatial resolution and sufficient sensitivity is required. This study involves the design, development, and characterization of such a handheld radiation detector. Following the design and integration of the detector, the main characteristics of the detector, such as energy resolution, photopeak efficiency and response at different source-to-detector distances were investigated experimentally. Energy resolution of the detector was found to be less than 10 keV (FWHM) at energies below 159 keV, which allowed resolving the radiation from the two radionuclides. Energy spectra of the radioactive sources acquired experimentally were compared to those simulated in Monte Carlo N-Particle Transport Code (MCNP6/X) and good agreement was observed between two curves. The study

is also targeted to give a contribution to the better localization of the SLNs and tumors by designing an optimum collimation geometry for the detector. Based on the simulations and experimental results, it was found out that by having a spatial resolution of 4.28±0.40 mm and sensitivity of 188.61±1.41 cps/MBq at 5cm source-to-detector distance, the collimated detector could meet the necessities of locating the deeply-seated SLNs that requires a detector with fine spatial resolution and adequate sensitivity. In overall; the detector was found to be promising for radio-guided surgery applications.

Acknowledgements

I would like to express the deepest appreciation to my advisor Professor Bruce R. Thomadsen who has the attitude and the substance of a genius: he continually and convincingly conveyed a spirit of adventure in regard to research. Without his guidance and continious help this dissertation would not have been possible.

Dr. Bednarz thank you for co-advising me on this project which was actually brought up by you at the first place. As an international student, I was not able to take the Monte Carlo course because of the possibility that the MCNP license may be delayed. So I tried to learn the program myself. However, your door was always open to me whenever I needed help about the simulations in MCNP.

Dr. Culberson, I have always admired your sincerity and knowledge. You have always treated me like a friend and at the same time you never turned me down whenever I needed help in regard to research and funding. Special thank to you for funding the last two months of my study in which I did not have any financial support elsewhere.

Dr. Henderson, you have been such a great advisor for me during my time in the Department of Nuclear Engineering. It was on your occasion that I switched to the Department of the Medical Physics and met Dr. Thomadsen. I would like to thank you for supporting me at every stage of my studies at the University of Wisconsin-Madison from day one.

Dr.Weiben, our first contact with you was because you have thankfully guided me about the three-dimensional image reconstruction algorithm. Although I could not make a considerable progress on this part of the project due to the limited time, it was very valuable for me that you gave me a future vision in this regard. I would like to thank you for that.

I would like to thank my committee members once again, Dr. Bryan Bednarz, Dr. Wesley Culberson, Dr. Douglass Henderson, Dr. Steve Cho and Dr. Oliver Wieben for generously accepting to examine the feasibility of my research proposal and for guiding me throughout my study.

The major funding of my study was by: the Turkish Ministry of Education under the YLSY grant program. I would like to thank the officials of the Turkish Ministry of Education and the organizers who made this scholarship possible to me.

I would like to thank you Dr. Steve Cho and people from the Department of Radiology at the University of Wisconsin-Madison for funding one year of this study under the R&D pilot funding program.

Special thanks to Dr. Bhudatt Palliwal from the Department of Human Oncology at the University of Wisconsin-Madison for funding the necessary tools and equipment of the project, including the cost of the integration of the detector, under the Discretionary Research Funding Program.

I would like to thank M.R. Farukhi, Ph.D and Zaid Farukhi from Rexon Components & TLD systems Inc. (Cleveland, OH) for assistance with the integration of the handheld radiation detector unit and lending their MCA unit for the measurements.

To Jeff Radtke from Calibration Laboratory, As you already know I had to change my previous Ph.D project after putting a considerable effort on it. No matter, in my old or current project, you have never turned me down whenever I needed help. I would like to thank you for all of your efforts.

Nobody has been more important to me in the pursuit of this project than the members of my family. I would like to thank my parents, Haci&Imran Bedir, whose love and guidance are with me in whatever I pursue. They are the ultimate role models.

I would like to thank my siblings Fatma, Elif, Ummugulsum, Hatice, and my mother-father in law Irfan&Alime Sariyar for their emotional support throughout my study. No matter we have been away from each other, I have always felt your support.

Most importantly, I wish to thank my loving and supportive wife, Hilal, and my three wonderful children, Rumeysa, Mahsum and Abdulhamid who provide unending inspiration. Hilal, all of the work that I have done so far has come true thanks to you because you did the hard job by taking care of our three lovely children while you were away from your parents and friends.

There are so many friends that have been on this journey with me, M.Nasuh Arik, Fatih Ortakci, Fatih Kunkul, Baris Kalaycioglu, Enes Kotil, Mustafa Karaaslan, Hilmi Gurleyen and many others. I would like to thank you all for the support and prayers you dedicated to me.

Table of Contents

List of Figures

List of Tables

Introduction

Primitive techniques to diagnose some of the diseases including cancer were based on touching and sensing some critical organs, tissues and skeletal systems. That was until 1895 when German Physicist Wilhelm Conrad Roentgen accidentally discovered x-rays during his experiments when he was repeating Hertz's and Lenardz's previous work on cathode rays. [1] He discovered that a new ray could pass through most of the tissues in the body except bones and metals and that was x-ray. Although the first use of the x-rays was not for medical application as Roentgen used x-rays to produce radiograph of weights in a box and to make a radiograph of her wife's hand, it did not take a long time after the discovery of x-rays, only within a month, x-rays were used in the form of medical radiography as a guidance to surgeons in Europe and the United States. [1] That was a new era for medical imaging. Shortly after the discovery of the x-rays, in 1896 Henri Becquerel discovered the radioactivity when he was studying the properties of the x-rays by exposing potassium uranyl sulfate to sunlight and placing it on photographic plates with the idea of by absorbing sunlight, potassium uranyl sulfate would emit the sunlight energy in the form of x-rays. [2] After that, it did not take long for him to understand the truth and discover the radioactivity of the uranium element [2]. Marie Curie then, discovered radium and polonium when she was working on the characteristics of some elements. Her work was inspired by Becquerel's previous work. [3] Her contribution to the science was not limited to the field of physics and

chemistry, she also made a huge contribution to the field of medical imaging by designing small and portable x-ray machines to be used in the field by medics. [3]

More than a century from the discovery of the x-rays, Gerritt Kemerink from Maastricht University Medical Center, found an antique x-ray machine sitting in a dutch warehouse which was used by scientists just weeks after Roentgen discovered the x-rays. [4] He took some X-rays of hand specimens and compared the quality of the image with current x-ray machines. He found out that the image quality was almost similar, except the old machine gave 1,500 times more radiation dose to the skin comparing to the dose given by the current technology. [4] That was a clear indication that the goal of medical imaging remained the same, to guide the medics having better diagnostics on the patients, although the imaging techniques and modalities have been improved since then.

Advancing technology and an increasing number of cases in cancer have revealed the need to further improve medical imaging devices and modalities. To give a more specific example to that; according to the American Cancer Society, breast cancer is one of the most common cancer types in American women. Sometime in her life, the chance to be diagnosed with breast cancer of an American woman is estimated at 12%. [5] The statistics by American cancer society also show that following lung cancer, breast cancer is the first cancer type that results in the death of American women. [5] 1 out of 38 American women die because of breast cancer. Based on the estimation of the American Cancer Society, about 268,600 American women will be diagnosed

with invasive breast cancer and 41,760 of them will die as a result of breast cancer in 2019. [5] All of these statistics reveal that starting from screening and evaluation to the therapy, all steps of the cure should be treated with extra care to find the most appropriate treatment plan for a breast tumor patient. However, non-palpable (occult, non-sensible) breast tumor localization has always been a challenge for surgeons. This is mainly because the localization of the tumor with conventional techniques rely on preoperative imaging. The big size and long acquisition time of conventional imaging devices make them infeasible for intraoperative use. Sometimes, images taken preoperatively with these imaging devices do not help the surgeon to precisely localize the tumor during the surgery. This is because the surgeon is unable to synchronize preoperative imaging data with the anatomy of the patient in a real-time fashion which causes the extent of the tumor indistinguishable from the normal tissue. Consequently, the tumor margins are mislocalized and re-excision procedure is often required. An observational study of breast surgery formed between 2003-2008 shows that among total of 2206 women diagnosed with breast cancer, 509 out of 2206 (23%) of them received one re-excision, 48 out of 509 (9.4%) patients that had one re-excision already, received the second, and 7 out of 48 (1.4%) that had two re-excisions already, received the third one to achieve adequate clear margins. [6]

To address the increase in re-operational and re-excision rates in breast cancer, handheld gamma probes are designed to be used intraoperatively to improve the precision of the breast tumor localization. Although they can be used intraoperatively, real-time image guidance is beyond the

scope of these probes as they are not intended to visually guide the surgeon during the surgery. An audible intraoperative output from these probes is combined with the preoperative imaging data and together let the surgeon decide and mark the surgical margins. That raised a new question to be solved in the field of medical imaging. Is a fully intraoperative radio-guided breast surgery possible? In that way, intraoperative image guidance could be provided letting the surgeon see the patient anatomy, tumor, and extent simultaneously and precisely localize the surgical margins prior to the excision. The answer was positive. There have been valuable improvements in this regard over the last decade. Using tumor-targeted tracers labeled with radionuclides through injection to the targeted tumor site or placing radiactive brachytherapy sources inside the tumor with the use of a handheld gamma probe or a gamma camera by mapping the radiactive distribution inside the tumor, real-time image guidance was provided to the surgeon. But just like any new system that was invented, besides the innovations brought by this system, there were some limitations due to the detector design and imaging methodology of the system.

The main motivation for this study was the same as that of the medical professionals after the discovery of x-ray, those who immediately built and used the x-ray machine, or those who contributed to the field of medical imaging after that: to better diagnose and treat the patients by better guiding the doctors. In order to achieve this goal, the constraints of intraoperative handheld gamma probes and limitations of the three dimensional, real-time image guidance system for breast

tumor surgery are addressed by designing, developing and characterizing a new radiation gamma detector.

This dissertation consists of two Parts. Part I discusses the current state of the art of the radio-guided breast tumor surgery in a total of 3 Chapter including some background in breast anatomy, breast tumor physiology, surgical modalities and tumor localization procedures (Chapter 1), underlying radiation physics of radio-guided surgery of breast tumor (Chapter 2). The history of the radio-guided surgery, literature review including the components, working principle, and limitations of handheld gamma probes and intraoperative 3D image guidance system will be discussed in Chapter 3 of Part I. It would be more appropriate to discuss the details and limitations of these technologies after providing some background information on the field of radio-guided surgery which will be presented in Chapter 1 and Chapter 2. After discussing these limitations in detail in Chapter 3. Chapter 3 also explains how this work proposes to handle each of these constraints.

Part II is the contribution part of the thesis which consists of four chapters in total, Chapter 4, Chapter 5, Chapter 6, Chapter 7.

Chapter 4 focuses on the design parameters and the process of the development of the radiation detector used in the project. Among the wide selection of detection materials, in order to find the best fit for the project a detailed comparison and discussion are presented in terms of some

important detector characteristics. The selection of the photomultiplier type and deciding factors are discussed. Crystal dimensions are determined based on the maximum photoelectron range and intrinsic absorption efficiency data of the crystal. Finally, the process of development of the detector in collaboration with Rexon Inc, (Ohio) is summarized and final production is graphically presented.

Chapter 5 discusses the experimental and computational characterization results of the device with no collimation in use. The energy resolution of the detector is examined by taking a pulse height spectrum of different multi-nuclides: (^{109}Cd, ^{57}Co, ^{99m}Tc, ^{123}I, ^{137}Cs and a multi-nuclide source) experimentally. In addition to that, the experimental energy spectra are analyzed when both ^{99m}Tc and ^{123}I are in use together to see if the detector capable of distinguishing energy peaks coming from each source. Some of the experimental pulse height spectra data is compared to the Monte Carlo simulation data to validate the results. The experimental detection efficiency of the detector at a certain source to detector distance is plotted as a function of incoming photon energies. Finally, the detector response to the distance measurements is tested experimentally and presented graphically.

In Chapter 6; the collimation material, thickness, and geometry are examined. Since there is a known trade-off between sensitivity and spatial resolution, which are known as two key characteristics of the detector, geometry of the collimation is analyzed both experimentally and computationally (MCNP) in order to find optimum geometry of the collimation that would allow

having sufficient sensitivity and fast acquisition to create real-time image of radioactive distribution and at the same time having a decent spatial resolution so clustered sentinel lymph nodes at depth can be resolved from each other. Based on the presented results, an optimum geometry of the collimation is proposed. The optimum collimation design is simulated in MCNP and some of the detector features are characterized computationally. The results are then compared with literature.

Chapter 7 starts with conclusions extracted from this study. In order to accomplish the aim of the overall project, next steps: integration of the tracking system to the detector for on the fly measurements, generation of the response functions of the detector, and generation and implementation of the 3D image reconstruction algorithm are discussed.

Part I. Status Quo

1. Introduction to Breast Tumor and Surgery

1.1. Breast Tumor Basic Definitions

Breast cancer is a type of cancer that arises in breast tissue. In scientific terms, it is the irregular growth and proliferation of tumor cells that emerge from breast tissue. [7] **Glandular and stromal tissues** are the two main types of breast tissue. Glandular tissue consists of milk-producing glands called **lobules** and milk passages known as **ducts**. Stromal tissue consists of fatty and connective tissues as seen in Figure 1.1 (a) below. Excess soft tissue fluids and waste are eliminated by lymphatic tissue, which is another tissue type that is located in breast tissue. Since the breast is mainly formed of ductal and lobular tissues, cancer most commonly forms in these cells, which are called **ductal and lobular cancers,** respectively. [8] Alternatively, there is a

smaller chance of cancer forming in other non-glandular cells in the breast, which are named **sarcomas and lymphomas, which are** not considered specifically as breast cancers. [8]

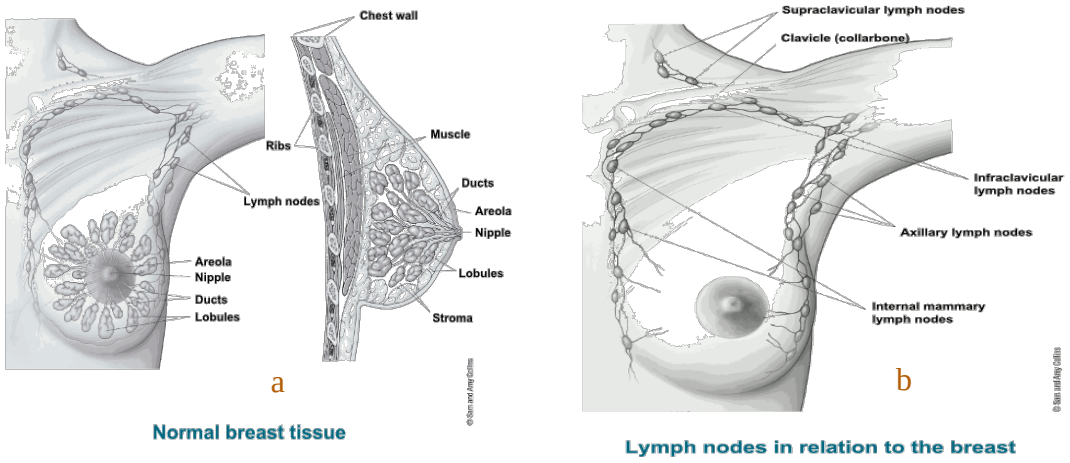

Figure 1.1 (a) Anatomy of normal breast tissue (b) Main paths and sites of the lymphatic vessels through nodes. (Adapted from Collins, Sam, and Amy) [8]

Lymph nodes in the body are connected to each other by **lymphatic vessels**. **Lymph** is a fluid that flows through the lymph vessels, comprised mostly of excess water and waste, and is managed and drained by lymphatic vessels, returning eventually to the blood circulation via the subclain vein. Cancer cells in tissue can travel through these lymphatic vessels and end up growing in lymph nodes. Figure 1.1 (b) above shows the main anatomic sites of the lymph nodes along lymph vessels which includes **axillary nodes** (lymph nodes under the arm), **supraclavicular** and

infraclavicular nodes (lymph nodes above and below the collar bone) and **internal mammary nodes** (lymph nodes inside the chest close by the breast bone). [8] The existence of cancer cells in lymph nodes raises the likelihood of cancer cells travelling through the lymphatic system and spread to other organs of the body. In **non-invasive cancer**, cancerous cells are mostly trapped in ducts and do not penetrate to the connective and fatty tissues of the breast. **Invasive breast cancer**, on the other hand, is when cancerous cells are not limited to ducts and invade the surrounding connective tissues. The fact that the cancer is invasive does not always mean that it invades lymph nodes and other organs as well. [9] **Lobular carcinoma in situ** (LCIS) and **ductal carcinoma in situ** (DCIS) are the most common types of non-invasive breast cancer. As it can also be understood from their names, DCIS is a type of breast cancer in which cancer cells are confined to the ducts. in the same manner, LCIS is a type of breast cancer in which cancerous cells are trapped within lobules of the breast. The most common types of invasive breast cancer are mainly divided into two branches, **infiltrating lobular carcinoma** (ILC) in which the cancerous cells initially begin in lobules of the breast and then spread to the other organs or the tissues of the body and **infiltrating ductal carcinoma** (IDC) in which the cancerous cells start into ducts and propagates to the wall of the duct and fatty connective tissue. It is more likely to spread to other organs of the body. Among all of these modes of the breast cancer, IDC is known as the most commonly occurring breast cancer. [9]

1.2. Surgical Modalities for Breast Cancer

Breast tumor surgery is subdivided into four branches in terms of excision procedure: total (simple) mastectomy, modified radical mastectomy, partial mastectomy, lumpectomy.

1.2.1. Total(Simple) Mastectomy

Total mastectomy is a surgical procedure in which the whole breast with breast tissue, areola, and nipple is removed by the surgeon as seen in Figure 1.2. Some of the lymph nodes under the arm may also be removed with total mastectomy. Total mastectomy is optionally offered by the surgeons to the patients diagnosed with DCIS, stage I and II breast cancer, stage III locally advanced breast cancer. [10]

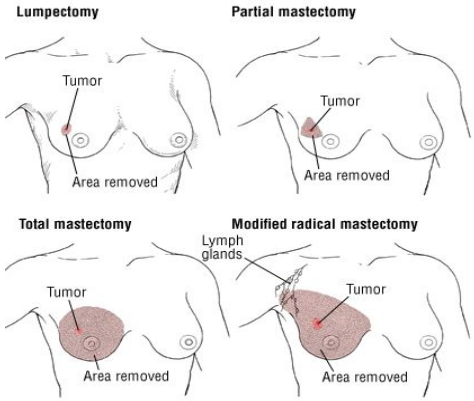

Figure 1.2 is a graphical representation of different breast tumor surgery modalities based on the sites and volumes excised. (Extracted from online, it is publicly used by several online sources, no copyright or trademark information was stated)

1.2.2. Lumpectomy

In contrast to total mastectomy in which the entire breast tissue is removed, lumpectomy (also called a tylectomy is a form of breast-conserving surgery where the surgeon removes only the breast tumor and some tissue around it as seen in Figure 1.2. [11]

1.2.3. Partial Mastectomy

Partial mastectomy is more comprehensive compared to lumpectomy. As seen on Figure 1.2, in addition to the lumpectomy procedure, the lining over the chest muscles deep to the tumor is removed as well. Since the breast is saved, it can be counted in the category of breast-conserving surgery. However, the defect in the breast will be more extensive compared to that in a lumpectomy. [11]

1.2.4. Modified Radical Mastectomy

A modified radical mastectomy removes the entire breast with skin, areola, nipple and most of the lymph nodes under the arm, except the pectoralis major muscle. It is the traditional method in the treatment of breast cancer. [12] [13] Figure 1.2 shows the tissues removed during a modified radical mastectomy.

1.3. Sentinel Lymph Node Biopsy

In sentinel lymph nodes biopsy (SLNB), a radiotracer (mostly nanoparticles labeled with technetium-99m, ^{99m}Tc) is injected near the tumor area which guides the surgeon to localize sentinel nodes during the surgery. Following the localization, sentinel nodes are extracted and sent for pathological examination. It is a supportive pathological procedure performed after the surgeries to assess whether the cancer cells have invaded the lymphatic system. Initially, only nodes under the arm are removed for the examination. In case of positive results, the doctor may recommend to remove additional lymph nodes. [11]

1.4. Localization Modalities in Breast Cancer

1.4.1. Wire-Guided Localization (WGL)

The traditional, non-palpable, breast-tumor localization method, known as wire-guided localization (WGL), uses either a mammogram or an ultrasound image as a guide. A guide wire is placed in to area of concern by radiologists to locate the tumor. Then, a second mammogram is performed to document the position of the wire. Following the wire insertion, the surgeon locates and removes both wire and wire-targeted area in the breast.

1.4.2. Radioactive Seed Localization (RSL)

Although, WGL has been a useful tool to locate non-palpable breast tumors and lesions for decades, it brought with it several irreparable drawbacks. Usually, placing the hooked wire into the breast, as seen on Figure 1.3 (a), and the surgery procedure are performed on the same day, which generally causes a conflict and struggle to plan, schedule and organize both procedures in a timely manner. More importantly, a mis-localization of the tumor site and wire may have emerged as the result of possible displacement of the inserted wire due to the post-insertion mammography or transportation procedures. Such uncertainty in the location of the tumor creates a challenge for the surgeon and often results in inadequate excision of the margins of the tumor. [14]

RSL has been introduced as an alternative to the WGL. A titanium capsule, with dimensions of 4.5 mm in length and 0.8 mm in diameter, that contains 0.10-0.15 mCi (3.7-5.6 MBq) of radioactive Iodine-125 (^{125}I) is used in this procedure. The source is the same as that used in permanent brachytherapy. Under mammographic or Ultrasound image guidance, the seed is inserted to the region of interest, as seen on Figure 1.3 (b). [14] The tumor site that contains the ^{125}I source activity can then be excised by the surgeon with the guidance of a commercially available gamma probe that is set to detect the low-energy gamma photons of 35 keV emitted from ^{125}I. This probe can also be used in the SLN and localization procedure for the biopsy by changing the energy settings to detect the 140 keV photon energies coming from ^{99m}Tc labeled sulfur colloid. [15]

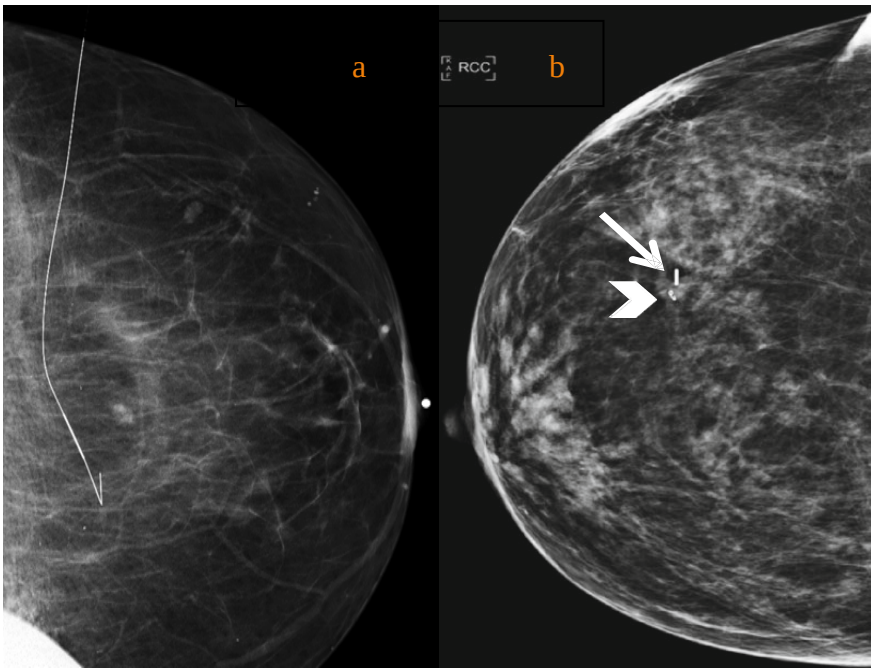

Figure 1.3 (a) Mammographic image after wire-guided localization procedure performed (b) Mammographic image showing ^{125}I source inserted to the lesion (arrow) and the marking clip (arrowhead) before the biopsy procedure. (Copied from Gray R.J., Cox C.E., Dauway E.L. et al with permission) [14]

Since neither the radioactive seed inserted into the breast nor the equipments used in the RSL procedure are dependent on the displacement, the programming difficulties found in the WGL can be easily overcome by the RSL. [14] In some practices, several months have been observed between the seed localization and surgery procedure. [14, 16] Moreover, the maneuverability of

the portable gamma probe and continuous audible signal guide the surgeon better than the wire in managing the localizing the center of the tumor. [14]

RSL begins with the insertion of the radioactive seed into the tumor targeted area by using a mammography or an ultrasound image as the guidance. Thanks to commercially available preloaded needles, surgeons do not have to load the 18-gauge needle with a ^{125}I seed during the surgery. Although permanent brachytherapy is performed with magnetic resonance imaging (MRI) guidance, MRI guidance of seed insertion is not recommended in some studies due to the limitation of using radiation equipment in MRI room. [14] [17] [18] [19] Local anesthesia is applied to the area of the targeted skin, then the tumor site is imaged by mammogram or ultrasound, and the surgeon inserts the needle containing the ^{125}I seed into the center of the tumor. The ^{125}I source is inserted into the area of the lesion using the stylet to push the source just out of the needle. The needle is then withdrawn. To verify the accurate placement of the seed in the site of the tumor, another mammogram or ultrasound image is taken. More than one ^{125}I source may be placed into the target of interest in case the size of the tumor is bigger than the average size of a breast lesion . [14] Although ^{125}I has a 60-days half-life, which would allow many days between the localization and excision procedure, the usual separation between these two procedures is only 5 days in the U.S due to the some radiation protection principles. [15] [20] Limiting the time to five days with the seed in place requires no radiation precautions since the dose to the skin from the seed in that time is less than the skin dose from a single mammographic exposure [15]

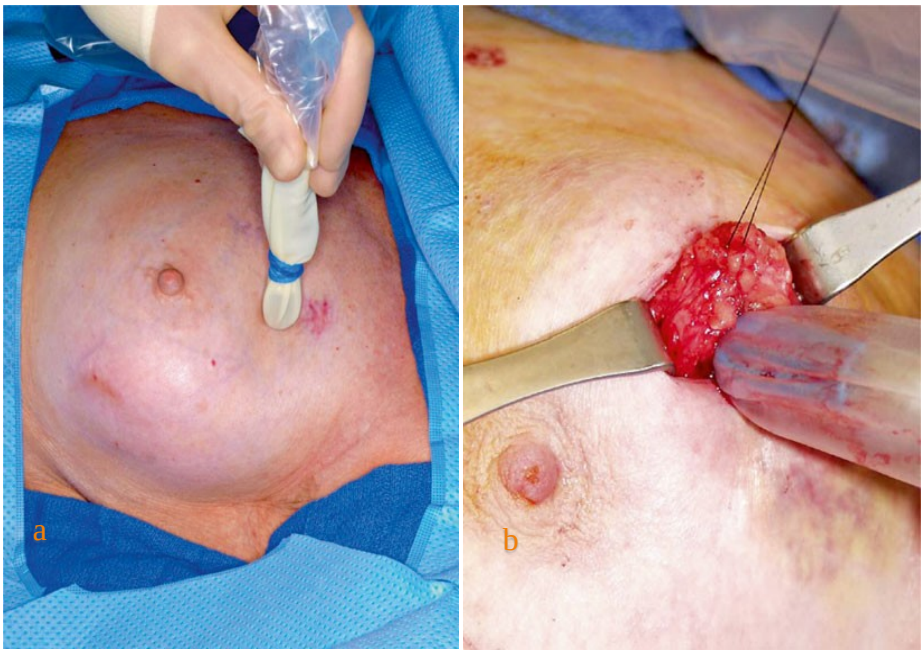

Figure 1.4 (a) Survey of the breast to determine the position of the ^{125}I source with a commercially available gamma probe. (b) Survey after the incision to determine the tumor site and depth of the tissue containing the source (Copied from Gray R.J., Cox C.E., Dauway E.L. et al with permission) [8]

A commercially available gamma probe is equipped with various settings so different isotopes with different peak energies can be detected. Figure 1.4 (a) shows how measurement data as an output from the probe is collected by the surgeon by scanning it over the breast. Probes optionally come with an audible guidance. The higher the pitch of the audio indicates the higher

the activity detected in the area of the probe tip. This area is then marked as the incision site, which is the smallest distance between skin and lesion. After performing the incision, the gamma probe is utilized again to guide the surgeon deciding location and volume of the tissue dissected, as seen on Figure 1.4 (b). Following the excision, the surgeon uses the gamma probe once more to make sure the ^{125}I is located inside the resected tissue and no radioactivity left inside the tumor bed. [14] This is generally challenging because the Compton-scatter photons from the ^{99m}Tc in the lymph system are also detected by the gamma probe in addition to photopeak energies coming from ^{125}I. Hence, the surgeon should be well experienced and the probe should be able to distinguish the radiation lines coming from each sources.

The resected tissue with the radioactive seed inside is then send to the pathology department for histopathological examination. The ^{125}I source is located by pathology staff after marking the area with ink. If accurate insertion of the seed was performed before the surgery, the location of the source helps the pathology staff locate the lesion. After identification, the seed is transported to the nuclear medicine department in a lead container for long-term decay prior to disposal. [15] [21]

1.4.3. Radio-occult Lesion Localization (ROLL)

Radio-occult lesion localization (ROLL) was first introduced in 1996 which uses a ^{99m}Tc labeled radiotracer intratumorly injected to the patient in order to locate and excise the tumor

during the surgery by the guidance of a commercially available gamma probe. It has been widely adopted to the field and used as a reliable alternative to the WGL since then. [22] As opposed to the RSL technique which uses a ^{125}I source to locate the center of the tumor, ROLL uses a ^{99m}Tc labeled radiotracer called macro aggregated albumin (MAA) for tumor localization. [22] Current studies show that ROLL is found to be a more useful procedure than WGL in terms of comfort of the patient, the frequency of the clear margins, and localization time and an ease to be combined with sentinel lymph node biopsy. [22]

The ^{99m}Tc-MAA radiotracer, with a particle size range of 10-150 µm, is injected into the tumor under the guidance of ultrasound or stereotactic mammographic imaging. [22] Since the activity of the injected radiotracer is relatively low, between 0.027-3.324 µCi (1-123 MBq), only negligible amount of the activity moves to the lymph nodes, the rest staying within the tumor. [23] [24] [25] During the injection process, the needle tip and the tumor are visualized simultaneously. Once the needle tip is advanced to the tumor location, the radiotracer is then administrated to the region, as seen in Figure 1.5. The mass and volume of the injected MAA mixture is often 0.5µg and 0.2 ml respectively. [26] The radiotracer administration brings some risks with it, such as skin contamination, missed localization and risk that the blood vessel will be punctured and tracer carried to the liver. [22]

Figure 1.5 Radiotracer Injection Process. (a) Needle tip is being placed into the lesion under ultrasound guidance. (b) Syringe is integrated with a Luer-Lok connection for leakage protection. (c) The syringe is covered with lead to protect staff from radiation. (d) Intratumoral radiotracer injection under the guidance of ultrasound image (Copied from B. Pouw et al. [22] with permission)

ROLL procedure can be combined with sentinel lymph node biopsy (SLNB) in two different ways. The first technique includes the intra-tumor injection of ^{99m}Tc-MAA and subdermal injection of ^{99m}Tc-nanocolloid to the level where lesion locates. [22] [27] [28] The next

technique allows surgeon to facilitate both radiotracer in one injection by utilizing ^{99m}Tc-albumin nanocolloid into the tumor.

Since the travel range of the ^{99m}Tc-albumin nanocolloid tracer is limited from the injection site, only small fraction of injected radioactivity (0.1-1%) is able to move to the lymph nodes which allows coupling both procedure in one session. This integration is called as SNOLL (SLNB+ROLL). [22] [29] Although one tracer SNOLL procedure found to be more comfortable, lower cost and shorter time procedure than SLN in detection of sentinel nodes and lesion, a current study of SNOLL shows that SNOLL is less effective than SLNB procedure in SLN detection [29]

After radiotracer administration, skin contamination and migration of the radiotracer from breast to lymphatic vessels or breast parenchyma should be checked under the guidance of planar gamma-camera imaging. In case of skin contamination, a decontamination process is recommended which prevents having false findings during the localization and surgery procedure. [22] A clinical study shows that 4 out of 959 patients (0.4%) are observed with considerable amount of radioactivity spread to the breast parenchyma. [30] A SLNB gamma-camera imaging procedure is applied to SNOLL procedure, in which some facilities use planar static images taken 15 min and 3hr after injection. These images are then used to visualize the patient contour when a flood source is placed under the patient. [22] [31]

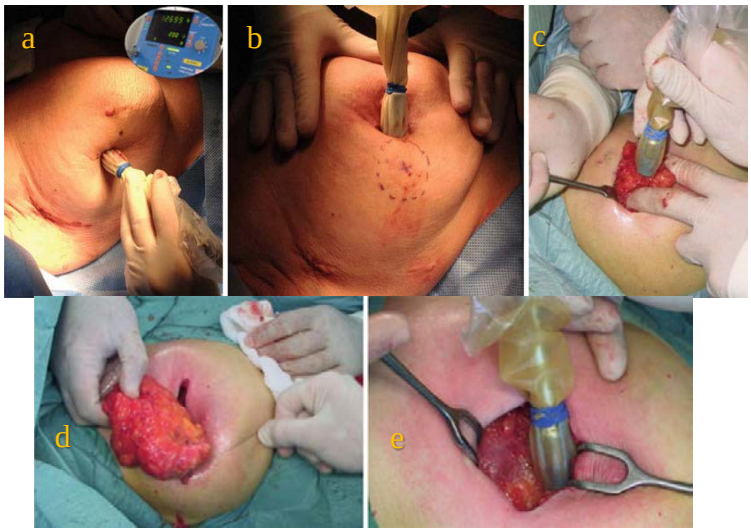

Figure 1.6 localization in ROLL. (a) The highest output from the probe is detected and the site marked on the skin. (b) The incision site is evaluated and determined by the surgeon. (c) Survey performed after the incision to determine the area of the excision. (d) Excision of the tumor with the margins determined in picture c. (e) A survey in the cavity of the breast after excision. (Copied from B. Pouw et al. [22] with permission)

In the operating room, as with RSL, a commercially available gamma-probe can be used to detect radiation from the radiotracer after injection. Since there are many types of gamma probes on the market, their critical features, such as the sensitivity, energy resolution, and spatial resolution differ. Once the location of the highest counts while passing the detector over the skin is detected, it is marked as the incision point. Following the incision, the probe is used to measure

the margins by evaluation of the drop in the count moving from the tumor to the surrounding tissue. The area determined to be tumor is then excised. A survey of the rest of the cavity is performed by scanning the probe around the region to assess for residual tumor. In case of radioactivity found in the cavity, the excision site is enlarged. The whole procedure is summarized in Figure 1.6.

1.4.4. Radio-guided Sentinel Lymph Node Biopsy

Technetium-99m is a cost effective, easily accessible, low-dose isotope of Technetium, which has been widely used for the localization of the sentinel lymph nodes. There are a variety of carriers utilized with ^{99m}Tc in SLN detection including sulfur colloid, nanocolloidal albumin, antimony trisulfide colloid and Lymphoseek™ (^{99m}Tc-tilmanocept, targeting CD-206 receptors on macrophages). Among of these radiopharmaceuticals, only ^{99m}Tc-sulfur colloid was FDA registered until 2013. Therefore, it was the only accessible radiotracer in the United States that has been used for SLN mapping in breast cancer until 2013. However in 2013, FDA approved one other radiotracer to use for SLN detection breast cancer which is called as Lymphoseek™ (^{99m}Tc-tilmanocept). The other two radiotracer using ^{99m}Tc, described above, are widely used in foreign countries and reported as effective as ^{99m}Tc-sulfur colloid in SLN localization. [32]

Due to the large particle size of ^{99m}Tc-sulfur colloid (having a mean particle size of 300 nm), it is believed that drainage of this radiotracer into the lymphatic vessels after the injection is less likely to occur. As a precaution action to this potential problem, ^{99m}Tc-sulfur colloid is

infiltrated through a filter just before the injection. However, according to a research study performed by Martin et al., filtration of ^{99m}Tc-sulfur colloid prior to injection showed no improved impact on identifying the sentinel nodes compared to not filtering. [32] [33] Contrary to what is believed, another study showed that filtration of the radiotracer before injection decreases the rate of sentinel node detection compared to not filtering. [34]

A wide variety of isotope injection methods have been used in the literature in terms of isotope volume, the time of injection, the location of injection. However, no considerable difference in success rate has been observed. [32] Although, there is no standard volume of injection recommended, the injection volume of the radionuclide in sentinel node identification varies between 0.05 ml and 16 ml. [32] [35] Timing of radiotracer injection is examined by McCarter et al. [36] No matter if the radiotracer is injected a day before or at the same day of localization procedure, comparable results in the rate of SLNs identification have been observed in the study. However, the authors highlight that the activity of the radiotracer at the time of localization should be comparable for both cases, so the decay correction should be taken into account to determine amount of activity to be injected for each case. [32, 36]

The location of the radiotracer administration is another factor that affects the success rate in SLN localization. Several studies revealed that regardless of which method the radiotracer was injected into the patient (intradermal (ID), subdermal (SD), intratumorally (IT) etc.), there was no significant increase in the success rate of mapping axillary sentinel nodes. [32] However, while

the depth of injection has not been found to be an important factor for localization of axillary nodes, it is important for internal mammary (IM) lymph nodes. While superficial or intradermal (ID) injections are sufficient to identify axillary nodes, a deeper intraparenchymal (IP) injection is required for the localization of IM nodes [37]

The current state of the art of SLN localization allows the utilization of radiotracer alone, blue dye alone or combination of two. The success rate of SLN detection is reported as 91.2%, 89.2% and 83.1% with the use of only radionuclide, blue dye or both, respectively. [38]

The procedure for SLN localization using only radiotracer was described above. If using a combination of radiotracer and blue dye, blue lymph vessels and nodes are first localized to guide the surgeon determining the dissection area. Additional guidance for determining the excision area is supplied by a gamma probe that audibly guides the surgeon to localize the nodes containing the highest radioactivity. [32] Both radiotracer and blue nodes are then dissected by the surgeon. Dissecting only the nodes containing the highest radioactivity is not solely enough, as reported by Martin et al. His study showed that the probability of the most radioactive SLN being actually a SLN positive node is 80%. [39] McMaster et al. therefore suggested a rule, which is called the 10% rule, in which all nodes that contain at least 10% of the activity of the most radioactive node are submitted as SLNs and dissected eventually. [40]

2. Radiation Measurements

Although current technology in radio-guided surgery is well-equipped and structured, measurements of radiation in the human body with handheld devices or portable cameras requires knowledge about the effects of radiation on the body. It is also essential for surgeons, engineers and researchers to be familiar with problems that might arise during the scanning process and the physics processes related to the issues. This will prevent surgeons from performing unnecessary scans. [41] The subsections below discuss the relevant background on the physical processes.

2.1. Interaction of γ or X-ray Radiation with Matter

In radioguided surgery, gamma particles emitted from radiotracers often result in two major interactions within matter depending on the energy of emitted particles and atomic number of the medium in which the interaction takes place. A gamma or x-ray photons transfers its energy, partially or entirely, in a single interaction to an electron in the medium along its path of travel. The energy given to the electron is then deposited in the medium. If the medium is the crystal of a

detector then the energy deposited contributes to the number of counts recorded by the detector. The underlying physics of the interaction of photons with matter are discussed below.

2.1.1. Photoelectric Absorption

In the photoelectric effect, an emitted photon from the radioactive source interacts with a bound orbital electron of an atom. The photon is absorbed and part of the energy from the photon is used to overcome the binding energy of the electron, freeing it from the atom. The other part of the photon's energy goes into kinetic energy of the emitted electron. The ejected electron leaves a hole in the orbital shell that it originally occupied. The electron emitted is usually a K-shell electron. The vacancy in the shell is filled by one of the upper shell electrons through rearrangement of electrons between shells, or alternatively, it is filled by the capture of a free electron in the medium. The difference in the binding energies of the electrons before and after rearrangement creates one or more characteristic x-rays. The characteristic x-ray and the ejected electron are called a fluorescence photon and photoelectron, respectively. The low-energy characteristic x-ray travels some distance in the medium and interacts again through one of the two interactions mechanisms discussed and the interaction is usually with a less tightly bound electron of an atom. The kinetic energy of the photoelectron is computed by Equation 2.1 below, where E_e is the kinetic energy of the photoelectron, hv is the energy of incoming photon and E_b is the binding energy of the electron in its original shell:

$$E_e = hv - E_b\,. \tag{2.1}$$

An alternative to the characteristic florescent radiation release, when the outer-shell electron drops to fill the vacancy in the shell from where the photoelectron originated, is the transfer of energy to another electron in its shell or an electron with less binding energy. The remaining energy above the binding energy appears as kinetic energy of the ejected electron as it leaves the vicinity of the atom. The ejected electron is called an **Auger electron**. Since the kinetic energy of the Auger electrons is low, its range is very short.

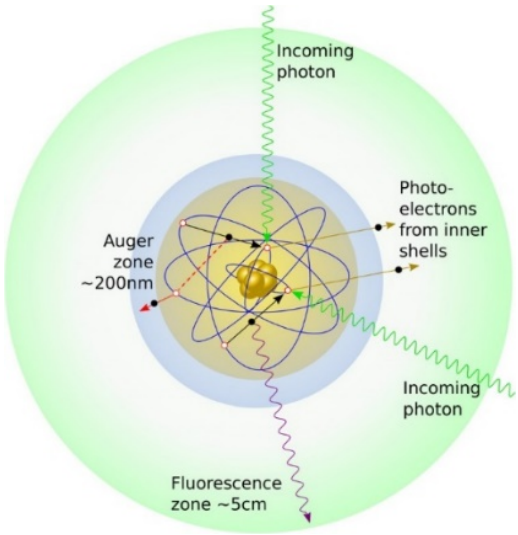

Figure 2.1 Graphical representation of the emission of a photoelectron, auger electron and their relative range after the interaction. (Copied from H L Byme et al. with permission.) [42]

The Auger effect competes with the emission of characteristic x-ray florescent. On average, the photoelectric effect results in the emission of characteristic x-rays 88% of the time and Auger electron release the remaining 12% of the time. [43] The entire photoelectric process is graphically summarized in Figure 2.1.

2.1.2. Compton Scattering

Compton scattering is a process in which an incoming photon has a scattering interaction with one of the loosely bound outer shell electrons of an atom in the medium. The incident photon scatters with an angle θ imparting energy to the electron. The scattering interaction is illustrated in Figure 2.2. The resulting electron is called a recoil, or Compton electron. The energy of the scattered photon and recoil electron can be calculated from Equations 2.2 and 2.3, respectively, which are derived from basic conservation of energy and momentum laws:

$$hv' = \frac{hv}{1 + \frac{hv}{m_0 c^2}(1 - cos\theta)}, \qquad \text{and} \tag{2.2}$$

$$E_{e^-} = hv - hv' = hv\left(\frac{\frac{hv}{m_0 c^2}(1 - cos\theta)}{1 + \frac{hv}{m_0 c^2}(1 - cos\theta)}\right). \tag{2.3}$$

In the above equations, the energy of the recoil electron is denoted by E_{e^-}, the energy of the incoming photon is hv, the energy of the scattered photon is $hv'$and the rest mass energy of the electron is denoted by m_0c^2 $(511\ keV)$. As the scattering angle θ decreases, the amount of energy transferred to the electron also decreases. The interaction probability for Compton scattering depends on the electron density in the absorber material, and as a result, the atomic number of the absorber (Z) is a major determinating factor for the likelihood of a Compton scattering interaction. As Z increases, the probability of having a Compton event increases as well.

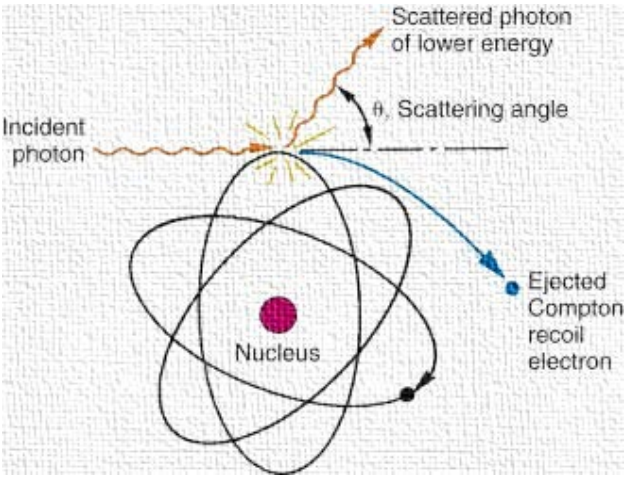

Figure 2.2 Pictorial representation of Compton Scattering. (Copied from from S.R. Cherry et al. with permission.) [44]

The angular distribution of scattered photons can be determined from the Klein-Nishina formula which shows that incoming photons with higher energies are more likely scattered in the forward direction. Hence according to Equation 2.3, energy transferred to the electron is small. On the other hand, as the incoming photon energy decreases, the fraction of photons scattering backwards increases as illustrated in Figure 2.3 below. Thus, on average, low energy photons will transfer a larger fraction of their energy to the recoil electrons.

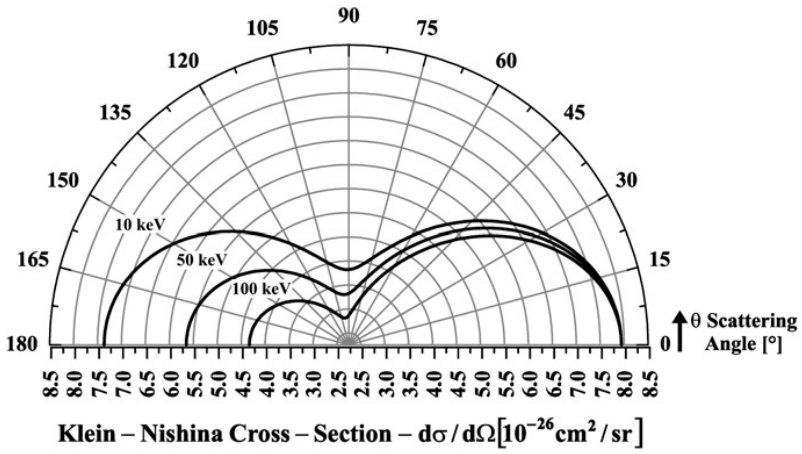

Figure 2.3 A graphical representation of the Klein-Nishina Cross-section of Compton scattering as a function of scattering angle of the incoming photon with different initial energies. (Copied from Scannavino et al. with permission.) [45]

2.1.3. Pair Production

Pair production will only occur if the incoming photon energy is greater than twice the rest mass energy of the electron (1.022 MeV). In this process a photon interacts with the electric and magnetic (E&M) fields of an atom, or on rare occasions, with the E&M fields of an electron. The photon disappears and an electron-positron pair is created. Since a positron is not a stable particle, it can decay into its basic constituents, or, which is usually the case, after travelling in the medium and losing most of its kinetic energy, it annihilates after an encountering an electron in the medium.

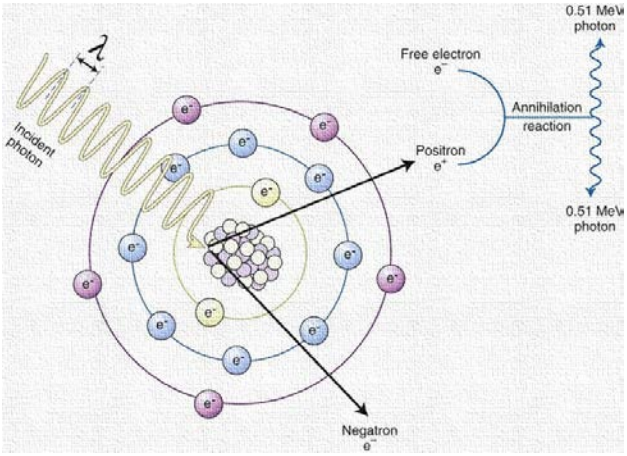

Figure 2.4 A graphical representation of Pair Production. A photon interacts with the positively charged nucleus of the atom, creating a positron-electron pair. The positron in the medium combines with the free electron, two particles disappears by creating two annihilation photons in opposite direction. (Copied online from [46] with permission.)

Both the electron and the positron disappear and two (sometimes three) annihilation photons in opposite direction are created, each having the rest mass energy of the electron, 0.511 MeV, as seen in Figure 2.4.

Equation 2.4 below expresses the energy relation of the pair production process. The electron-positron pair shares the energy of the incoming photon less twice the rest mass energy of the electron:

$$E_{e^+}E_{e^-} = hv - 1022\ keV\ . \qquad (2.4)$$

2.1.4. Rayleigh (Coherent) Scattering

Coherent scattering is an alternative scattering mode to the photoelectric effect and Compton scattering, in which a photon interacts with the atom as whole. No atomic excitation or ionization takes place in Rayleigh scattering, but the angle of the scattered photon will be different from the original angle of the incoming photon after the interaction as illustrated in Figure 2.6 below.

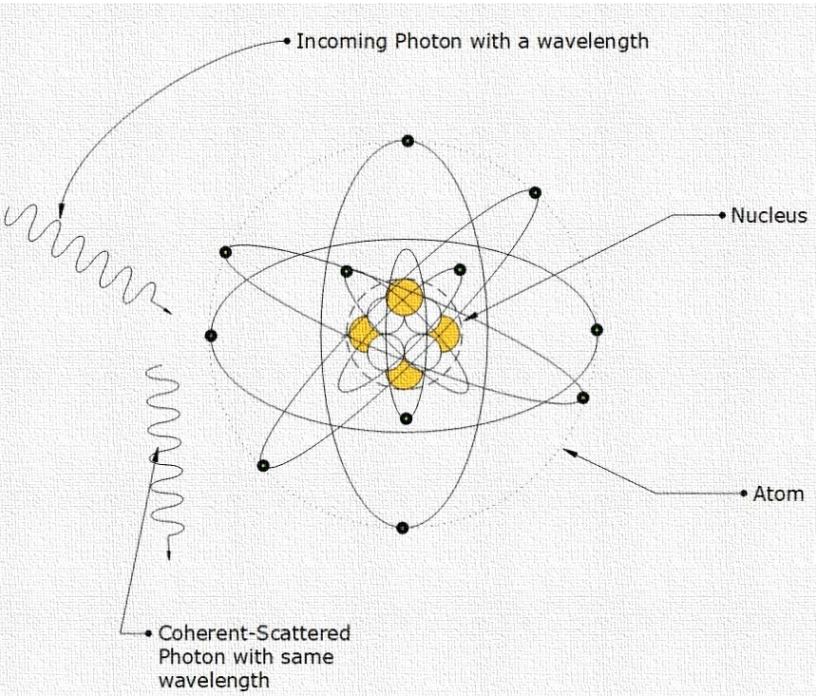

Figure 2.5 A graphical representation of Rayleigh (Coherent) Scattering.

2.1.5. Relative Proportions of the Interactions

Comprehensive analyses and measurements were performed by Evans et al. to determine the relative importance of the three major interactions of photons with matter as a function of atomic number of the absorber and energy of the incoming photon. [47] The results are graphically expressed in Figure 2.6. The photoelectric effect is the predominant process for low energy photons ($\leq$ 0.3 MeV) in high atomic number absorbers. Compton scattering, on the other hand, is

the leading mode of interaction for photons with intermediate energy (0.3-3.0 MeV) and a wide range of atomic numbers. Pair production is dominant for higher energy photons (≥3.0 MeV) and high Z. [47]

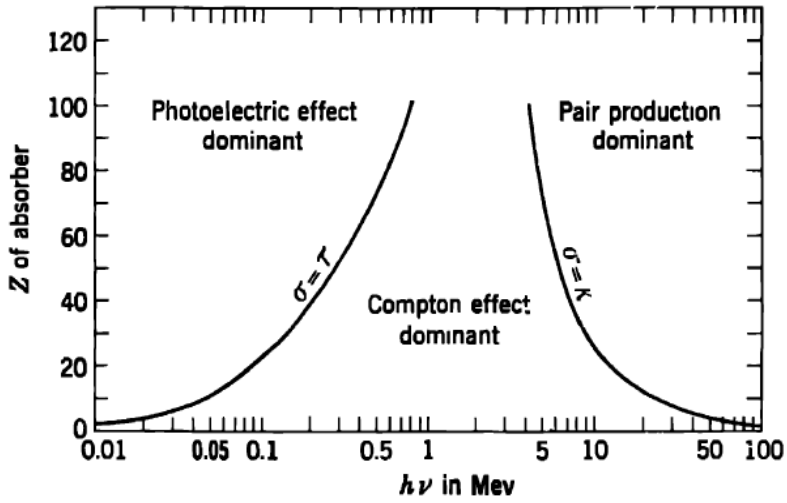

Figure 2.6 by Evans et al: Plot of the relative importance of these three major of gamma and x-rays interaction with matter as a function of the atomic number of the absorber and energy of the incoming photon. [47]

In this study, the energy range of gammas and x-rays emitted by most radioisotopes used in radio-guided surgery is below 1 MeV and we will be observing energy transferred to the electrons after each interaction. In this energy range the dominate photon interaction modes are the

photolectric effect and Compton scattering and, hence, pair production is an irrelevant mode of interaction for this project.

2.2. Interaction of Electrons with Matter

Secondary electrons are produced as a result of ionization. They are called secondary because they are genareted from the primary radiation, such as ions, electrons or photons. Owing to fact that secondary electrons might be created as a result of the interaction of photons with matter, the interaction of charged particles with matter is also relevant to radio-guided surgery.

Since $\beta^{+} and\ \beta^{-}$ are charged particles, they can interact with the orbital electrons or the positively charged nucleus. The interaction of electrons occurs through the loss of their kinetic energy (or speed).

Freely moving electrons interact with bound electrons through two different modes, ionization and excitation. When a freely moving electron approaches an orbital electron, the repulsive coulomb force can transfer some of its kinetic energy to the orbital electron, ejecting it from the atom if the transferred energy is sufficient, converting the atom into a positively charge ion (a process called ionization). The ejected electron is known as a secondary electron and is called a delta-ray. Excitation is when the moving electron transfers less energy to the orbital

electron than necessary to ionize the atom. The result in this case is that the bound electron transitions to a higher orbital level. A secondary electron is not created in this case. The initial incoming or freely moving electron slows down and losses energy.

When freely moving electrons travel in the medium they slow down as they interact with the atomic nuclei, sometimes causing a major deflection in their direction and the emission of a photon as the result. These photons are called bremsstrahlung radiation. An approximate emission probability of bremsstrahlung photons relative to the ionization and excitation can be determined from Equation 2.5 below in which ρ is the Bremsstrahlung yield, Z is the atomic number of the absorber atom and E_β is the maximum energy of the electron: [48]

$$\rho \approx \frac{ZE_\beta}{3000\ MeV}\ . \qquad (2.5)$$

Unlike gamma rays, penetration by electrons in tissue cannot be expressed by the simple exponential attenuation law; it is rather determined by empirical formulas as in Equation 2.6 below [49], where R is the range of the electron in the unit of g/cm^2:

$$R = \begin{matrix} 0.412E^{1.265-0.0945\ lnE} & 0.01 < E < 2.5\ MeV \\ 0.530E - 0.106 & E < 2.5\ MeV \end{matrix}\ . \qquad (2.6)$$

2.3. Measuring Radiation in the Tissue

The type of interaction with matter varies by the type of radiation involved, as discussed in the previous subsections. Radioguided surgery requires a careful analysis of the effects of the different radiation types for the accurate detection of radiation sources in the human body.

One of the other factors that affects the detection of radiation sources in the body is the geometry of the measurement system which involves the diameter of the detector "D" and the distance between the detector and radioactive source "d". The ratio between flux incident on a detector, I_d , to the fluence of the source, I_s , is approximately proportional to square of the ratio of *D* to *d* as illustrated in Equation 2.7 below [41]:

$$\frac{I_d}{I_s} \propto \frac{D^2}{d^2} \quad . \tag{2.7}$$

Equation 2.7 is known as the solid angle effect in the language of radio-guided surgery. It solely depends on the geometry of the measurement setup. It can be interpreted as follows: when the distance between the detector and source increases, the fraction of radiation detected decreases, or as the diameter of the detector increases, the fraction of the radiation detected increases. It is vital for a surgeon to interpret this solid angle effect correctly in case the source in the tissue is smaller in size and deeper in the tissue. [41]

2.3.1. Detection of γ and x-rays in tissue

Gamma and x-rays play very important roles in the detection of radioactive sources in the tissue. Because they have a very short range in tissue, β particles, on the other hand, are not useful to locate radioactive sources in the tissue. No matter what the origin of the γ and x-rays (from γ decay, radioactive emissions, bremsstrahlung, and annihilation), they generally interact with matter through absorption and scatter. [41] Generally, tissue has a lower atomic number than most shielding materials and collimators, hence absorption through the photoelectric effect in tissue is less important compared to the absorption through photoelectric effect in the collimator and in shielding materials [41] Scatter in tissue is dominated by the Compton interaction for the typical energies used in radio-guided surgery. As discussed in section 2.1.2, the trajectory and energy of the scattered photon differs from that of the incoming photon after a Compton scattering event. As a result of its change in direction, the scattered photons travel some distance in tissue and they get further away from the region of interest (the area that contains the activity) before they are detected. Detection of scattered photons can be reduced by using an energy window in the detector, or a good collimator which can substantially eliminate the scatter. [41]

2.4. Challenges during Radio-guided Surgery

In radio-guided surgery when localizing the tumors, a sufficient time of acqusition should be determined since the decays of radioactive sources are random in nature. This means one cannot control the events created by radioactive sources but the integration of these events can be measured over a period of time. In radio-guided surgery this integration time generally varies between 0.5-10 s [41] Considering a typical count rate of 10-30 cps in radio-guided surgery, a targeted area containing weak radioactivity can easily be omitted unintentionally by the surgeon. Smearing the image of radioactivity over an area is generally caused by fast movement of the detection device. Such effects reduce the chance of resolving a weak point of interest from a wide area that contains low radioactivity. Thus, choosing an appropriate integration time over an area is very important, requiring the surgeon to extend the time of detection over structures that potentially contain radioactivity. [41]

Another challenge in radio-guided surgery is known as shine-through. It is a "negative" result of the improper handling of the detector during scanning process. The area that contains the true radioactivity "shines" through the area of shallower tissues. This gives the impression of activity in a region that actually has none and causes the surgeon to mistaken the location of the real structures that contains activity. The solution to this problem is using different angles of measurements by ensuring that the cylindrical axis of the detector is directed to the region of interest for each angle used as seen in Figure 2.7. [41]

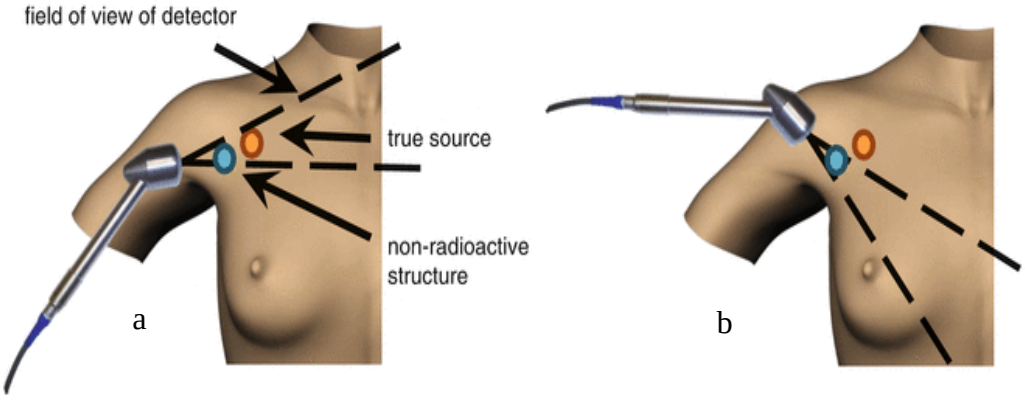

Figure 2.7 (a) A radioactive source is shining through a non-radioactive structure, causing displacement of the true source by a non-radioactive structure. (b) The solution to (a) is using a different angle of measurements by ensuring that the cylindrical axis of the detector directed to the region of interest for the new angle used. (Copied from Wendler et al. with permission) [41]

An opposite effect to shining through is known as shadowing, illustrated in Figure 2.8. In the case of two neighboring structures containing different radioactive intensities, one with a high activity and the other containing a lower activity, the signal from the weaker source is overshadowed by the stronger source. This pitfall of radio-guided surgery has a critical importance for this study, since one of the goals of this project is to resolve sentinel lymph nodes from the tumor that most likely contains a higher activity. The solution to this problem is possible by

carefully adjusting the angle of the detector, thus ensuring that only the weak source is in the field of view of the detector. [41]

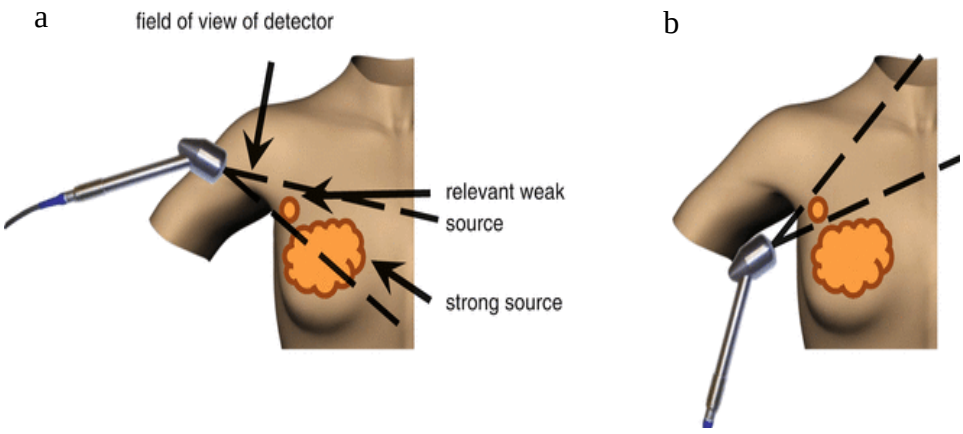

Figure 2.8 (a) a hot source shadowing the weak source causing the weak source undetected by a radiation detector. (b) shows the solution to the shadowing problem in (a) in which the angle of the detector is changed by ensuring that only relevant weak source is in the filed of view of the detector. (Copied from Wendler et al. with permission) [41]

As mentioned in the introduction, one of the the main tasks of this project is to design and develop such a detector so it can handle these potential pitfalls discussed above.

2.5. Characteristics of Breast Tumor and Sentinel Nodes

Radio-guided surgery is a process brought together by combining several important steps: the identification of anatomy of the targeted tissue and neighboring organs, the determination of the characteristics of the tumor and neighbor structures, and the selection of a suitable radionuclide and agent, and identifying and using the best-fit hardware (detector and supporting instruments) based on all the above important steps. The goal of the guidance is to define the center and margins of the tumor and sentinel nodes, surgical removal of the defined volumes, and pathological examination. Evaluation of the tumor and node characteristics is crucial since the detection system is chosen and designed based on the requirements of a specific type of the tumor. One should have a clear knowledge of the typical tumor size, depth and uptake of the specific cancer in order to select proper instruments and methodology so the goal of the process is accomplished. This section includes some literature studies performed to evaluate the size, depth and radioactivity uptake of breast tumor and sentinel nodes.

2.5.1. Characteristics of Occult Breast Tumor Masses

Hruska, O'Connor et al. performed a quantitative breast lesion analysis to determine the size, depth and relative tracer uptake of a breast lesion by using dual-headed, dedicated, breast imaging system comprising two identical opposing cadmium-zinc-telluride (CZT) detectors. The thickness of the breast was measured in over 75 patients, finding the median thickness of the breast

as 6.5 cm and 7 cm for cranio-caudal (CC) views (see Figure 2.9) and mediolateral oblique (MLO) views, respectively. [50]

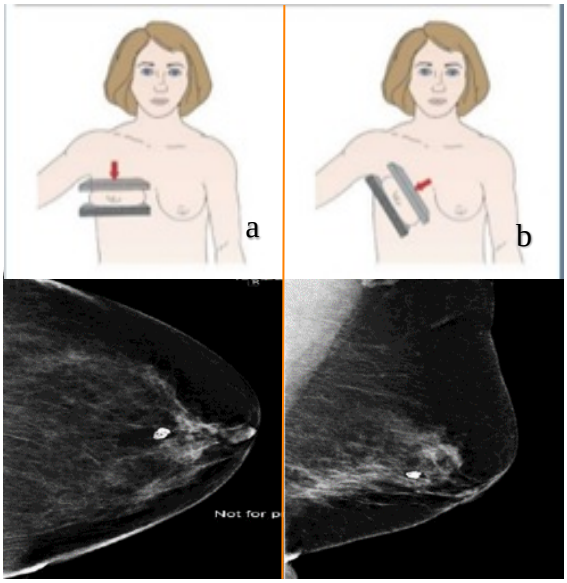

Figure 2.9 (a) Position of the breast and detector and resulting image in CC view. (b) Position of the breast and detector and resulting image in MLO view. (The figure copied from online sources in which no copyright is stated)

Hruska, O'Connor et al. also performed an analysis of the shape of the tumor mass in MBI for 55 cancer patients. Forty-nine out of the 55 were reported to be either in a round or oval shape. By the guidance of the pathological exam results after excision or mastectomy, the sizes of the

oval and round tumor masses were measured with the maximum length observed in all three dimensions. The results showed that the mean tumor sizes in each three dimensions varied between 4-20 mm. A spherical tumor shape approximation was made for those whose standard deviation of the three dimensions was less than 10%, otherwise the shape of the tumor was assumed to be ellipsoidal. [50]In these 49 patients with oval or spherical shaped tumor masses, the ratio of major axis to minor axis varied between 1.0-2.4 with a mean value of 1.5 and a standard deviation value of 0.3. [50]

In another study, the size and mass of the non-palpable tumor in 543 patients had been analyzed clinically with both pathological and mammographic methods. The non-palpable tumor size varied between **0.1-3 cm** and median tumor size was reported as **1 cm.** Both pathological and mammographic appearance showed similar tumor characteristics in terms of mass, calcification and size. [51]

Fortunata et al. performed a prospective study in 77 patients, diagnosed with non-palpable breast tumors, to determine the efficiency of the intraoperative ultrasound localization. The diameter of the tumor in these 77 patients ranged from **4-17 mm** with a median diameter of **9 mm**. The range of the distance from the tumor to the closest tumor margin in 75 out of these 77 patients changed between **0.3-3.2 cm** with a median distance of **1.3 cm**. [52]

2.5.2. Characteristics of Sentinel Nodes in Breast Tumor

One of the recent studies by Waddington et al. estimated the mean dose to the specific organs and tissues after ^{99m} Tc colloidal albumin administration. Subjects were selected from patients recently diagnosed with breast cancer and having clinically lymph node –negative lesions under 5 cm in diameter. Between 10-15 MBq (0.27-0.41 mCi) ^{99m}Tc nanacolloid in a volume of 0.2 ml was injected for all the subjects. An immediate dynamic image and a later image at 16-24 hour post injection were taken. The range of the activities in the lymph nodes was estimated between **0.440 and 2.53 mGy per MBq (or per 0.027 mCi) of injection**. [53]

Pathological findings from a clinical study revealed that the SLN residual activity was about **1 MBq (0.027 mCi)** after 18-24 hours of intratumoral injection. [54, 55]

Bentel et al. measured the maximum depth of supraclavicular (SC) and axillary (AX) lymph nodes on CT images in 49 patients. The maximum depths of SC lymph nodes were found to be 2.4-9.5 cm range with a median for the maximum depth of 4.3 cm. The range of the maximum depth of the axillary lymph nodes varied between **1.4-8 cm,** with a median maximum depth of also **4.3 cm**. [56]

3. Literature Review

3.1. History of Radio-guided Surgery

Sentinel Lymph Node Biopsy for melanoma and breast cancer and intraoperative localization of the lesions containing radiotracers for the surgical dissection of non-palpable breast lesions were all novel clinical applications in early 1990s. [57]In 1960, Earnest A. Gould and his team were the first researchers describing a lymph node in that they “noted at the junction of the anterior and posterior facial vein,” during parotid gland cancer surgery. [57, 58, 59] However, in 1977, Cabanas et al. brought a new concept to the definition of the sentinel nodes by stating that, “Anatomically, clinically, and pathologically it was found that the SLN is the first site of metastasis and may be the only lymph node involved. If SLN biopsies are negative for metastases, no further surgical therapy is immediately indicated.” [57, 60, 58] However, neither Cabanas et al. nor Gould et al. defined the sentinel node in relation to activity changes in the pattern of lymphatic drainage after a radiotracer injection; instead, their definitions were solely based on a static anatomical structure. [57]

In 1993, Alex et al. utilized 14.8 MBq (0.4 mCi) ^{99m}Tc sulfur colloid in 10 melanoma patients through intradermal injection for the localization of sentinel nodes in melanoma by the guidance of an intraoperative handheld, gamma radiation probe. [57, 61, 62] A lymphoscintigraphic procedure was performed between 10 min and 150 min following the injection to evaluate the sentinel lymph nodes pre-operatively followed by a sentinel lymph node biopsy. The handheld gamma probe (C-Trak, Morgan Hill, California, USA) used in the study carrying a NaI scintillation crystal hermetically coupled to a photomultiplier tube and integrated to a unit consisting additional front-end electronics for the read-out of radioactive counts. [57, 61] Alex et al. reported that all sentinel nodes evaluated in all 10 patients by lymphoscintigraphy were identical to those localized by a gamma radiation probe. [61] In the same year, Krag et al. performed a sentinel lymph node biopsy procedure and used the same model probe in 22 breast cancer patients who were intradermally injected with 14.8 MBq (0.4 mCi) ^{99m}Tc sulfur colloid 1-9 hour before the biopsy procedure. [57, 62] Among these 22 patients, sentinel nodes were successfully localized in 18 of them. [57, 62]

In 1996, Cox et al. and his colleagues from the H. Lee Moffitt Cancer Center and Research Institute were the first researchers to introduce intraoperative localization of non-palpable (occult) breast lesions with the guidance of a handheld gamma probe. [57, 63] An intravenous injection of 666 MBq (18 mCi) ^{99m}Tc sestamibi was administered to a patient 1 hour before the surgical procedure. The breast lesion was identified by the intraoperative utilization of a gamma probe and

subsequently the lesion was dissected. [57, 63] This study lead to the development of two techniques for the radio-guided surgical excision of occult breast lesions, using mammographic or ultrasound image guided placement of radionuclides in the occult breast lesion. [57]

The radio-guided Occult Lesion Localization technique was first introduced in 1998 by Luini and Veronesi et al. in which patients diagnosed with non-palpable breast lesions received (3.7 MBq) 0.1 mCi ^{99m}Tc colloidal human serum albumin through intratumorally injection by the guidance of mammographic or ultrasound imaging one day before the surgical procedure followed by a day after surgical excision by the guidance of various intraoperative portable gamma probes. [57, 64, 65]

Not until a year later, the same research group from the H.Lee Moffitt Cancer Center and Research Institute published a first series of papers using a radioactive seed localization technique, in which a ^{125}I source encapsulated in a titanium seed was placed into the center of the breast tumor by the guidance of mammographic or ultrasound imaging 5 days prior to surgery. Intraoperative guidance of a handheld gamma probe was then utilized to localize the center of the breast tumor, and subsequently the spotted tumor site was surgically removed. [18, 57, 66, 67]

3.2. The Use of Intraoperative Gamma Probes in Radio-guided Surgery

Intraoperative handheld gamma probes combined with preoperative imaging techniques including mammography and ultrasound are widely used in radio-guided surgery. [68] After the first implementation of a handheld gamma probe for radio guided surgery by Alex et al. [61] and Krag et. al [62] in 1993, several handheld gamma probes have been developed and made commercially available. Although the goal of all these probes is to guide surgeons in localizing target lesions, they differ in their design, including the choice of detector material, size of the unit, choice of collimation material and collimation geometry, and front-end electronics (pre-amplifier, photomultiplier etc.). [69] The choice of each of these components of the gamma probes are specific to the desired task. It is clear that a success rate of any procedure to localize tumors or SLNs is not solely dependent on the performance of the user during the surgery but also the performance characteristics of the probes utilized. Overall sensitivity, spatial resolution, energy resolution and contrast are the most important variable qualities of a handheld gamma probe. [58, 70, 71, 72, 73, 74]

The overall sensitivity of a probe is the detection ability of the probe from a radioactive source placed at a certain distance along the center axis of the probe tip. The overall sensitivity of a probe is often reported in units of count per second per unit activity of the particular radioactive

source (cps/Mbq). It is simply the rate of the photons detected by the probe to the number of counts emitted from the source per unit time. [58]

The spatial resolution of a probe, which is also known as lateral sensitivity distribution, is the ability of a gamma probe to determine the location of a target source of activity placed at a certain longitudinal and lateral distance from the tip of the gamma probe. [58] The spatial resolution is often given in the unit of full width half maximum (FWHM) in mm. It is the twice of the lateral distance of a radioactive source from the longitudinal axis of a gamma probe at a certain depth, where the detected count rate falls to half of the maximum count rate detected at the same distance. [58] It is a crucial characteristic of a gamma probe when localizing and resolving deep-seated sentinel nodes, specifically when they are close to each other.

Energy resolution, or spectral discrimination, describes the ability of the detection crystal to distinguish between different energies. Good energy resolution of a gamma probe enables discrimination between energies of radioactive sources when simultaneously present in the patient. [58] It is also a critical characteristic since counts due to the scattered photons should be differentiated from the counts due to the primary photons for an accurate mapping of the radioactive distribution of each source. [58]

Contrast is one of the other crucial characteristics of a gamma probe which directly depends on sensitivity, spatial resolution and energy resolution of the probe. [58] In radio-guided surgery,

contrast can be defined as the capability of a gamma probe to distinguish radioactivity in targeted tissue from the activity in surrounding tissues. [58]

To date, no comprehensive review has been reported in the literature comparing the performance characteristics of all commercially available intraoperative handheld gamma probes in the market. Although it is not possible to include and compare all of the gamma probes on the market, Table 3.1 provides comparative information on some important performance characteristics of commonly used, commercially available handheld gamma probes.

Since gamma probes are used intraoperatively, measurements should be taken in a rapid and accurate fashion. Fast and accurate detection does not solely depend on the performance of the probe but is also highly dependent on the user. [68] Accurate handling of the probe during the surgery is required for a precise detection. In addition to challenges discussed in section 2.4, shadowing and shine-through challenges the localization of some of the SLNs with the intraoperative gamma probes, specifically, when SLNs are deeply seated in the breast and have a low radioactivity uptakes, they might be missed by the surgeon because of the attenuation in the tissue. [68]

Table 3.1 Comparision of the physical and performance characteristics of some of the gamma probes in the market. Most of the values on the table were taken from Zamburlinia et al. [69], Kaviani et al. [75], Van Eijk, et al. [76, 77, 78], Dorenbos et al. [79], Garnier et al. [80], Syntfeld et al. [81], D Alexiev et al. [82], Alharbi et al. [83].

	C-Trak Omniprobe		**Europrobe**		**Neoprobe**	**Node Seeker**	**Navigator**		**γ-Locator**	**Surgeo guide**
Type	Normal Collimator	Lechner Collimator	Large	Small	with Collimator	Bent-tip	No collimator	with collimator	F8-R6	with Collimator
Detector Material	CsI(TI) PMT	CsI(TI) PMT	Cs(I)TI (SiPM)	CdTe	CdZnTe	LYSO	CdTe	CdTe	CsI(TI)	CsI(TI)
Head Diameter (mm)	15	15	16	11	17	14	14	14	23	16
Aperture Diameter (mm)	6.8	n/a	5	5	9	n/a	n/a	7	n/a	7.5
Weight (gr)	190	199	150	104	160	133	182	182	330	185
Literature % Energy Resolution of the detector material at 662 keV	6.20%	6.20%	6.20%	1.80%	1.8-5.1%	7.40%	1.80%	1.80%	6.20%	6.20%
Literature % Energy Resolution of the detector material at 140 keV	≤25 %	≤25 %	20.20%	n/a	n/a	n/a	n/a	n/a	≤25 %	≤25 %
Sensitivity in Air at (cps/MBq) at 3 cm	1500	850	1240	284	2200	2300	510	510	200	1700
Sensitivity in Air at (cps/MBq) at 5 cm	680	380	560	121	800	940	210	n/a	28	n/a
Spatial Resolution FWHM (mm) at 3 cm	28	19	22	21.12	53	37	35	35	37	45
% Maximum Side and Back Shielding Leakage	0.020	0.020	0.001	0.001	2.000	2.000	0.030	0.030	0.000	0.500
References	[69, 75-80]	[69, 75-80]	[69, 76-81]	[69, 81, 82]	[69, 75, 81, 82]	[69, 76, 77, 78]	[69, 82, 83]	[69, 82, 83]	[69, 75-80]	[69, 75-80]

3.3. Intraoperative 2D Gamma Cameras for Radio-guided Surgery

In order to address the obstacles and challenges of intraoperative gamma probes discussed in Section 2.4 and 3.2, intraoperative gamma cameras have been developed and used for radio-guided surgery. Intraoperative use of these imaging systems requires some features, including but not limited to: portability in the operating room, rapid acquisition and display, continuous monitoring, measurements in real time, fine spatial resolution, high energy resolution and high sensitivity. [68]

Two-dimensional gamma cameras in radio-guided surgery differ based on their design. They can be either mobile (or portable) or handheld. If the detector unit used in the camera system is less than 1-2 kg in weight, which can be easily handled by an average person for the typical acquisition time required, ~ 1 min, then the unit does not require a backing or support system and can be used in handheld fashion, called a handheld gamma camera. If the unit is heavier, the unit requires some support structure and is referred to as a portable or mobile gamma cameras. [68] No matter the design, the common goal is to map the distribution of the radionuclides by providing real-time, 2D scintigraphy images intraoperatively. [84, 85, 86, 87] The field of view provided by mobile gamma cameras is variable as they can be designed to provide either a small field of view (SFOW) such as 5.0x5.0 cm^2 or large field of view (LFOV) up to 40x30 cm^2. [84, 85, 86] The

image quality of these mobile or handheld gamma cameras is the same as that of gantry based preoperative conventional gamma cameras [84, 88] except for a difference in coverage because of the bigger sizes of some conventional gamma cameras providing larger field of views than the mobile or handheld units. [84, 88]

Table 3.2 compares important physical and performance characteristics of most of the portable or handheld gamma cameras in the market and literature. The major contribution to the table is from Hellingman et al [68] and Tsuchimochi et al. [89]

Table 3.2 A comprehensive comparission of the physical and performance characteristics of the intraoperative gamma cameras available in the market and literature.

Brand	**CarollRes** [68, 89, 151, 152, 153]	**CGC** [68, 155]	**Crystal Cam** [68, 156]	**Ergo** [68, 157]	**Ez-Scope** [68, 89, 157]	**Gamma CAM** [68, 159]	**GE Camera** [89, 161, 162]	**Imaging Probe** [89, 160]	**IP Guardian II** [68, 163]	**Luma GEM** [89, 173]	**Medi PROBE** [89, 164, 165]	**Minicam** [89]	**Minicam II** [68, 89]	**NODE VIEWTM** [68, 166]	**POCI 2nd** [68, 89, 157, 167]	**POCI** [89, 167]	**Sentinella S102** [68, 89] [169, 189]	**SSGC Prototype** [89, 171, 170]	**SSGC Clinical** [89, 172]
Physical and Design Charecteristics																			
Type	Portable	Handheld	Handheld	Portable	Handheld	Portable	Handheld	Portable	Handheld	n/a	n/a	Handheld	Handheld	Handheld	Handheld	Handheld	Portable	Portable	Portable
Detector Material	Gd2SO5(Ce)	CsI(Tl)	CdZnTe	CsI(Tl)	CdZnTe	NaI(Tl)	CdZnTe	CsI(Tl)	CsI(Tl)	CsI(Na)	CdTe	CdTe	CdTe	NaI(Tl)	CsI(Na)	YAP(Ce)	Cs(Na)	CdTe	CdTe
Det. Head size (mm3)	78x78x275	Ø 95X200	60x60x140	421X284X102	60X60X220	n/a	Height 150	n/a	n/a	n/a	200x70x30	Ø95x150	70x170x250	64X64X76	Ø95X90	Ø24mm	154X80X82	152x166x65	82x86x205
Weight (g)	2490	1000	800	19300	800	10000	1200	2000	1200	n/a	1500	n/a	700	1100	1200	2000	1300	2700	1400
Collimator type	Parallel hole	Pinhole	Parallel hole	Parallel hole	Parallel hole	Parallel hole	Parallel hole	Parallel hole	Parallel hole	Parallel hole	pinhole	Parallel hole	Parallel hole	Parallel hole	Parallel hole	Parallel hole	Pinhole	Parallel hole	Parallel hole
PMT Type	PS-PMT	CCD	n/a	PS-PD	n/a	PS-PMT	n/a	PS-PMT	PS-PMT	PS-PMT	n/a	n/a	n/a	PS-PMT	PS-PD	IPSD	PS-PMT	n/a	n/a
Performance Characteristics																			
Image Matrix size	300x300	125x125	16x16	512x512	16x16	n/a	16x16	20x20	18x18	16x16	256x256	16x16	16x16	29x29	50x50	n/a	300x300	32x32	32x32
FOV (mm2)	40x40	8x8	40x40	396x310	32x32	125x125	40x40	49x49	44x44	20x20	14.08x 14.08	49x49	40x40	50x50	Ø 40mm	Ø 24mm	40x40	44.8x44.8	44.8x44.8
System Spatial Res. (mm)	10 mm at 3cm	1.28-2.9mm at 13-50 mm	3.8-4.9 mm at 25-50 mm	10.3 mm at 100mm	2.3-8 mm at (10-50mm)	n/a	5mm at 50mm	n/a	2.5-2.9 at 0-15mm	2.1 mm at 0 mm, 2.6 mm at 30mm	5.6-12.6mm at 50mm	5%	2.46 mm at 0mm	1.8 mm at 6mm	3.9-76 mm at (10-50 mm)	1.9 mm at 0mm	5.4-8.2 at 30mm 7.3-11 at 50mm 10-18 at 100mm	1.6 at 0mm 3.9 at 25mm 6.3 at 50mm 11.2 at 100 mm	1.5 at 0mm 2.3 at 25mm 3.4 at 50mm 6.8 at 100 mm
Sensitivity (cps/MBq)	1000 at 0 cm	214 at 3mm	237-554 at 0 cm	113 at 0cm	184-477 at 0cm	61 at 0cm	100 at 0cm	210 at 0cm	204 at 0cm	n/a	6.5-3.3 at 0cm	n/a	n/a	135 at 0cm	290 at 0cm	200 at 0cm	27-72* at 0mm	300 at 0cm	150 at 0 mm
% FWHM at 140keV	45 % at 122 keV	58%	5.20%	7.90%	8.60%	n/a	8%	20%	20%	> 20%	n/a	n/a	5-7 %	12%	32%	38%	15.90%	7.80%	6.90%

*High resolution low sensitivity collimation,

n/a: Not available or missing information,

PMT: Photo Multiplier Tube, IPSD: Intensified Position Sensitive Diode, PS-PMT: Position Sensitive Photo Multiplier Tube, PS-PD: Position Sensitive Photo Diode, CCD: Charge Coupled detector.

3.4. Three-Dimensional Intraoperative Image Guidance and Freehand SPECT

Wendler et al. and his colleagues from Computer Aided Medical Procedures (CAMP, TUM, Munich Germany) published a series of articles in 2007, which were mostly about the feasibility of 3D intraoperative imaging of radioactive distributions using a three-dimensional optical tracking system based on an optical sensor and a camera to track gamma probe. In one of their first publications, they reported that localizing liver metastases in real time using the combined power of ultrasound and a tracked gamma probe is feasible. [90] The gamma probe used in this study was NodeSeeker (See Table 3.1) with a custom-made collimation. [90] In the same year, Wendler et al. and his colleagues performed some radioactive measurements in a phantom with the same gamma probe that they used in their previous study. [91] However, this time the goal was to test the feasibility of imaging the 3D radioactive distributions of ^{99m}Tc in the phantom by using the tracked gamma probe intraoperatively. [91] They reported that the reconstructed images, which were generated by combining tracked gamma probe count data and associated position and orientation of the probe, were comparable to those of a conventional SPECT system. [91] In 2010, the same group conducted a feasibility study to integrate this system to the clinical settings in localizing SLNs for breast cancer. This was the first time a group performed 3D lymphatic mapping intraoperatively using a standard gamma probe and an optical system to track

the probe and patient. [84, 92] The results were then compared to the SPECT-CT images and found to be promising, although the system had some issues to be solved. [92]

After the first application of this system into the clinical settings, Valdes, Sicart and Nieweg et al. published an editorial commentary which specifically focused on introducing the 3D intraoperative image guidance system developed by Wendler et al. [84, 93] Subsequently, this 3D image guidance system was named Freehand SPECT (fhSPECT declipse® SPECT; SurgicEye, Munich Germany) and became commercially available in Europe and the United States in 2009 and 2011, respectively. [84, 94]

3.4.1. Freehand SPECT System

The freehand SPECT device is augmented by a three-dimensional tracking system that tracks the position and orientation of the optically fitted patient and handheld gamma detection probe (HGDP) or small field of view gamma camera (SFOV GC) by using a pair of video cameras. The operator moves the freehand SPECT device around the patient by hand. Location and orientation data from the tracking system is combined with the counts measured by HGDP or GC to produce planar images of the radiation intensity and three-dimensional images of spots with the highest counts measured. A 1 to 2 minutes scan produces a 3D SPECT image. The results can then be seen on a video image of the patient with the help of a third camera which is located between the two cameras that track orientation and the position of the probe.

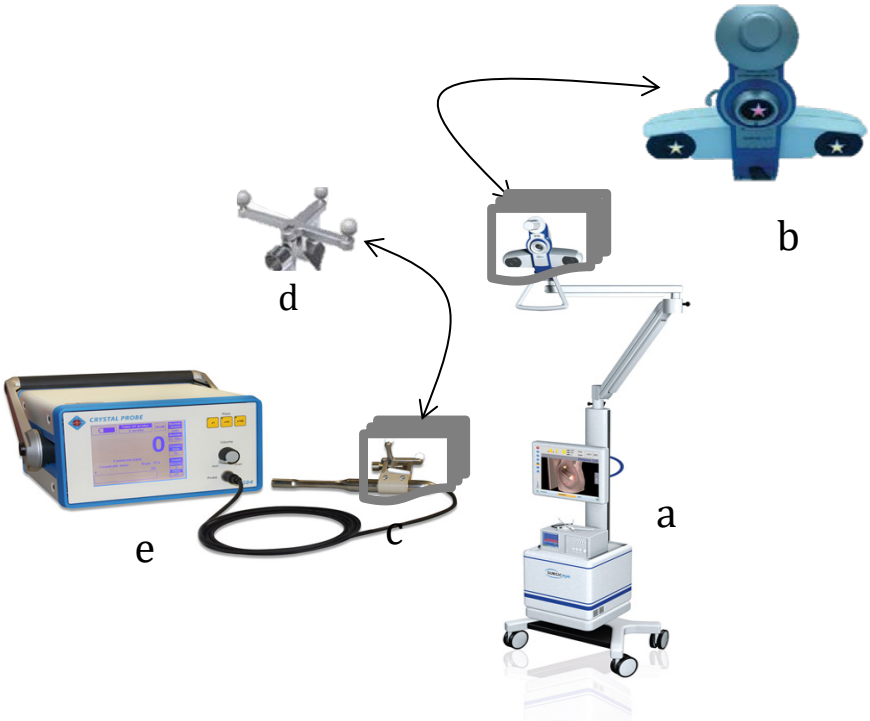

Figure 3.1 Graphical expression of the Freehand SPECT system (a) the main unit holding the image processing computer system, touchscreen monitor and tracking system. (b) The tracking unit contains an optical camera sensor in the middle (red star) and two Infrared (IR) camera sensors on the sides (yellow stars), all mounted to the head of the main unit within a moveable arm. (c) The standard gamma detection probe and corresponding fiducial tracking targets (d) areintegrated to both HGDP and the patient. (e) The conventional output unit of the HGDP. (The pictures copied from Bluemel et al. [84] and the manufacturer's website [94], with permission and the pictures were modified for an improved representation of the system)

The fhSPECT system comes with a main unit holding the reconstruction computer system and touchscreen output monitor which integrated to a moveable arm module containing an overhead unit with an optical video camera in the middle and two IR stereo cameras on the sides as seen on Figure 3.1. The system is integrated to a HGDP or a GC in order to detect radiation emitted from the previously injected radiotracer. Patient and HGDP are tracked by an infrared (IR) system through two fiducial tracking targets, one secured to HGDP and the other on the patient. [84] The system does not use any robotic or gantry-based module to move the HGDP over the region of the interest but has the user holding and moving the probe over the ROI systematically. The count measurements provided by HGDP are combined with the tracking data provided by tracking system and together processed in a reconstruction algorithm to create a 3D distribution of the radiotracer within the surgical field. [84] Since the distribution can be measured and tracked in all dimensions, the depth information of the lesions containing radioactivity can be presented as well. Thanks to utilization of the augmented reality overlay with video camera images (denoted as red star in Figure 3.1), the reconstructed image of the radioactivity distribution within the surgical field can be seen on the touchscreen monitor. [84]

3.4.2. Literature Review on Freehand SPECT Studies coupled with Handheld Gamma Detection Probes

In 2014, Pouw et al. performed a feasibility study that compared conventional US-guided intratumorally injection of ^{99m}Tc-nanocolloid for patients having non-palpable breast tumor scheduled for SLNB, to Freehand SPECT-guided injection of the same radiotracer to the same patients with non-palpable tumors having a ^{125}I brachytherapy source inserted into the tumor preoperatively. [95] The Freehand SPECT system was coupled with a standard HGDP. The depth difference between the center of the ^{99m}Tc-nanocolloid and ^{125}I source was measured by the guidance of US and Freehand SPECT, separately. Then, the results were compared to each other. The average difference in the depth measured by Freehand SPECT was found to be 10.9±6.8 mm in 34 patients. [95] On the other hand, the average depth difference measured by US was 9.7±6.5 mm in 21 patients. [95] Although the depth measured by the two methods is not the same, the author reported that an injection with Freehand SPECT guide may be possible. [95]

In an another study performed in 2014, Fressmeyer et al. analyzed the feasibility of using hybrid imaging of Freehand SPECT and Ultrasonography (US) in patients diagnosed with thyroid cancer. [96] The authors state that the maximum spatial resolution of the Freehand SPECT system was measured at 13 mm, although the manufacturer's reported resolution was 5 mm at the same distance. [96] The authors highlight that, although the goal of their study is to test the feasibility of fusion imaging and their findings are positive for that goal, 13 mm spatial resolution of Freehand

SPECT at depth is not sufficient to localize small thyroid structures, especially when they contain varying amounts of radioactivity. [96]

Pouw et al., from the University of Amsterdam,investigated the ability and accuracy of Freehand SPECT, using a standard HGDP to predict surgical margins in breast tumors in a 2016 study. [97] In 10 patients diagnosed with non-palpable breast tumors, I-125 sources were implanted as part of RSL. The resected tumor specimens were scanned using a freehand SPECT system to measure the distance between the face of the resected tumor specimen resection plane and the ^{125}I source. [97] The distance measurements provided by Freehand SPECT were then compared to those provided by CT images of the same tumor specimens. The mean difference between Freehand SPECT and CT measurements were reported as 2.9 mm, having a standard deviation of 2.7 mm. [97]

3.4.3. Literature Review on Freehand SPECT with Small Filed of View Gamma Camera

The first use of the Freehand SPECT in conjunction with a small field of view gamma camera (SFOV GC) was reported by Matthies et al. in 2013. [98] The mini gamma camera utilized in this study was provided by CrystalPhotonics, Germany. The mini camera hada 16 x 16 pixels^2, 4x4 cm^2 CdZnTe detection crystal with a tungsten and lead collimator. [98] However, in this study the gamma camera was not used in freehand fashion, it was mounted on a robotic arm to compare

image quality provided by the robotic-arm SPECT system with a conventional freehand SPECT system. [98] The result showed the robotic-arm SPECT system provided better quality images and faster data acquisition compared to conventional Freehand SPECT system. The reason for the improvement was attributed to optimized acquisition trajectories. [98]

In 2016, Engelen et al. performed a comprehensive phantom and clinical study in order to test the performance of the Freehand SPECT system using a mobile compact gamma camera (MGC) in localizing sentinel nodes in breast tumor. [54] The phantom study included determination of sensitivity and resolvability of the Freehand SPECT-MGC hybrid system at various source to detector distances and using different injection site-to-sentinel node distances. The clinical study, on the other side, determined the sensitivity and resolvability of the Freehand SPECT-MGC system in 10 breast cancer patients for various source to detector and injection site-SN distances. The results were than compared to conventional gamma camera lymphoscintigrams. Detection sensitivity in the phantom study revealed that, while the three-dimensional Freehand SPECT mobile gamma camera system (3D-FHS-MGC) was able to detect minimum SN activities of 0.08 (2.2 μCi) MBq at 36 mm source to detector distance, the 2D-flatbed imaging system was able to detect minimum SN activities of as low as 0.02 (0.55 μCi) MBq at the same source to detector distance. [54] Resolvability experiments in phantoms of 3D-FHS-MGC investigated spatial resolution and resolvability, when SNs at depth are placed in close proximity to each other. Neither the 3D-FHS-MGC system nor the 2D flatbed imaging system was able to resolve a SN

placed 10 mm from the injection site at 60-mm source to detector distance. [54] Although 2D-Flatbed imaging resolved a SN 20 mm from the injection site and 60 mm from the detector, the 3D-FHS-MGC system failed to resolve this SN. [54] The phantom clustered-nodes resolvability experiment showed that four sentinel nodes separated by 10 mm at about 40 mm depth were not distinguished by the 3D-FHS-MGC system unless each source contains relatively high activity (25MBq and up) and was located at only 4-mm source-to-detector depth. In a clinical resolvability study, on the other hand, it was found that two axillary nodes separated by 11 mm and each containing different activity were not identified and distinguished by the 3D-FHS-MGC but were resolved by the 2D Flatbed imaging system. [54] The authors concluded that it was not possible to distinguish a lymph node containing low activities when a higher activity node is nearby. The 3D system was also not able to resolve lymph nodes in close proximity at depth due to the poor spatial resolution of the MGC. [54]

3.4.4. Summary of the Limitations of the Freehand SPECT System

Despite the innovations brought by the Freehand SPECT system, there are still several issues that need to be improved for a more effective utilization of the system in radio-guided surgery. First and foremost, although freehand SPECT was initially intended to be used in real-time fashion, the 3D image guidance provided in the operating room (OR), is not truly a real-time measurement. [84, 99] This is because any alteration of the target sites within the ROI, or any

movement of the patient during the surgical procedure, requires repetition of the whole 3D-image creation procedure including the scanning and reconstruction process. [84] Hence, the Freehand SPECT measurements could only be referred to as a true real-time fashion when there is no movement of the target structures within the ROI and no change in the position of the patient observed during the surgical procedure. [84, 99]

Secondly, no matter if the Freehand SPECT is used in conjunction with either HGDP or SFOV GC, the resolvability of small clustered lymph nodes containing different activity uptakes at depth is always problematic due to the poor spatial resolution of HGDP [96] or SFOV GC [54].

Moreover, according to Bluemel et al., accurate depth measurements of the target lesions in the reconstructed 3D volume are limited when the freehand SPECT device is coupled with a handheld SFOV GC. [84]

As discussed in Section 3.4.3, another limitation of the Freehand SPECT system that uses SFOV GC is the inability of resolving lymph nodes, specifically when they are located less than 20 mm distance from the injection sites at typical lymph-node depth due to the shadowing effect caused by poor spatial resolution of the collimated GC. [84, 54]

Last but not the least, Freehand SPECT coupled to either HGDP or SFOV GC is unable to determine the surgical margins of the breast tumor accurately. This is mostly because the ^{125}I radioactive source implanted into the center of the tumor for the localization of the breast tumor

by the Freehand SPECT system provides no information about the margins of the tumor but only the center of the tumor. Using multiple radioactive seeds implanted to the tumor site still does not provide precise information about the extent of the tumor as discussed in the study performed by Pouw et al., explained in Section 3.4.2. [100]

3.5. Motivation for the Project

The current techniques to treat breast cancer offer some options to the patient under certain circumstances. If the patient's diagnostic and physiological characteristics meet certain requirements, the patient is then given an opportunity to choose among different treatment plans, including, but not limited to, total removal of the breast (mastectomy) or breast conserving surgery (lumpectomy) followed by radiation therapy as discussed in Section 1.2. Each treatment technique brings their own advantages and drawbacks. Although the total mastectomy ends up with permanent loss of the breast, it has slightly less risk of growing a local recurrence of the cancer cells compared to lumpectomy except when lumpectomy is followed by radiation therapy. [101] Depending on how comprehensive the excision of the tumor was, lumpectomy however saves the breast partially or entirely. It is easier to reconstruct the breast after partial breast conserving surgery. However, if lumpectomy is followed by radiation therapy, there is a high possibility to delay breast reconstruction to avoid potential postoperative complications. [102] The deciding factors are specific to each patient. During lumpectomy operation, the tumor and some surrounding

tissue (margins) is removed by the surgeon. Pathological examination then provides information about how clear the margins are of cancer cells after the surgery. If the margins are all clear, then the operation is completed. Ideally, the tumor and margins are all cleared at the first lumpectomy attempt. However, this is often not the case. Even the pathological examination itself takes about a week after the lumpectomy for the definitive report that could lead to having additional surgery performed. This is called re-excision lumpectomy or simply re-excision.

Non-palpable tumor localization has always been a challenge for surgeons. The discussion in Section 1.4 clearly explains that neither the traditional tumor localization method known as wire guided localization (WGL) nor the most commonly used technique known as radioactive seed localization (RSL) can provide a detailed information about the extent of the tumor. The source can only indicate the center of the tumor and possibly provide a few local points in the tissue around the tumor. Thus, the output from both WGL and RSL is very coarse. In addition, intraoperative three-dimensional image guidance is not available in either of these two localization methods, because the hardware (probes) used and the localization method applied in both cannot achieve such guidance. In other words, they are not intended to visually guide the surgeon during the procedure. Several studies with different localization methods and different instrumentation have been performed over the years with attempts to provide better guidance to the surgeons. The outcomes from these studies contributed to the localization procedure in terms

of scheduled interventional appointments, staff time and patient wait times. Nevertheless, no considerable decrease in re-excision and re-operation rates has been observed. [103]

The freehand SPECT device Declipse®SPECT (see Section 3.4.4) comes with an optical 3D tracking system which allows surgeon to visualize the radioactivity distribution of the tumor on a static video image with three-dimensional view. [84, 94] Despite the novel innovation of the system, it still has limitations that need to be addressed for the precise localization of breast tumor and associated sentinel node intraoperatively. As discussed in Section 3.4.4, these limitations can be summarized as followings:

(1) Freehand SPECT coupled to either SFOV GC or HGDP is unable to resolve clustered lymph nodes at depth which is mainly due to low spatial resolution of the detector. [54]

(2) Due to the shadowing effect caused by poor spatial resolution of the detection device, the Freehand SPECT system has difficulties distinguishing and resolving lymph nodes from the radiotracer injection site if lymph-node-injection-site distance is less than 20 mm at depth. [54]

(3) Additionally, in the same manner as in RSL, the Freehand SPECT device does not obtain information about the extent of the tumor. It is more focused on the localization of the sentinel lymph node by using the ^{99m}Tc source and localization of the tumor by using multiple ^{125}I brachytherapy sources. Using multiple radioactive seeds to obtain information about the margins of the tumor, still does not provide precise tumor margins information. In both procedures, the

system has its limitations because of the imaging methodology and poor spatial resolution of the detector at depth. [100] [54]

(4) Lastly, the three-dimensional image produced and projected onto the patient may be blurred since the system does not respond to the movement of target lesion sites or the movement of the patient during the surgery. [84] Thus, the resultant image does not register to the ROI and the patient as patient moves. [84]

The following subsections will discuss how this project proposes to handle these limitations of the conventional tumor localization methods and Freehand SPECT system.

3.5.1. CLR1404 Imaging Agent and Imaging of the Breast Tumor

Unlike WGL, RSL, radio-occult-lesion-localization (ROLL) or Freehand SPECT that uses ^{125}I radioactive seeds or intratumorally injection of ^{99m}Tc albumin nanocolloid or ^{99m}Tc nanocolloid to obtain information about the tumor, this project proposes a breast tumor-seeking imaging agent, such as CLR1404. CLR1404 is a tumor-targeted radioiodinated alkylphosphocholine (APC) analog which was recently developed by Cellectar Biosciences Inc, Madison, WI. Depending on the isotope of the Iodine used in conjunction with this analog, it can be utilized as an imaging agent, i.e.,^{124}I or as a radio-therapeutic agent, i.e., ^{131}I. [104]

According to a translational study performed by Weichert et al. from the University of Wisconsin-Madison, as the result of testing selective uptake and retention of radioiodinated ^{124}I-

CLR1404 imaging agent in 57 different spontaneous, transgenic, human and rodent malignant cells and tumor types, the agent is taken up and retained by almost all primary and metastatic malignant tumors, including all breast tumors, no matter where the tumor anatomically resides in the body. While the uptake in tumor cells is found to be high, no considerable uptake from normal cells is observed. [104] Another study reported by Grudzinski et al. tested the targeted therapeutic efficacy of the ^{125}I-CLR1404 in rodents with triple-negative breast cancer (TNBC). The agent was found to be significantly efficacious against (in vivo) metastatic TNBC models.

No clinical or theoretical study has been found in the literature that uses CLR1404 in conjunction with ^{123}I. However, since the chemical structure of CLR1404 is suitable with iodine coupling (having a radioiodinated APC analog), there should be no problem in labelling any isotope of iodine to CLR1404. Iodine-123 is chosen because it is the radioisotope of Iodine which makes it suitable to be used with CLR1404 and is useful in intraoperative medical imaging because of its short half-life, mono energetic gamma emission, i.e., 159 keV with 0.83 emission probability. In summary, injection of ^{123}I-CLR1404 radiotracer would allow imaging the entire tumor and localize it with the margins, which is not possible in RSL or Freehand SPECT procedures.

3.5.2. SLN Localization and Detector Technology

In addition to the utilization of ^{123}I to localize the entire tumor, this project aims to use a ^{99m}Tc based molecular agent through injection in order to localize SLNs. As discussed in Section

3.4.3 and 3.4.4, the freehand SPECT system has difficulties distinguishing clustered lymph nodes because of the low spatial resolution of the detector used in the probe or gamma camera. Although the agent for nodal localization will be same as in RSL and Freehand SPECT, the detector to localize ^{123}I and ^{99m}Tc sources will be totally different in terms of its design and characteristics.

The proposed procedure uses ^{123}I to localize the tumor cells and ^{99m}Tc to identify the lymph nodes. The energy of these radionuclides, as discussed in later chapters, are very close and require a new detector to differentiate and localize radiation from each source. The detector will also have to have high sensitivity. The spatial resolution, which is the most problematic characteristic of the detector used in Freehand SPECT system, has to be sufficient for accurate depth identification. The main task of this study is to design and develop this detector so the characteristics in terms of sensitivity, energy resolution and spatial resolution will be adequate to the application.

3.5.3. Overview and Future Objectives

In the long-term vision of the project, the image of the radiation fields will be viewable by surgeon on a clear, heads-up, augmented reality visor allowing the surgeon to view patient with the reconstructed image of tumor and nodes superimposed in the patient (see Future Work). The image projected will remain registered as the surgeon moves. By providing information about the edges of the tumor, the project is expected to reduce the probability of having positive margins following first breast-conserving surgery. Since the CLR1404 imaging agent is found to be taken

up by almost all types of cancer cells not just by breast cancer cells [104], the procedure would be beneficial for patients diagnosed with any type of non-palpable tumor by guiding surgeon to remove tumor at the first attempt, providing adequate tumor-free margins. The surgical outcomes in terms of clear tumor margins, re-excision, reoperation rates would be potentially improved with this approach. Moreover, the approach can offer some considerable improvements in workflow in relation to patient wait time, and staff time.

Part II. Contribution to the Research Problem

4. Design and Development of the Detector Technology

4.1. Introduction

Identifying edges of a tumor is one of the key points to improve the precision of tumor localization in breast-conserving surgery. As noted in the previous chapter, the most recent work (Freehand SPECT), uses a ^{125}I brachytherapy source and ^{99m}Tc colloidal suspension through injection to locate the tumor and sentinel lymph nodes respectively. Nevertheless, ^{125}I radioactive seed does not offer any information about the extent of the tumor. This project uses CLR1404 labelled with ^{123}I to identify the whole tumor and ^{99m}Tc labelled nanoparticles to locate SNs. Hence, the detector selection, in terms of both its components (detector type, collimation type, and front-end electronics including photo multiplier type) and its characteristics (detector thickness, width, energy resolution, detection efficiency, sensitivity and decay time), is very important. The selected detection crystal must quickly distinguish between radiation coming from ^{123}I and ^{99m}Tc

sources, through good energy discrimination and a short decay time, have a high light yield and short wavelength of maximum emission. If the selected crystal is a scintillator, selection of the photon multiplication device is another important component as part of a compact and efficient photomultiplier device. This chapter discusses design characteristics and development of the detector unit based on the performance characteristics needed to accomplish the goal of this work.

4.2. Determination of the Detection Crystal

4.2.1. Radioisotopes and Their Decay Schemes

In this project, as discussed earlier, the patient will be injected with CLR1404 labeled with ^{123}I to image entire tumor. The patient will also receive nanoparticles labeled with ^{99m}Tc through injection near the tumor to localize SNs. I-123 is the isotope of iodine with 13.224 [105, 106] hours of radiological, 120-138 days [107] (unbound-iodine) of biological and 12 hours of effective half-lives. [107] It is a good research tool to use in medical imaging because of its short half-life, ability to provide clear SPECT images and ease of use. As seen on Figure 4.1 (a), a mono energetic neutrino at 1.070 MeV (97%) accompanies the decay of ^{123}I by electron capture, resulting in ^{123}Te. The transition leaves ^{123}Te in an excited state. A 159-keV gamma photon with emission probability of 83% is then emitted by de-excitation of ^{123m}Te.

Tc-99m is the other radionuclide utilized in this project. It is one of the most commonly used medical imaging radionuclides due to its relatively short physical half-life (6.007 h). [105, 106] It is produced from ^{99}Mo, which has a half-life of 66 hours. [108] In previous studies, nanoparticles labeled with ^{99m}Tc have been shown to be a suitable imaging agent in detecting sentinel lymph nodes for patients diagnosed with breast tumor. [109] Figure 4.1 (b) shows the decay scheme of ^{99m}Tc. It de-excites to ground state of ^{99}Tc by emitting a 141 keV gamma photon with 0.89 branching ratio.

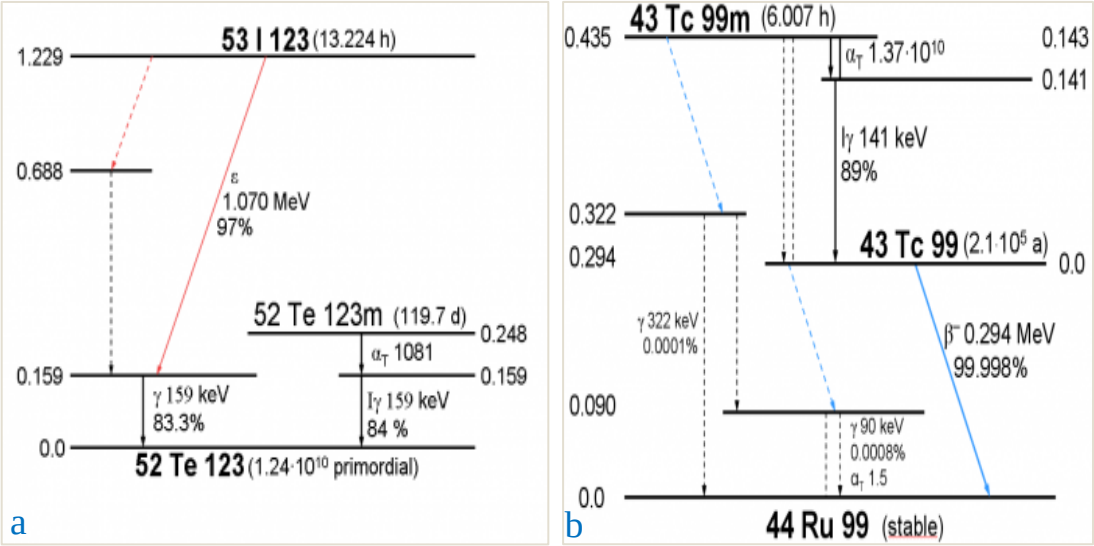

Figure 4.1 (a) Decay scheme of ^{123}I (b) Decay scheme of the ^{99m}Tc. Figures extracted from [105, 106] with permission.

4.2.2. Detector Materials

Detectors used as spectrometers can be divided into three main categories based on their working principles: gas detectors, scintillation detectors and semi-conductor detectors. They can be used alone or as a combination regarding to aim of the task. The most important characteristics of an intraoperative radiation detector used in localization of SLNs and tumors are detection efficiency, energy resolution and spatial resolution. An optimum probe in practice, of course, would have the highest detection efficiency, best energy resolution and finest spatial resolution. However, having these best performance characteristics all together in a detector would not be possible. Therefore, the optimum performance parameters of a detector are application specific. [86]

This project requires a detection crystal with adequate energy resolution to differentiate between the 159-keV gamma from ^{123}I and the 141-keV from ^{99m}Tc. These two energies are very close to each other and they are relatively low. The percent energy resolution degrades as the energy decreases, which makes the inherent energy resolution at low energies a very important characteristic of the detector. However, having a good energy resolution alone will not be enough. In order to detect sufficient radiation coming from the sources to create images, the detection efficiency (sensitivity) also must be high. This is particularly true in order to image the margin of the tumor where the tumor cell population decreases. A fine spatial resolution is needed for both determining the edge of the tumor and localization of small lymph nodes. The detector needs a

high sensitivity to provide information about the specific sites of the tumor while offering a rapid search over large surgical fields. [110] Pulse pile-up is one of the potential problems for a radiation detector. It occurs when there is a significant probability that more than one particle interacts in the detector within the detector resolving time. Insufficient resolving time of the detector causes a distortion of measured pulse-height spectrum. Therefore, a fast resolving time is required to minimize pulse pile-up on the measured spectrum. The detector also needs a small size to be compact and light, a good linearity of response, a high light yield (output), a low internal activity (background) and dark current.

Gamma-ray detection and spectroscopy are often use one of two materials: inorganic (non-plastic) scintillators and semiconductors. Gas filled detectors are compact, low cost and good for room temperature operation; however, high-voltage and delicate components are needed for operation. In addition, they are incapable of providing the required spectroscopic information. [111] In scintillation detectors, a gamma or x ray interacting in the crystal produces a traveling electron. As the electron moves through the crystal, it interacts with the atoms through ionization and excitation, which, through de-excitation, results in visible light that is then converted to an electrical pulse in a photomultiplier. In semiconductor detectors, ionization produced by the radiation produces free electrons that are then collected as an electrical pulse.

Scintillators are generally low cost, small, and easier to grow materials. They exhibit high gamma-detection efficiency and fast-timing characteristics. Semiconductor detectors, on the other

hand, are known for their small size, rugged structure, high energy resolution and good spectroscopic capability. However, they tend to be expensive materials for larger detectors, which would be required for a high sensitivity. Cadmium Zinc Telluride (CdZnTe or CZT) is widely used in RSL practice, albeit at a high cost. [111] Some of the most recent intraoperative imaging probes which use CZT and Cadmium Telluride (CdTe) semiconductor materials are: **Gammed** (Capintec Inc NJ, USA), **Gamma Finder® (**Silicon Instruments GmbH, Germany Subsidiary SenoRx Inc. CA, USA), **Navigator™** (RMD instruments LLC, MA, USA) and, **Neoprobe** (Neoprobe corp. OH, USA).

A wide literature review was conducted to find an optimal detector material for this project in terms of some important characteristics discussed above. Table 4.1 shows the comparison of detector materials that are used in gamma spectroscopy. Among the wide selection of detector materials shown on Table 4.1, the detector materials listed in bold font can be considered as the most promising ones based on their performance characteristics.

CZT crystals are widely used for gamma spectroscopy in medical purposes as mentioned earlier. The very small volume (<1.0 cm^3) of CZT detectors provides excellent energy resolution performance, i.e., < 2% at 662 keV. [81] However, the performance of the CZT is limited by the small size of the crystal, since they are harder to grow and become expensive for larger sizes. [81] The smaller the active surface area of the CZT crystal results in a lower the detection efficiency. However, as the size of the crystal increases, the energy resolution becomes poorer. [81] As a

comparison, A CZT crystal with 5.445 cm^3 volume (the largest volume available) and a $LaBr_3(Ce)$ crystal with 12.9 cm^3 volume exhibits 5.1% and 3.2% resolution at 662 keV peak respectively. [81] It becomes even worse for CZT (18.7 %) at 81 keV compared to the $LaBr_3(Ce)$ (9.1%) at same energy. [81] Thus, at sizes large enough to provide a useful sensitivity, the CZT likely would no longer have any advantage over $LaBr_3(Ce)$, particularly at the energies in this project. It is, of course, still one of the best options for spectroscopic purposes since it has the best energy resolution in miniature sizes. However, $LaBr_3(Ce)$ would be a good alternative to CZT since it has comparable performance characteristics and much less cost compared to the CZT.

NaI(TI) is another important crystal used for spectroscopic purposes. Better energy resolution can be obtained by $LaBr_3(Ce)$ and $LaCl_3(Ce)$ above approximately 120 keV as compared to the resolution obtained by NaI(TI) at same energy range. [82] Although, as the energy falls below 120 keV the percent energy resolution of the NaI(TI) gets closer to the percent energy resolution of $LaBr_3(Ce)$ and $LaCl_3(Ce)$, they still provide slightly better results than NaI(TI) in terms of percent energy resolution under 120 keV which make them an excellent alternative to NaI(TI). [82]

The energy response of $LaBr_3(Ce)$ with respect to NaI(TI) and CZT within 0-662 keV is more linear. [82] High detection efficiency can be acquired by $LaBr_3(Ce)$ crystals thanks to their high density and recently available larger crystal sizes. For these reasons, $LaBr_3(Ce)$ can be considered as an excellent alternative for NaI(TI) and a possible replacement for CZT in

spectroscopic applications where moderate-high energy resolution and high detection efficiency is required. [82]

$LaBr_3(Ce)$, $LaCl_3(Ce)$, $CeBr_3(Ce)$ and $SrI_2(Eu)$ are all inorganic scintillators. As seen on Table 4.1, $LaBr_3(Ce)$ demonstrates better performance characteristics than both $LaCl_3(Ce)$ and $CeBr_3(Ce)$ with regard to energy resolution, light yield and decay time. $SrI_2(Eu)$, on the other hand, has better energy resolution below 662 keV and higher light yield as compared to $LaBr_3(Ce)$. $LaBr_3(Ce)$, and $SrI_2(Eu)$ show comparable energy resolution characteristic above 662 keV. [112] However, the decay time of the $SrI_2(Eu)$ is almost 20 times slower than the decay time of $LaBr_3(Ce)$. Therefore, $SrI_2(Eu)$ is only suitable for the applications that requires low count rates. [113] A potential pulse-pile up would occur on the spectrum of measured data, if they are used in detection of radiation sources with high count rates.

$LaBr_3(Ce)$ is an inorganic scintillator with very attractive properties when using in medical imaging for gamma spectrometry. Several studies have shown that it provides excellent energy resolution, very fast decay, high temperature stability, high gamma detection efficiency and excellent energy linearity. [114, 115] In a comparative study, the gamma spectrum of ^{57}Co was acquired using both $LaBr_3(Ce)$ and NaI(TI) with comparable volumes. The results showed that the 122-keV line was clearly distinguished from the 136-keV line if the $LaBr_3(Ce)$ was the detector in use. However, NaI(TI) was incapable of resolving these two energies. [116] Another study

Table 4.1 Some Physical and Performance Charecteristics of Several Detection Crystals. Several papers has been cited including [76, 77, 79, 80, 81, 82, 113, 112, 114, 145] [191, 174, 192, 193, 195, 196, 175, 197, 176] [177, 178, 179, 180, 181, 182, 183, 118, 184] however the majority of the data taken from Eijk et al. [137]

	Density (g/cm^3)	**Light Yield (photons/ MeV)**	**Decay Time (ns)**	**Hygro-scopicity**	**Wavelength of maximum emission (nm)**	**Energy Resolution % at 662 keV**	**Energy Resolution % at 81 keV**	**References**
NaI(TI)	3.67	41,000	230	Yes	230	5.6	9.9	[76, 77, 79, 81, 137]
LaBr3(Ce)	5.3	63,000	16	Yes	380	2.6	9.1	[81, 114]
LaCl3(Ce)	3.86	46,000	25	Yes	330	3,3	an	[197, 137]
CdZnTe(very small volume)	6.2	na	na	No	na	1.8	na	[82]
CdZnTe(comparable volume)	6.2	na	na	No	na	5.1	18.7	[81]
CeBr3(Ce)	5.07	45,000	17.2	Yes	370	5.8	11	[177, 118]
BGO	7.1	9,000	300	No	300	9	na	[79, 137, 145, 180]
LSO	7.4	26,000	40	No	40	7.9	na	[137, 181, 184, 190]
GSO	6.7	8,000	60	No	60	7.8	na	[146, 191, 137]
SrI2(Eu)	4.6	120,000	1200	Yes	435	3	na	[113, 112]
YaP	5.5	21,000	30	No	30	4.3	na	[137]
LuAP	8.3	12,000	18	No	18	15	na	[137, 183, 174]
LPS	6.2	30,000	30	No	30	10	na	[174, 137]
CsI(Na)	4.51	40,000	630	Yes	420	7.4	na	[78, 79, 137]
CsI(TI)	4.51	66,000	800	Slightly	550	6.6	na	[77, 79, 80]
CaW04	6.1	20,000	na	No	420	Integrating mode	na	[78, 79, 137]
YTa04(Nb)	7.5	40,000	na	No	410	Integrating mode	na	[175, 137, 182]
Gd202S(Tb)	7.3	60,000	1.0E+06	No	545	Integrating mode	na	[194, 137, 182]
Gd202S(Pr,Ce, F))	7.3	35,000	4.0E+03	No	510	Integrating mode	na	[192, 193, 137, 179]
Y1.34Gd0.6003(Eu,Pr)	5.9	42,000	1.0E+06	No	610	Integrating mode	na	[137, 176]
Gd3Ga5012(Cr,Ce)	7.1	40,000	1.4E+05	No	730	Integrating mode	na	[137, 176]
CdWO4	7.9	20,000	5.0E+03	No	495	6.8	na	[137]
Lu203(Eu,Tb)	9.4	30,000	1.0E+06	No	611	Integrating mode	na	[174, 195, 196, 137]
CaHfO3(Ce)	7.5	10,000	40	No	390	Integrating mode	na	[137]
SrHfO3(Ce)	7.7	20,000	40	No	390	Integrating mode	na	[137, 178]
BaHf03(Ce)	8.4	10,000	25	No	400	Integrating mode	na	[137]

na: Not available, not applicable or missing information

demonstrated that the detector efficiency of the lanthanum bromide gets higher as the gamma ray energy decreases due to the domination of photoelectric effect at lower energies (below 122 keV). $LaBr_3$(Ce) crystal detected 122-keV gamma lines 23.1% better than NaI(TI) at 15-cm source to detector distance. [114]

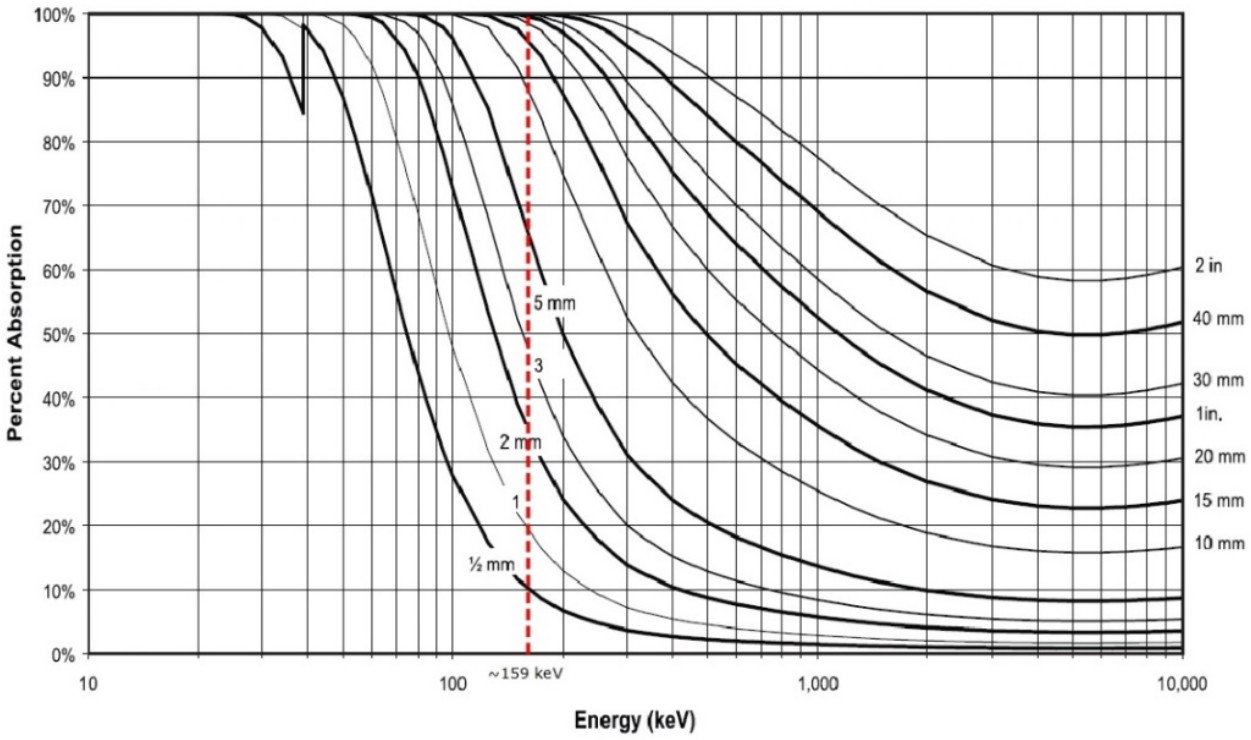

Figure 4.2 Intrinsic absorption efficiency of a 1-inch diameter LaBr3(Ce) crystal for different energies and different crystal thicknesses. Extracted from (Extracted from Brillance®380 Scintillation Material 2009 with permission) [117]

Figure 4.2 shows the absorption efficiency of a 1-inch diameter $LaBr_3$(Ce) crystal for different energies and different crystal thicknesses. As we are mainly dealing with energies below 159 keV, it shows almost 100% absorption efficiency thicknesses greater than 2.5 cm. [117] These two important characteristics of the $LaBr_3$(Ce), energy resolution and sensitivity, along with the others characteristics discussed above, make it an ideal tool for this project since we want to resolve 141 keV (^{99m}Tc) energy from 159 keV (^{123}I) energy with high detection efficiency.

The only known drawback of $LaBr_3$(Ce) crystal is the existence of internal background (self-activity) coming from ^{138}La, which is a naturally occurring radioisotope of La with 0.09% abundance. The energy spectrum of $LaBr_3$(Ce) measured by a HPGe detector is shown in Figure 4.3. The decay of ^{138}La results in three intrinsically produced photon peaks: 789 keV gamma line from a beta decay with 33.6% branching ratio, 1436 keV gamma from electron capture with 66% branching ratio and a 32-keV fluorescence x-ray peak. A 1461 keV peak coming from ^{40}K is also acquired. [82] Due to the existence of ^{138}La in $LaBr_3$(Ce), an average of 1.45-1.49 counts $s^{-1}cm^{-3}$ self-activity was detected in the crystal. [118] However, taking this low average background count rate into account and being aware of the gamma lines on the spectrum due to the internal activity, the use of $LaBr_3$(Ce) in our task should not create a problem.

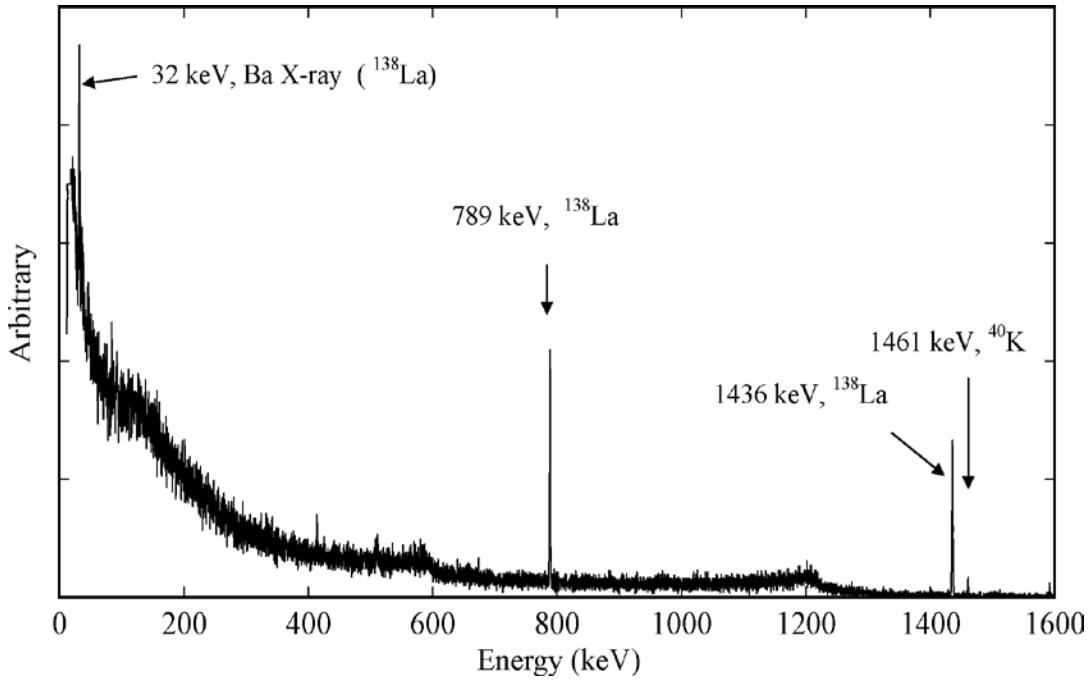

Figure 4.3 Intrinsic/Internal Energy Spectrum of $LaBr_3$(Ce) measured by an HPGe detector. Reproduced from Alexiew et al. [119] with permission.

4.2.3. Determination of the Required Thickness

When gamma rays and x-rays interact with matter, some portion of the energy is absorbed by the matter through photoelectric effect, Compton scattering and pair production interactions. However, the rest passes through without being absorbed by the material. Both the number of absorbed and number of transmitted photons depend on the material that the radiation passes through, its thickness and incoming photon energy. The probability of monoenergetic gamma rays

and x rays undergoing photoelectric or Compton interactions in matter generally follows an generally exponential relationship with the thickness of the matter. Assuming a number of photons N_0 of energies under 200 keV (where there will be no pair production), incident onto a slab of material, the resulting number of photons $N(x)$ after these gamma or x rays pass through the material with a thickness x can be determined from Equation 4.1 and the process is graphically represented in Figure 4.4. :

$$N_{(x)} = N_0 \, e^{-(\tau_I * x + \sigma_I * x)} \, . \tag{4.1}$$

where τ_I and σ_I are components of the linear attenuation coefficient due to the photoelectric effect and Compton scattering, respectively. The summation of these two components $(\tau_I + \sigma_I)$ is commonly expressed as linear attenuation coefficient "μ_I" which simplifies Equation 4.1 to Equation 4.2. :

$$N_{(x)} = N_0 \, e^{-(\mu_I * x)} \, . \tag{4.2}$$

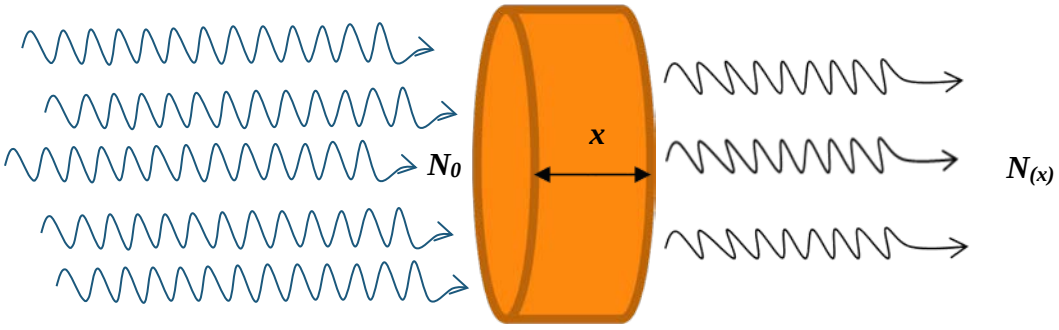

Figure 4.4 A graphical expression of x-rays or gamma rays pass through a material with a thickness "*x*".

The percent of photons attenuated by the material can then be determined from Equation 4.3 in which $N_{(x)}$ is the number of photons transmitted, $N_0 - N_{(x)}$ is the number of photons attenuated by the material. :

$$Attenuation[\%] = \frac{N_0 - N_{(x)}}{N_0} * 100 = \frac{N_0\left(1 - e^{-(\mu_I * x)}\right)}{N_0} = \left(1 - e^{-(\mu_I * x)}\right). \qquad (4.3)$$

*T*he absorption efficiency of a detection crystal follows a similar analysis but looking at the energery converted into electrons and absorbed in the crystal In this case the attenuation

coeffiecient used in equations 4.1-4.3 would be replaced with the mass energy attenuation coefficient, giving :

$$E_e = E_\gamma(1 - e^{-\mu_{en}\rho x}). \quad (4.4)$$

Where E_e is the energy given to the electrons, E_γ is the energy of the photons incident on the crystal, μ_{en} is the mass energeny attenuation coeffient, ρ is the density and x, as before, is the thickness of the crystal. The percent absorption efficeincy becomes, :

$$Absorption\ [\%] = \frac{E_\gamma(1-e^{-\mu_{en}\rho x})}{E_\gamma} = (1 - e^{-\mu_{en}\rho x}). \quad (4.5)$$

which depends on the thickness and effective atomic number of the material and energy of the incoming photons. The equations used assume a monoenergetic beam of photons. For a mixed-energy beam, the total quantities would have to be summed for each componant of the beam, or, if the beam has a continuous spectrum, the quantities would be integrated over the spectrum.

In this case, the minimum thickness of crystal needed can be determined by the interpretation of Figure 4.2. Based on the Figure 4.2, which is provided by the manufacturer, the

minimum thickness of $LaBr_3$(Ce) crystal required to obtain 100% absorption efficiency at 159 keV energy intrinsically is around **25 mm**. [117]

4.2.4. Determination of the Minimum Diameter Needed

Diameter of a cylinder-shaped detection crystal is the other factor affecting the intrinsic efficiency of that crystal. In this work, two cases were investigated in order to find the minimum diameter required: Assessing a photoelectric interaction takes place in the crystal and the resulting photoelectron moves approximately perpendicular to the cylindrical axis, as seen in Figure 4.5, and a Monte Carlo simulations performed in order to determine the intrinsic photopeak efficiency of the crystal for different diameter size of the crystal at thickness of 25 mm.

i. Electron Range

For the first case, the minimum diameter needed can be expressed as the maximum distance travelled by the electron in the crystal. The maximum distance *x* travelled by photoelectron in the crystal can be calculated either by empirical formulas as stated in Equation 2.6 at page **Error! Bookmark not defined.** or from Continuously Slowing Down Approximation (CSDA).

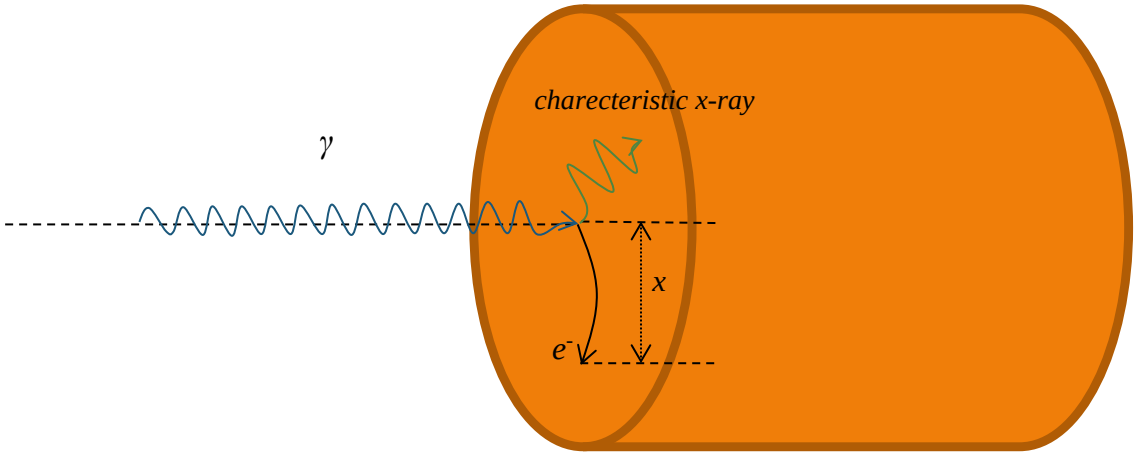

Figure 4.5 Graphical expression of incoming photon interacts with the crystal through photoelectric interaction just on the surface, resultant photoelectron travels distance x in the direction of perpendicular to the cylindrical axis. Eventually, the photoelectron is absorbed by the crystal.

The 159 keV photon emitted from ^{123}I interacts with one of the tightly bound valance electrons of the $LaBr_3$. A photoelectron with energy of E_e is then emitted. E_e can be calculated from Equation 2.1 in page **Error! Bookmark not defined.**. The K shell atomic binding energies (E_b) of La and Br are found to be 39 keV and 13.5 keV respectively. [120] The calculations can be performed for two cases: when Lanthanum is the dominant element during the interaction and when the Bromine is. By inserting these values in Equation 2.1, the resultant photoelectron energies are calculated as 120 keV and 145.5 keV for Lanthanum and Bromine dominant

interactions, respectively. However, rather than separating the elements from the compounds, the effective atomic number and mean excitation energy of the compound can be calculated, and based on these, the CSDA ranges of the electron as a function of energy can be plotted. The calculation of the CSDA range of electrons in $LaBr_3(Ce)$ used the NIST website. By entering the relative weights of the Lanthanum (La), Bromine (Br) and Cerium(Ce) in the compound and using the density of the $LaBr_3(Ce)$ as (5.08) g/cm^3, NIST ESTAR software calculated the mean excitation energy of the $LaBr_3(Ce)$ as 458.1 ev. [121] Based on that, the software plotted and tabulated CSDA ranges as a function of energy as seen on Figure 4.6 and Table 4.2.

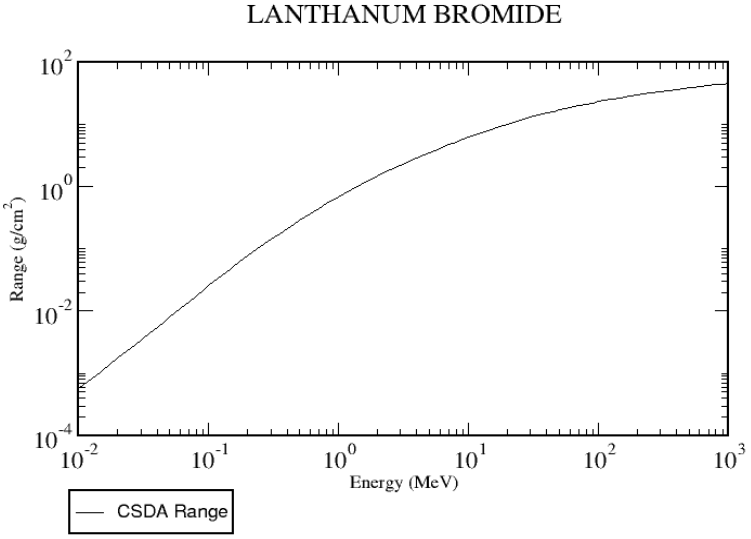

Figure 4.6 Plotting of the CSDA range of the electron in $LaBr_3(Ce)$ as a function of energy. Plotted in [121].

Table 4.2 Data extracted from Figure 4.6.

Kinetic Energy (keV)	CSDA Range (g/cm^2)
10	5.62E-04
13	8.05E-04
15	1.08E-03
18	1.39E-03
20	1.74E-03
25	2.52E-03
30	3.41E-03
35	4.42E-03
40	5.53E-03
45	6.74E-03
50	8.04E-03
55	9.43E-03
60	1.09E-02
70	1.41E-02
80	1.76E-02
90	2.14E-02
100	2.54E-02
125	3.65E-02
150	4.89E-02

By linear interpolation of Table 4.2, the CSDA range of electrons in $LaBr_3$(Ce) are calculated as 0.0341 and 0.0465 g/cm^2 for 120 keV and 145.5 keV respectively. By dividing these values by 5.08 g/cm^3, the density of the crystal, the maximum distance travelled by photoelectron in $LaBr_3$ was found to be 0.067 mm and 0.092 mm for La and Br dominated interactions, respectively.

If the incoming photon is from a ^{99m}Tc source instead, which has a 141 keV energy, by using Equation 2.1 in page **Error! Bookmark not defined.** again, the energies of the photoelectron is found to be 101.5 keV and 127 keV, when the incoming photon interacts with a k-shell electron of the La and Br, respectively. The calculation procedure above is repeated and range of the photoelectron with 101.5 keV and 127 keV is calculated as 0.051 and 0.074 mm respectively.

As will be seen below, in no case is the electron range a determining factor in the crystal geometry.

ii. Intrinsic Photopeak Efficiency

Intrinsic photopeak efficiency of detection crystal is another important factor that affects the overall sensitivity of a detection system. Percent intrinsic-photopeak efficiency of a detection crystal can be calculated from Equation 4.6.:

$$\varepsilon\,[\%] = \frac{E_p}{E_i} \times 100\ \%. \qquad (4.6)$$

where; E_i is the energy carried by the particles incident on the front circular surface of the detection crystal, E_p is the energy in the of photopeak deposited in the crystal volume.

Monte Carlo simulations were performed in order to calculate the intrinsic photopeak efficiency of the crystal for different diameters of the crystal. Figure 4.7 shows the model geometry used in the simulations.

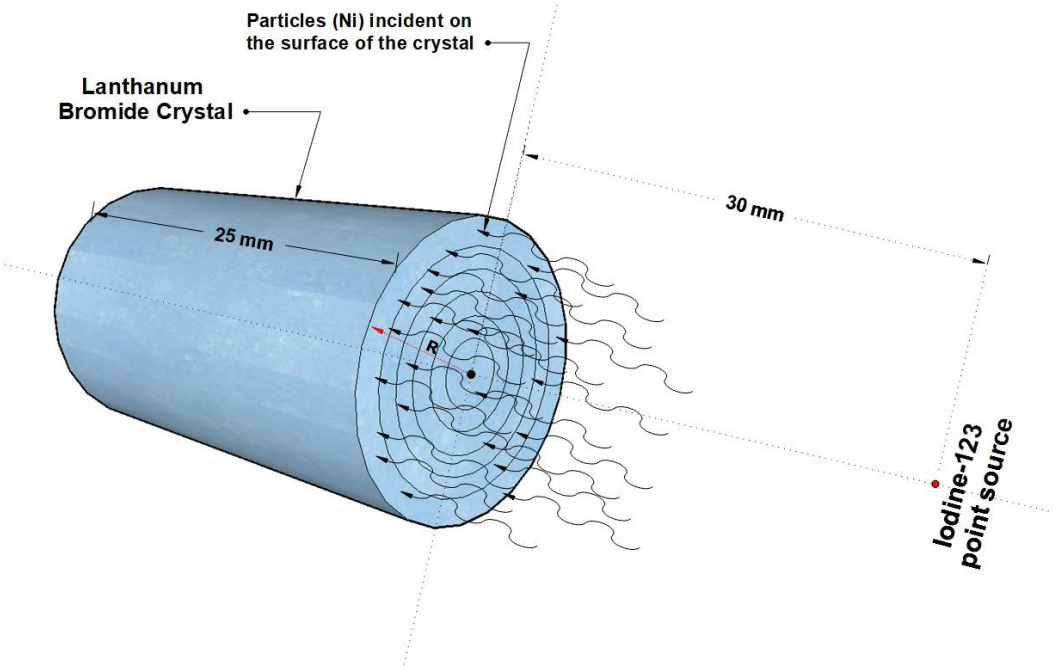

Figure 4.7 The model used in MCNP simulations to determine the intrinsic efficiency of the detector.

As seen in Figure 4.7, an isotropic ^{123}I point source has been used at a source-to-crystal surface distance of 30 mm. The crystal set to have a thickness of 25 mm. The geometry in Figure 4.7 was modeled in MCNP code and intrinsic percent photopeak efficiency of the detection crystal in Equation 4.4 has been calculated as a function of radius of the crystal. The results were then plotted as seen in Figure 4.8.

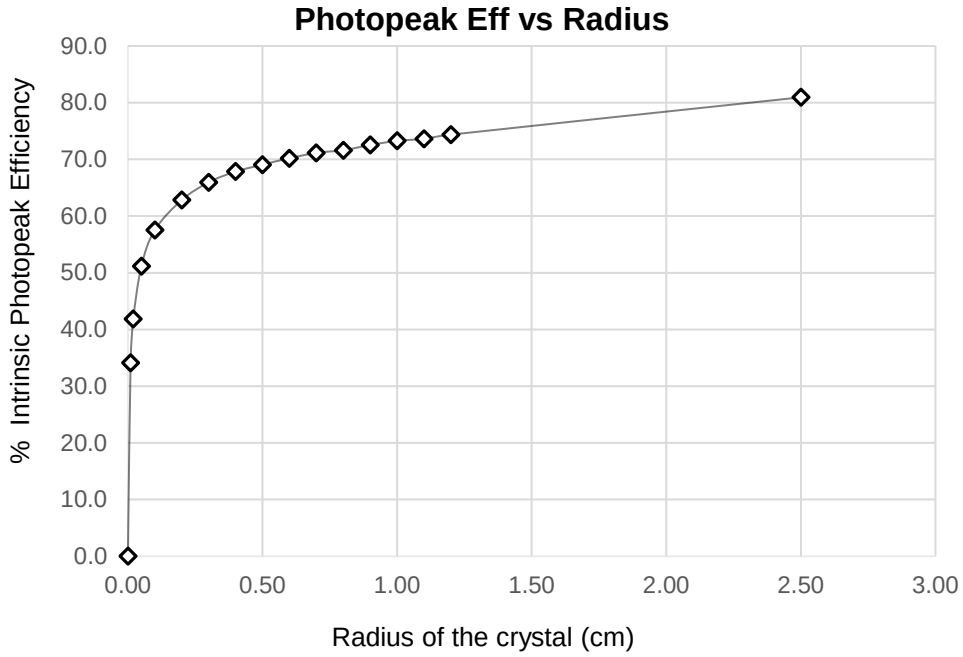

Figure 4.8 Plot shows the results of the MCNP simulations which provided percent intrinsic photopeak efficiency of the crystal as a function of the radius of the crystal.

As seen in Figure 4.8, there is a fast increase in intrinsic photopeak efficiency of the crystal for crystal radius between 0-0.5 cm. After about 0.5 cm radius, the slope decreases. Therefore, the difference in percent intrinsic photopeak efficiency of the crystal with a radius of 0.5 cm and 2.5 cm is seen as only about 14.0 percent based on the plot in Figure 4.8. Considering the higher cost

of the crystal for larger sizes and size limit based on the task of the project, fourteen percent difference is highly tolerable. Hence, the radius of the crystal is selected to be 5 mm.

4.3. Determination of the Photon-Multiplication Component

Radiation can be measured either directly with semiconductors or indirectly with scintillators. When radiation incident on a semiconductor, in which negative and positive charges are uniformly distributed, negative and positive charges are separated from each other through ionization. [41] Thus, while negative charges travel towards anode side, positive charges travel towards cathode, resulting in an electrical pulse which can be measured directly. Semiconductors, therefore, do not require a photon multiplication device for photon counting. [41] However, scintillators require a photon amplification device in order to measure the radiation. These devices can be divided in two category as explained following subsections.

4.3.1. Measurement with Conventional Photo-Multipliers (PMT)

When radiation interacts with the scintillation material, free electrons and photons are emitted as the result. The resultant electrons interact within the material by transferring most of their energy to the material and that is emitted again in the form of characteristic light. [122] The

photocathode of a conventional photo-multiplier tube (PMT) converts the energy of the light photon to an electron through the photoelectric effect. An iterative process takes place in dynodes, where the strong electric fields between successive dynodes accelerate the photoelectron to the next dynode, and multiple secondary electrons are knocked out of the dynode during the impact. These electrons hit the next dynode, generating more electrons. [122] This process continues until the electrons hit the last dynode (anode) resulting in a measurable electric pulse. The average time of the amplification in a PMT is ~50 ns and typical multiplication factor ranges between ~10^5-10^7. [122]

4.3.2. Measurement with Silicon Photo-Multipliers (SiPM)

A silicon photomultiplier (SiPM) is the other light sensing device that can be used to measure resultant photons emitted from scintillators. It is simply a multi-pixeled photon counter array working in a solid-state fashion detecting individual photons. Each pixel in a SiPM so-called micro-cells, works as an individual Geiger Mueller Avalanche Photo-diode (GM-APD), connected parallel to each other, all together constituting a single SiPM cell, as seen in Figure 4.9 (a) [123]

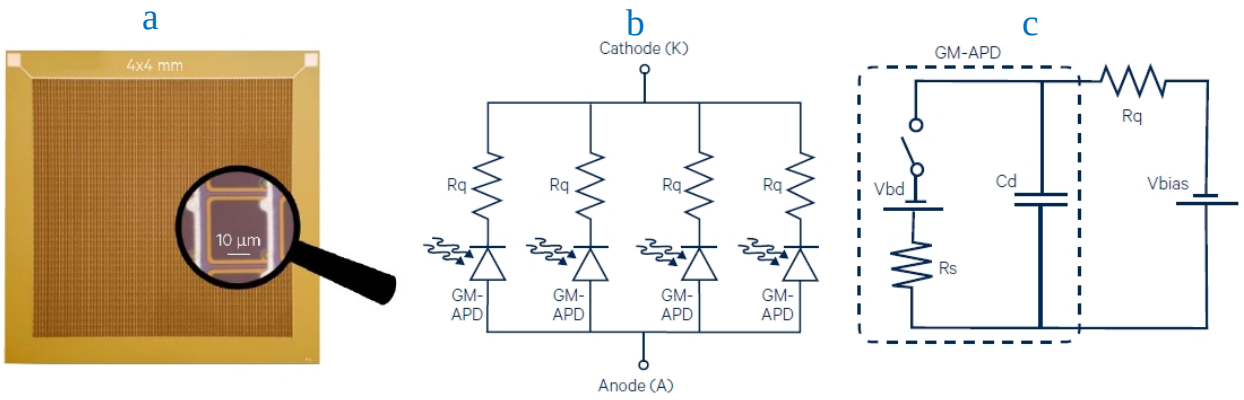

Figure 4.9 (a) A single SiPM cell consisting of a matrix of microcells connected parallel to each other. (b) Circuit showing the parallel connection of each micro-cells to each other through series of resistors. (c) Individual equivalent circuit of a micro-cell with series bias voltage and resistor. (Copied from [123] with permission)

In Figure 4.9 (c), an equivalent circuit of the microcells (APDs) is shown in which "C_d" is the diode capacitance in reverse bias, R_s is the silicon substrate series resistance, R_q is the quenching resistor. Three different mode can be observed in a GM-APD operation: Quiescent mode, discharge phase mode and recovery phase mode. Quiescent mode is when the diode is biased to the bias voltage (V_{bs}) reversely and the switch in In Figure 4.9 (c) is open. Once a photon is observed or a dark event takes place, the switch gets closed and the APD enters discharge phase. In discharge phase, the diode capacitance discharges passing through R_q and creates avalanche multiplication inside the microcell. During avalanche process, a steady current flows in the APD

unless it is quenched by R_q. Quenching this avalanche process results in an open switch again in which the APD enters in recovery phase. The charging process of the bias voltage by diode capacitance is repeated through R_q and quiescent mode is activated again, and the APS is ready for the absorption of a new photon.

A reverse bias voltage V_{bs}, which is only a few volts above breakdown voltage V_{br} of a microcell, is applied to the SiPM cell. The magnitude of overvoltage (ΔV), which is the voltage difference between V_{bs} and V_{br}, varies between 30-70V, depending on the design. [124]

A microcell or an individual APD works based on a p-p-n junction-structured photodetector. A silicon p-n junction of a photodiode creates a depletion region, which is the region that does not contain any mobile charge carriers. A photon energy absorbed in the silicon is transferred to the bound electron and moves it from the valence band to conduction band, creating electron-hole pairs. [124] Intrinsic electric field, which is created by intrinsic photoelectric interaction as the result of photon absorption, will cause the electrons to be dragged into the n side, and holes to p-side of the photodiode. The combination of intrinsic electric field of the junction, which is created by intrinsic photoelectric interactions, and the applied reverse bias V_{bs}, creates a strong electric field in the depletion region, or avalanche region, as seen on Figure 4.10. [124]

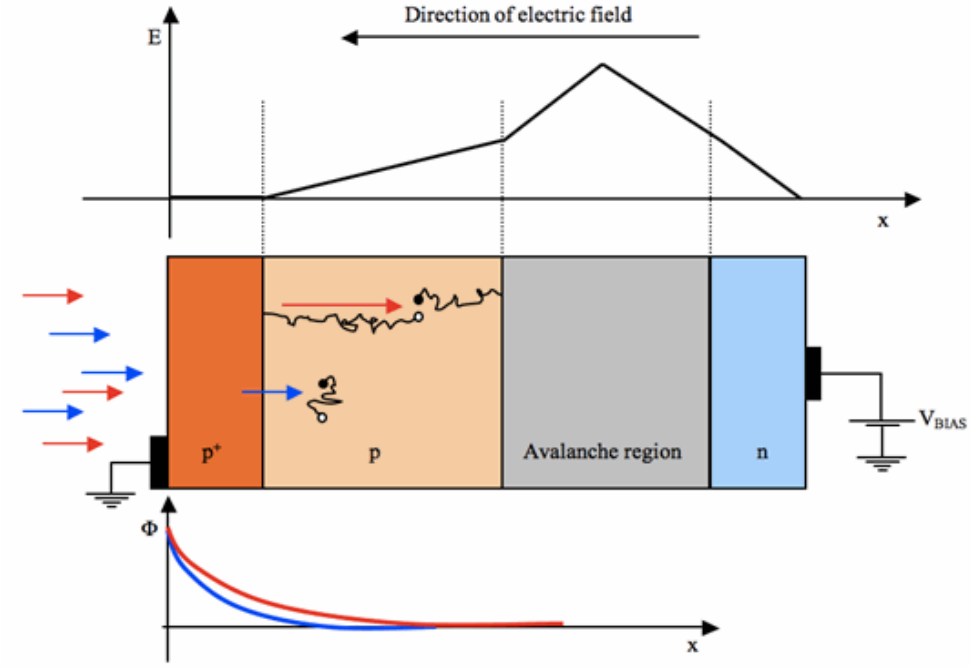

Figure 4.10 Schematic shows p-p-n junction structure and working principle of an APD/microcell in a SiPM. (Copied from [124] with permission)

When a sufficiently high electric field is created in the depletion region, charge carriers will be accelerated to a point where they carry sufficient kinetic energy to create secondary charged particles, called impact ionizations. Then, the silicon breaks down and the original electron hole pair is converted to a net current flow in the device. This process is called Geiger discharge. [124] Then, light is detected. However, the problem with individual microcells/APDs is when more than one photon arrives at the surface of an APD at the same time, the APD can only detect one of

them. [117] Thus, SiPMs contain a matrix of microcells/APDs connected parallel to each other, will allow simultaneous multi-photon detection.

4.3.3. Advantages of SiPMs over Conventional PMTs

SiPMs have been utilized in medical imaging for over a decade to eliminate some drawbacks originating from the use of a conventional photomultipliers (PMT). The well-known limitations of PMTs are: relatively high cost, bulky size, sensitivity to magnetic fields and low quantum efficiency. Some of the important advantages of SiPMs are relatively much smaller size, low-cost, low voltage bias compatibility, and low-noise level vs. supplied regulated voltage. [111, 125]

A comparative study demonstrated that a SiPM coupled to scintillators showed comparable gamma-spectral performance when compared with a PMT coupled to same scintillator. [126] Scintillation crystals coupled with SiPMs provided considerably better energy resolution than a conventional PMT coupled to same crystals for low energy range gamma detection (<200 keV). [126] SiPMs requires a bias voltage of only a few tens of volts e.g., 25.2V, which makes them suitable to be integrated with small internal-unit Li-ion batteries, instead of using external power suppliers that are used with conventional PMTs. [127] For handheld applications, this feature enables overcoming size and design complexities caused by external electronics of the conventional detector systems. Hence, the small size, better energy resolution in detection of low

energy gamma lines, low cost and other advantages of SiPM make it well-suited to the imaging applications that specifically require compactness, hand-held mobility, low magnetic sensitivity, multi-mode spectral energy selectivity and resolvability.

There are three major brands of SiPM technology: Hamamatsu, Ketek and SensL. In another comparative study, good linearity of response within a temperature range of -20 ^{o}C and +50 ^{o}C was recorded by SensL and Ketek brands SiPMs coupled to scintillators. [128] Overall, sensL's SiPM exhibited better performance than other two brands. [128]

As discussed earlier, photons emitted from scintillators impinge on the microcells of the SiPM and are counted as the result. The wavelength of the photons emitted from the scintillator is an important characteristic since detection efficiency of these photons by Silicon Photomultiplier are highly depend on their wavelength as seen on Figure 4.11. Brillance-$^{™}$380 is a $LaBr_3$(Ce) crystal, growth and procured by *Saint-Gobain Ceramics & Plastics, Inc* (Malvern, PA, USA). [117] Figure 4.11 (a) shows the range of the wavelength of the photons emitted from Brillance-$^{™}$380 crystal and their corresponding percent quantum efficiencies. It varies between 340-440 nm, having a maximum wavelength of emission at 380 nm. [117] Figure 4.11 (b) shows the photon detection efficiency of a SensL-MicroFJ 60035 silicon photomultiplier *(SensL-ON Semiconductors ISG, Cork, Ireland*) as a function of wavelength of the photons absorbed. [127]

.

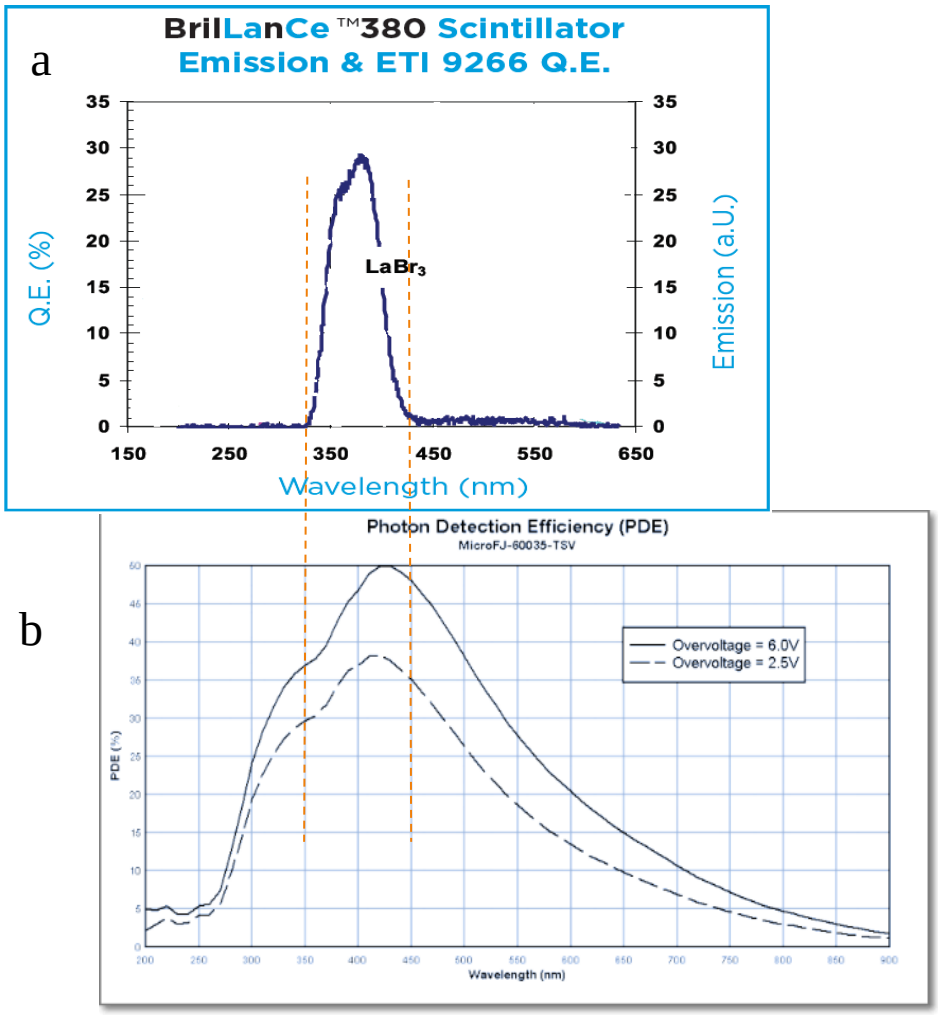

Figure 4.11 (a) plot of the photon detection efficiency of a SensL-MicroFJ 60035 silicon photomultiplier *(SensL-ON Semiconductors ISG, Cork, Ireland*) as a function of the wavelength of the photons absorbed. Taken from [127] (b) shows the range of the wavelength of the photons emitted from Brillance-™380 $LaBr_3$(Ce) crystal and their corresponding emission probabilities. (Copied from [117] with permission)

As it can be deduced from Figure 4.11 within the range of wavelength of the photons emitted from the $LaBr_3$(Ce) crystal, the silicon photomultiplier provides a wide range of high photon detection efficiency that includes about 60 % efficiency at a wavelength of 420 nm. This is another important factor demonstrating the compatibility of Silicon Photomultipliers with the LaBr3 (Ce) crystal

4.4. Selection Results of the Critical Components of the Detector Unit

As discussed in Sections 4.2 and 4.3 , based on the superior performance characteristics and compatibility of both Silicon Photo Multipliers and the LaBr3 (Ce) crystal, it was decided that this pair would be used as the two of the most important components of the detector in this project. As the results of the calculations explained in Section 4.2.3 and 4.2.4, our proposed detection crystal would be a 5% Cerium activated cylinder-shaped $LaBr_3$(Ce) having a diameter (Ø) of 10 mm and a thickness of 25 mm, hermetically sealed with a 2-mm thick (sides) reflector mounted in a 1.5 mm thick aluminum housing cylinder, as seen on Figure 4.12.

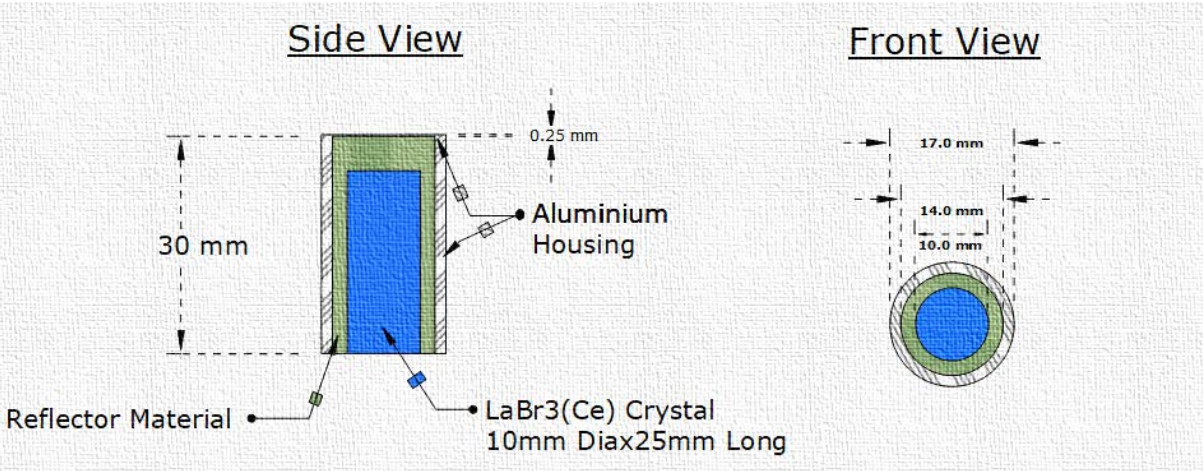

Figure 4.12 Schematic representation of the dimensions of the detection crystal $LaBr_3(Ce)$, reflector material and aluminum housing unit.

The brand, type and dimensions of the Silicon Photomultiplier has been chosen based on the diameter of the scintillator and discussion in Section 4.3. It is a SensL Micro Array FJ60035-4P which is comprised of 4 individual 6mmJ-series SiPM cells in 2x2 array sequence mounted to a The ARRAYJ−60035−4P−PCB evaluation board, which gives access to the output of the Micro Array FJ60035-4P SiPM as seen on Figure 4.13. [129]

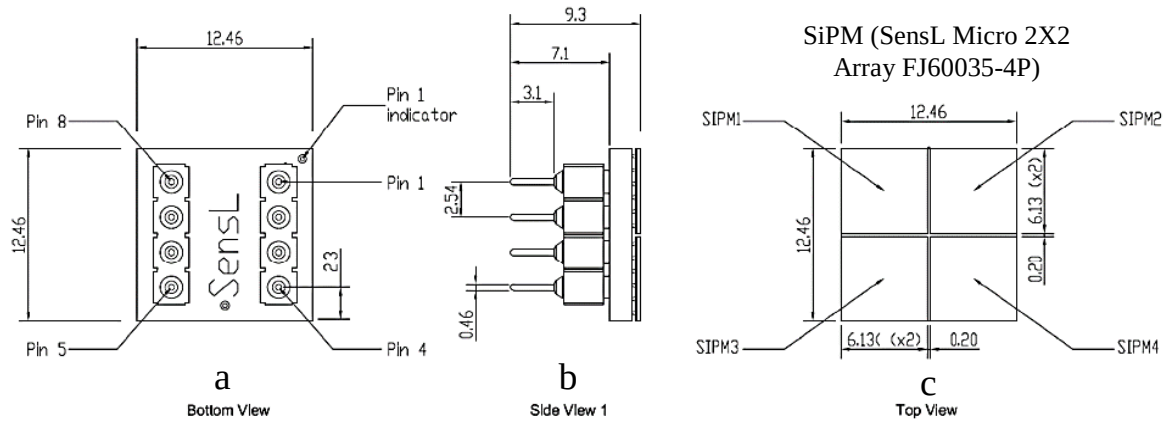

Figure 4.13 (a) Bottom schematic view of the SensL ARRAYJ−60035−4P−PCB evaluation board. (b) Schematic side view of the whole unit in which SensL Micro 2x2 Array FJ60035-4P SiPM mounted to SensL ARRAYJ−60035−4P−PCB evaluation board. (c) Schematic top view of the SensL Micro 2x2 Array FJ60035-4P SiPM. (Extracted from Manufacturer's Technical Report with permission.) [129]

Table 4.3 and Table 4.4 shows summary of the performance characteristics of Micro Array FJ60035-4P SensL SiPM and $LaBr_3$(Ce) crystal , respectively. All values on both tables extracted from manufacturer's technical reports.

Table 4.3 Tabulated Performance Charecteristics of the SensL Array J-60035-4P Silicon Photomultiplier. Values are taken from [127]

SensL Array J-60035-4P SiPM	
Parameter	**Value**
Type	Array
Active Area	12.46x12.46 mm^2
Array Size	2x2
Cell size	6x6 mm^2
Microcell Size	35μm
Total # of Microcells	22,292
Peak PDE Wavelength	420 nm
Minimum Bias Voltage	25.2 V
Maximum Bias Voltage	30.7 V
Spectral Range	200-900 nm

Table 4.4 Tabulated Performance Charecteristics of BrillanceCe™380 $LaBr_3$(Ce) Scintillator. Values taken from Manufacturer's Technical Data Report. [130]

BrillanceCe™380 $LaBr_3$(Ce) Scintillator	
Parameter	**Value**
Density	5.08 g/cm^3
Decay Time	16 ns
Wavelength of Maximum Emission (λm)	380 nm
Light Yield	63 (photon/keV)
HVL at 662 keV	1.8 cm
Refractive Index at λm	~1.9

4.5. Development Process of the Detector Unit

After the critical components of the detector were identified, a manufacturer was identified who could prepare the components and assemble the prototype detector. Although the company estimated the delivery date as 2 to 3 weeks from the order date, the first iteration of the detector unit received in early June 2017, 26 months late. While the shape and concept of the detector were specified with the company before, the unit as delivered was not suitable for mobile measurements. Moreover, the silicon photomultiplier was not coupled to the scintillator and the detector was simply a box containing the components. The unit was returned to the company with details on how the unit needed to be assembled. The second iteration of the detector was received in January 2018, and Figure 4.14 shows a picture of the 2nd iteration of the detector. The detector unit came with a built-in preamplifier and lithium-Ion battery, so no external power or NIM pre-amplifier unit were required. However, due to connection failures in the unit, it was returned again to the manufacturer for repair. Instead of just repairing the detector, the company opted to rebuild a third iteration by adding some new features to the original design of the detector. The upgraded detector was received after a long delay in December 2018.

The same problem as with the second iteration was encountered after the arrival of the third, but instead of sending the detector back, the detector was personally delivered to the factory and the researcher waited for the repair. To ensure that the detector would work in the

laboratory after being tested in the factory, the company loaned its MCA to be used during the experimental measurements. The methods and results related to this study can be seen in Chapters 5 and 6. The schematic details of the third iteration of the detector and planar reconstruction from a CT scan of the detector, in both grayscale and inverse grayscale, can be seen in Figure 4.15 and Figure 4.16, respectively.

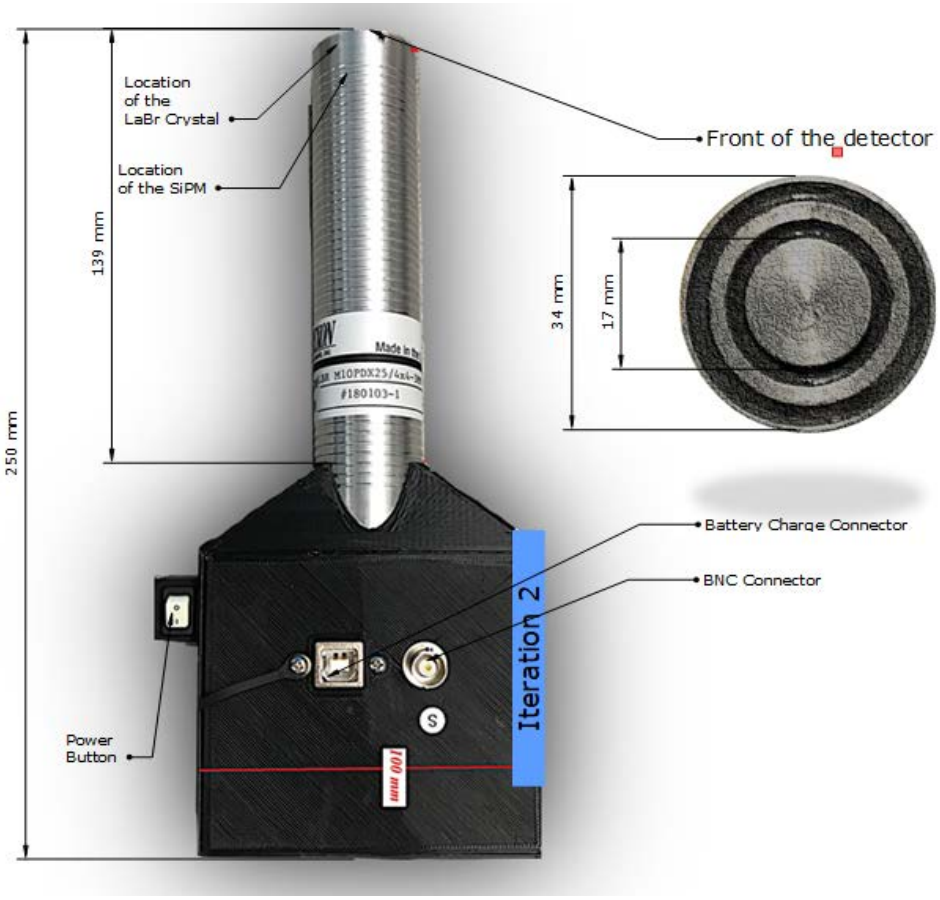

Figure 4.14 Graphical expression and dimensions of the 2nd iteration of the detector unit.

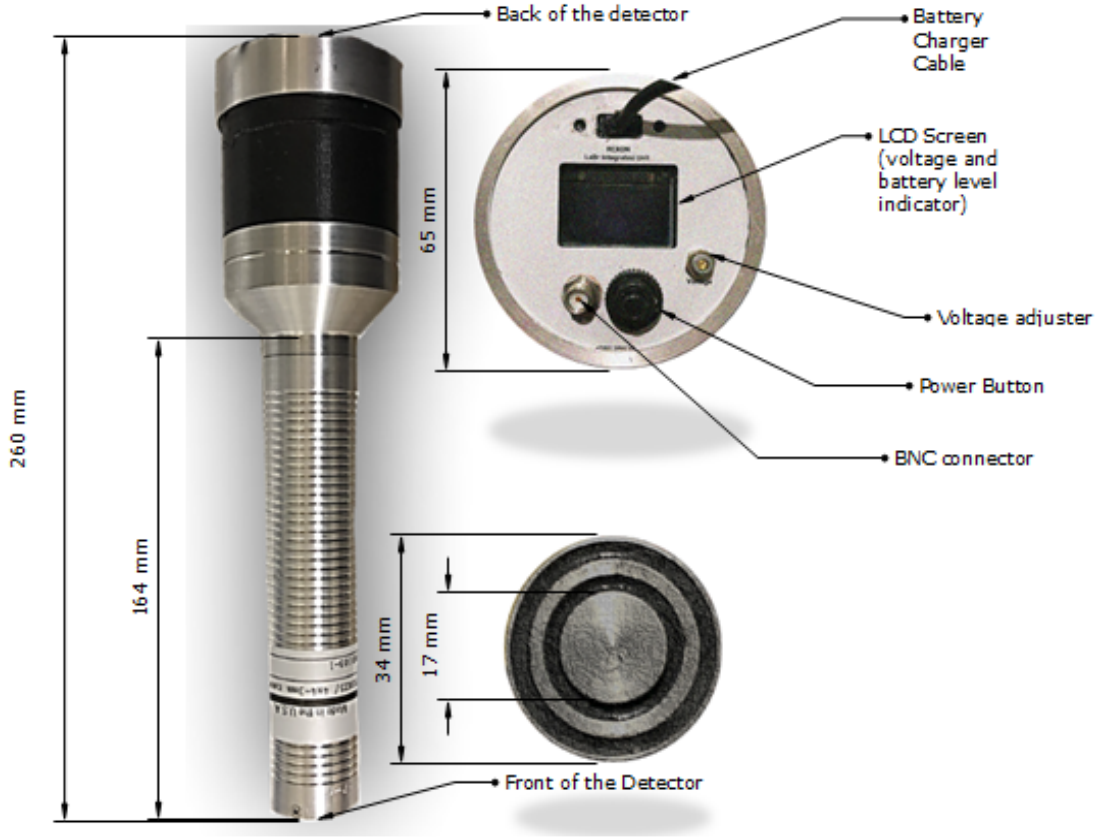

Figure 4.15 Dimensions and features of the 3rd iteration of the detector unit.

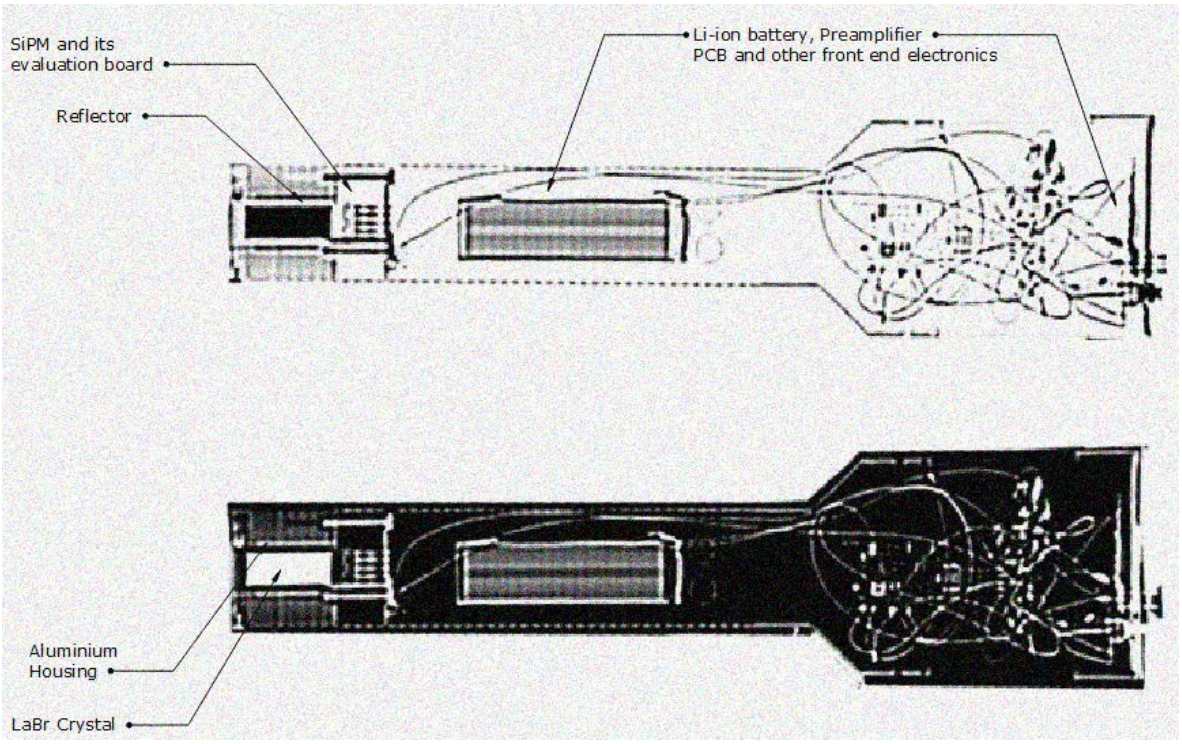

Figure 4.16 A planar reconstruction from a CT scan of the detector unit, in grayscale and inverse grayscale.

5. Characterization of the detector

5.1. Introduction

This work proposes to localize breast tumors using CLR1404 labeled with ^{123}I because of its short half-life and mono energetic gamma emission (159 keV with 0.833 emission probability). [106] The use of ^{123}I-CLR1404 radiotracer would allow imaging of the entire tumor, not just the center as with current methodologies. In addition, the project would still use ^{99m}Tc-labeled nanoparticles to localize the SNLs. One of the most commonly used medical imaging radionuclides, ^{99m}Tc decays to ^{99}Tc with a half-life of 6.007 h, emitting a 141 keV gamma with 0.89 branching ratio. [131]

Given that the proposed procedure uses ^{123}I and ^{99m}Tc, and the emission energies of these radionuclides are very close, differentiating and localizing the radiation from each source requires a probe with excellent energy resolution (spectral discrimination) and spatial resolution. It is also critical to reject counts due to the scattered photons. [58]

The detector must also have a sufficient photopeak efficiency to detect radiation lines coming from each source to locate at depth both tumor and lymph nodes containing activity. The experimental characterization of a prototype detector, including characteristics such as photopeak efficiency and energy resolution, is reported, along with Monte-Carlo validation of the results.

5.2. Materials and Methods

5.2.1. Experimental Procedure

i. Detector Components and Design

The detector unit is described in Chapter 4, and consists of a 10 mm diameter x 25 mm long $LaBr_3$ (5%-Ce) cylindrical scintillation crystal sealed in a 4.75 mm diameter (top) x 2 mm long (side) thick reflector of polytetrafluoroethylene, all of which was hermetically sealed in a 0.25 mm diameter (top) x 0.25 mm long (side) thick aluminum housing (Rexon Components and TLD System Inc. Cleveland, Ohio). The bottom of the housing was coupled to a 12.46 mm x 12.46 mm silicon photomultiplier (SiPM – SensL ARRAYJ-60035-4P, ON Semiconductors ISG organization, Intelligent Sensing Group, Cork, Ireland) The SiPM microarray has total of 4 6.33x6.33 mm^2 photo-sensing cells in a 2x2 array, each formed of 5,573 microcells, for an of total of 22,292 microcells. Each microcell serves as an avalanche photodiode coupled to a common anode and common cathode.

In Figure 5.1, the components of the detector unit, the geometry and dimensions of some critical components, and some important features are shown. Figure 5.1 also includes a planar reconstruction from a CT scan of the detector in an inverse-gray scale, similar to Figure 4.14. After setting the operating voltage to 29.3 V (noted as the optimal operating voltage value of SiPM by the manufacturer), the detector was connected to the amplifier input of an APTEC 5000S Multi-Channel Analyzer (MCA) that was connected to PC running APTEC (OCIC) multi-channel pulse height analyzing software. The schematic drawing of the instrumental setup of the experiments is shown in Figure 5.2.

ii. Radioisotopes Used in the Experiments and Simulations

The detector described above is designed to simultaneously visualize the radioactive distributions of radioisotopes injected into cancerous regions with similar energies below 200 keV, and thus, ^{109}Cd, ^{57}Co, ^{99m}Tc, and ^{123}I sources were utilized in the experiments. In addition, a multi-nuclide and a ^{137}Cs source were used to analyze the response of the detector to photon energies above 200 keV. The source calibration data for these sources is provided in Table A.1 in Appendix A. The ^{99m}Tc and ^{123}I sources were provided by the University of Wisconsin Health Nuclear Medicine Department. The ^{109}Cd, ^{57}Co, ^{137}Cs, and multi-nuclide sources were all check sources from the University of Wisconsin-Madison Radiation Calibration Laboratory.

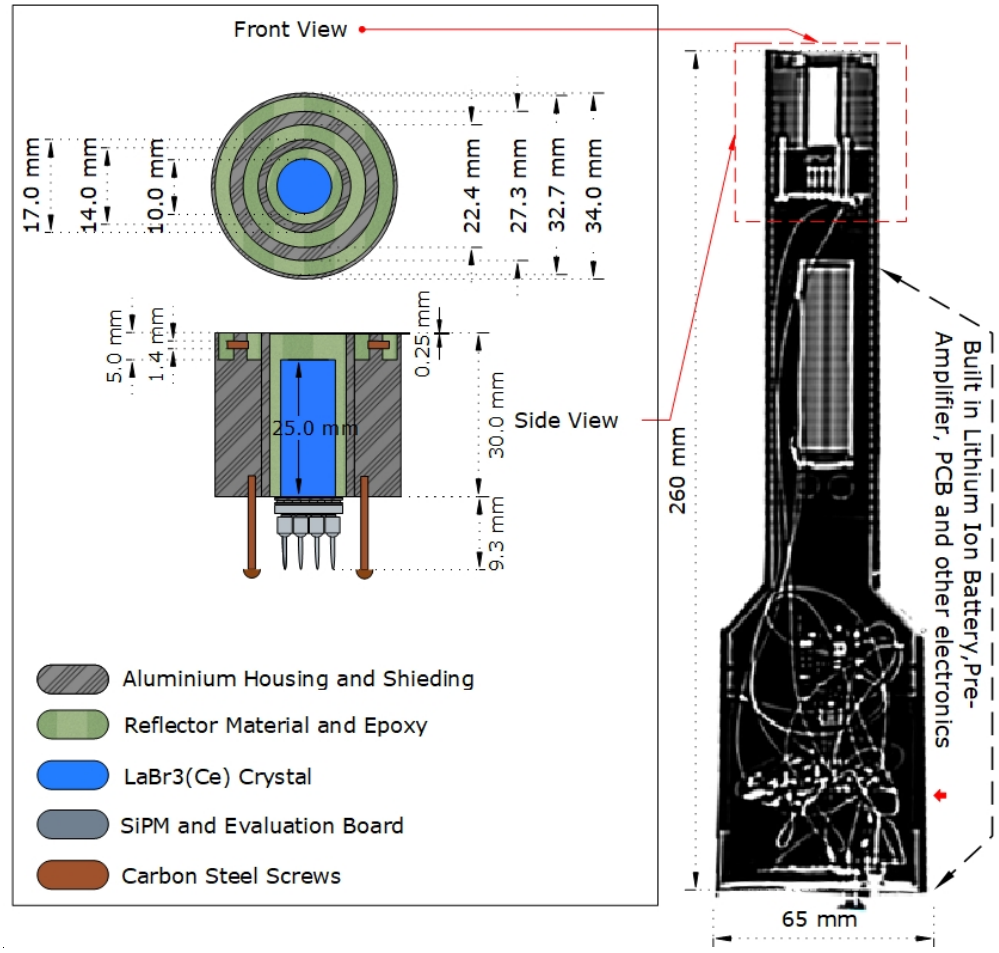

Figure 5.1 On the left, a graphical representation of the detector that shows the critical components, material composition, and associated dimensions. On the right, a two-dimensional reconstruction from a CT image of the detector shown in inverse grayscale.

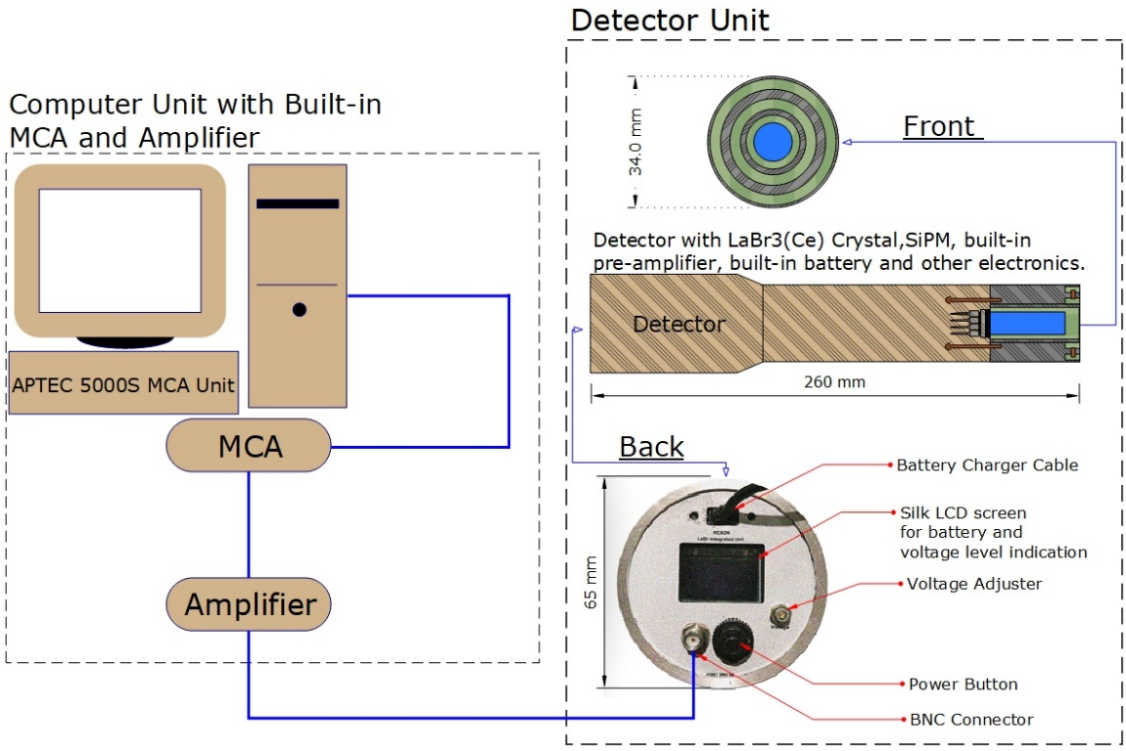

Figure 5.2 Schematic of the main instrumental setup used to measure efficiency, linearity, and resolution of the detector.

iii. Background Measurement and Subtraction

Before measuring any energy spectrum, the background radiation was measured. The instrumental setup for the background measurement can be seen in Figure 5.2 with no source in use. The time constant and fine gain of the amplifier was set to 1.0 μs and 2.5, respectively. The coarse gain was set to 2, raising the total gain in the amplifier to 5.0. The number of channels in the spectrum and ADC gain was both set to 1024. An energy spectrum has been acquired for 12,796 seconds to determine the counts due to the background. The background subtraction was applied to all spectra acquired experimentally.

iv. Spectrum Measurements

Each radiation source in Table 5.1 was placed on the axis of the detector one at a time at a specific source-to-center of the detector's front face distances for spectral measurements. The experimental parameters of the sources including source-to-detector surface distance (SSD), acquisition time and MCA settings are given in Table 5.1.

After acquiring the energy spectrum of the sources, peak analysis was performed for each source and the energy resolution of the photopeaks was determined using Equation (5.1):

$$FWHM[\%] = \frac{\Delta H}{H_\gamma} \times 100\%. \quad (5.1)$$

in which; ΔH is the channel width at half maximum, $H\gamma$ is the channel number of the photopeak. [132] The full width at half maximum of the photopeak can also be calculated in the unit of energy after calibrating the channel number by energy and performing the evaluation in energy units, as in Equation 5.2:

$$FWHM[keV] = \Delta H[keV]. \quad (5.2)$$

As shown in Table 5.1, the energy of the sources used in this study ranged between 0-1773 keV. The energy range for a particular source, such as ^{109}Cd fell between 0-88 keV. Therefore, some of the radionuclides required high gain, while others required low gain to fit optimally in the channels of the MCA. This did not allow the use of a fixed calibration curve for all sources.

Thus, the energy resolution of a photopeak was calculated using the channel number values that were best estimates for the particular radionuclide. The calculated energy resolution values are plotted as a function of energy in Section 5.3.2.

Table 5.1 Experimental and multi-channel Analyzer (MCA) settings data for each source used to acquire energy spectrum.

Experimental Settings			**MCA Settings**						
			Amplifier				**ADC**		
Nuclide	**SDD (cm)**	**Counting time (s)**	**Fine Gain**	**Coarse Gain**	**Total Gain**	**Time Const.**	**# of Channels**	**Gain**	**Lower Level Channel Discriminator**
^{109}Cd	1	200	4.5	2	9	1 µs	1024	1024	122
^{57}Co	5	200	4.5	2	9	1 µs	1024	1024	96
^{99m}Tc	100	120	3.5	2	7	1 µs	1024	2048	172
^{123}I	100	300	2.5	2	5	1 µs	1024	2048	172
^{123}I and ^{99m}Tc Together	100[a](Tc)-25[a] (I)	300	2.5	2	5	1 µs	1024	2048	172
^{137}Cs (Seed)	80[a], 40[b]	300	3.5	2	7	1 µs	1024	1024	86
Multinuclide	1[a], 6[b]	600	2.5	2	5	1 µs	1024	2024	81

[a] Source-to detector distance used for energy resolution measurements.

[b] Source-to-detector distance used to compare experimental spectra with MCNP simulations.

v. Photopeak Efficiency Measurements

The multi-radionuclide source and the sources of ^{109}Cd, ^{57}Co, ^{123}I were placed at 5 cm from detector surface as seen in Figure 5.3. The gamma spectrum of each source was acquired separately. The total number of counts under the photopeak for each energy was provided by the MCA software. The MCA software automatically sets a region of interest (ROI) around the photopeak and provided the total number of counts detected in this region. By using the channel window of this ROI, the number of background counts was calculated under the peak of interest and subsequently, the net number of counts were determined by subtracting background counts from the total counts for each source. The activity of each source was corrected for decay since calibration. Using Equation 5.3, the percent photopeak efficiency, ε, of each source was calculated and plotted as a function of photopeak energy. :

$$\varepsilon\,[\%] = \frac{N}{A_0 \times BR \times e^{-(ln2/t_{\frac{1}{2}})\times t} \times T} \times 100\%. \qquad (5.3)$$

where N is the number of net counts detected under the photopeak area, A_0 is the initial activity of the source [Bq], BR is the gamma emission probability of the source at photopeak energy, $t_{1/2}$ is the half-life of the source, t is the time since calibration and T is the experimental acquisition time (s). [133]

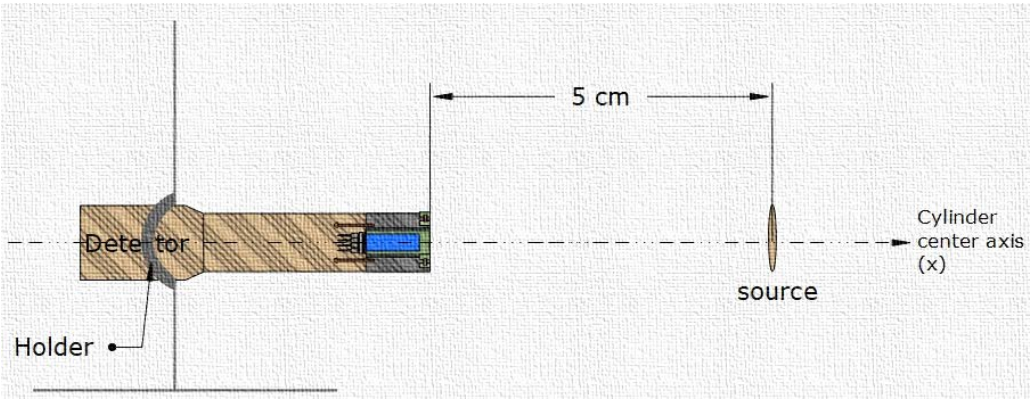

Figure 5.3 Schematic of the setup for photopeak efficiency measurements.

vi. Distance Measurements

Detector response as a function of distance was investigated by placing a ^{57}Co source on the axis of the detector at various SSD, as schematically shown in Figure 5.4. The region of interest was selected automatically by the MCA software. By using the channel window of this ROI, background counts were subtracted and the net count rate under the 122 keV peak area was computed for each distance.

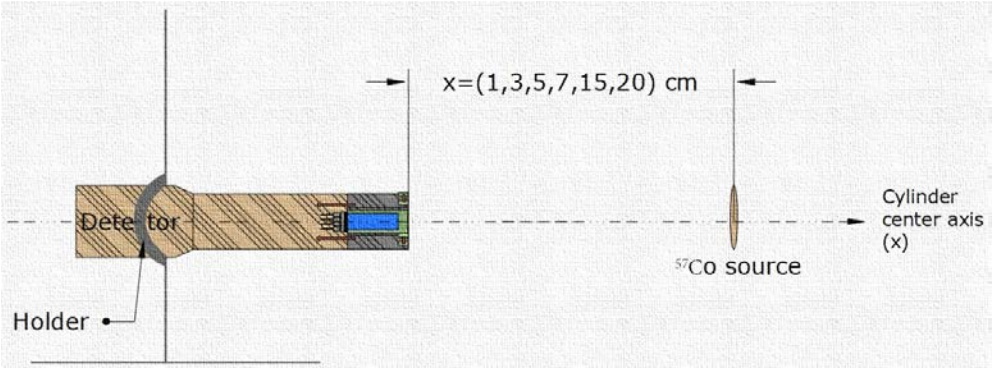

Figure 5.4 Schematic of the setup for distance response measurements.

5.2.2. Monte Carlo Simulations

In order to validate the energy spectra of the sources, the experimental results have been compared to computational spectra simulated with Monte Carlo MCNP6/MCNPX software (Triad National Security, LLC, manager, and operator of LANL, Los Alamos, NM). The Monte Carlo code allows the pulse height spectrum of the detectors to be simulated via the F8 tally feature. In order to use this feature and get accurate results, the detector had to be modeled for the program. The model used is shown in Figure 5.5.

i. Modeling of the Detector and Sources

The material composition and dimensions of the front portion of the detector are shown in Figure 5.1. Because of the critical importance of the detector geometry for the Monte Carlo simulations, a planar image of the detector was reconstructed from a CT scan (Figure 5.5 (a)). In order to model the geometry accurately, the acquired CT image was compared to the original design parameters and manufacturer's technical drawing and the 2D slice of the same portion of the detector was drawn using SketchUp Pro 2019 software [Trimble Inc. Sunnyvale, California], which can be seen in Figure Figure 5.5 (b). Finally, the geometry of this portion of the detector was modeled in the MCNP6/X software by defining surface, cell and data cards. The MCNPX Visual Editor Software with the Version of X_24E was then used to visualize the modeled detector as seen in Figure 5.5 (c).

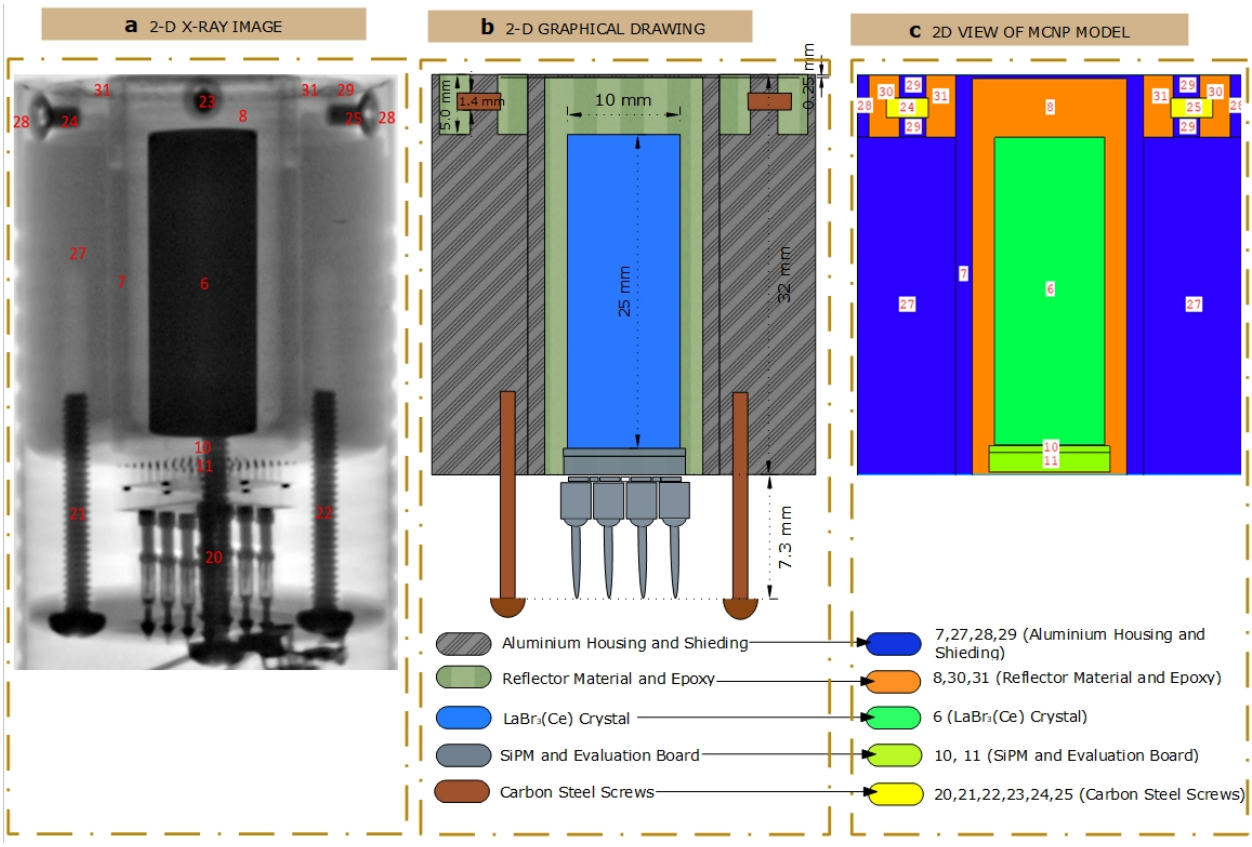

Figure 5.5 Modeling of the detector for the MCNP simulations: (a) the axial cross-section of the detector as shown in Figure 1; (b) the schematic drawing based on the CT image of the detector; (c) the MCNP input image of the detector

The MCNP6/X software allows defining a source within a Source, Distance, Energy Function (SDEF) card based on its position, mixed radionuclide constituents, emitted energies, and associated gamma emission probabilities. Table A-1 in Appendix A shows the specifications of the radiation sources used in Monte Carlo simulations. Three separate pulse-height simulations were performed to validate the experimental energy spectra of the sources. In the first simulation, a ^{137}Cs source was placed at a distance of 40 cm from the detector along the cylindrical axis. The second simulation included two different sources, ^{99m}Tc and ^{123}I,

placed at distances of 100 and 25 cm from the detector. In the last simulation, the multi-nuclide source was used with a 6 cm SSD.

The sources used to simulate the pulse-height spectra in MCNP were ^{137}Cs, the simultaneous use of ^{123}I and ^{99m}Tc sources, and the multi-nuclide source. The multi-nuclide source contained ^{210}Pb (0.047 MeV), ^{109}Cd (0.088 MeV), ^{137}Cs (0.662 MeV), and ^{60}Co (1.173 Mev and 1.333MeV). [134] All sources are assumed to be isotropic point sources since the active dimension of the sources was small enough and detector-to-source distances large enough to use the point source approximation. While ***Sin*** (source information) line within the SDEF card of MCNP code defines the energy of the source in units of MeV, the value in the ***SPn*** (source probabilities) line, on the other hand, defines the photon emission probability of this energy. *SPn* values are calculated from Equation 5.4 and tabulated in Table 5.2. The values are simply the normalization of the total gamma contribution of each radionuclide energy over the total number of photons emitted from all sources throughout the experiments. [135]

$$SPn = \frac{Activity\ of\ the\ Radionuclide\ (Bq) \times Branching\ Ratio}{Total\ \#\ of\ the\ photons\ emitted\ from\ the\ source\ per\ unit\ time\ (cps)} \qquad (5.4)$$

The position of a point source within the SDEF card is defined in *X*, *Y* and *Z* axes with the ***POS*** command in the form of "*POS x y z*". [135] The cylindrical axis of the simulated detector was

defined along the *Z*-axis with the front surface of the detector positioned at z=0. Radiation sources were positioned on this axis at specified *z* distances. Table 5.2 also provides the SDDs used in experiments and simulated in MCNP. Finally, the ***NPS*** (number of particles) block of the MCNP code defines the number of particles to be simulated.

Table 5.2 The source specifications and associated values used within MCNP simulations.

MCNP	Nuclide	Exp. Activity [Bq]	***SIn*** [MeV]	***BR***	***POS*** **[cm]**	***SPn***	***NPS***
Pulse Height Sim:1 ^{99m}Tc with ^{123}I	^{99m}Tc	2.0E+08	0.141	0.89	100	0.958	1.0E+09
	^{123}I	9.1E+06	0.159	0.833	25	0.042	
Pulse Height Sim:2 ^{137}Cs seed	^{137}Cs	5.2E+07	0.662	0.851	40	0.851	1.0E+07
Pulse Height Sim:3 Multi- nuc Source	^{210}Pb	3.2E+03	0.047	0.0418	6	0.082	5.0E+07
	^{109}Cd	1.1E+02	0.088	0.0363		0.003	
	^{137}Cs	1.5E+04	0.662	0.851		0.391	
	^{60}Co	1.0E+04	1.173	0.9986		0.262	
	^{60}Co	1.0E+04	1.333	0.9998		0.262	

ii. Material Composition of the Detector for MCNP Simulations

A block within the data card of an MCNP input file defines the material properties by assigning a unique material number to each material, specifying the associated molecular composition of each material. Thus, each cell defined within the cell card is filled by a unique material. The data card of the MCNP input file does not include the density information of the materials. The density is rather specified within the cell card. [135] An example of a data definition card used in the simulations can be seen in Table 5.3.

Table 5.3 MCNP block that defines material composition of the geometry involved.

```
c--------------------------------------------------------------------------------
c LaBr3(Ce) material composition by a mass fraction for gamma-ray transport
c--------------------------------------------------------------------------------
m1      35000   -0.615695       $ Bromine and associated mass fraction
        57000   -0.334505       $ Lanthanum and associated mass fraction
        58000   -0.05           $ Cerium and associated mass fraction
c--------------------------------------------------------------------------------
```

In Table 5.3, “m1” indicates material number 1 which is $LaBr_3$(Ce) crystal. The labels 35000, 57000 and 58000 define elemental Bromine (Z=35), Lanthanum (Z=57) and Cerium (Z=58). Mass fractions of each element are denoted with a minus sign and the sum of the mass fractions should be unity. Figure 5.5 (c) includes information about the filling material of each cell that is defined in the detector geometry. The specifications of the materials defined within the data card of the MCNP input file are shown in Table 5.4.

Table 5.4 Material Specifications used within the MCNP simulations. Values obtained from [136]

Material	Cell Number	Density [g/cm^3]	Element	Label	Mass Fraction
Cerium Activated Lanthanum Bromide	6	5.08	La	57000	-0.334505
			Br	35000	-0.615695
			Ce	58000	-0.050000
Aluminum	7,27,28, 29	2.699	Al	13000	-1.000000
Dry Air	9	0.00121	C	6000	-0.000124
			N	7000	-0.755268
			O	8000	-0.231781
			Ar	18000	-0.012827
SiPM	10,11	2.32	Si	14000	-1.000000
Carbon Steel	20,21,22,23,24,25	7.874	Fe	26000	-0.995000
			C	6000	-0.005000
Polytetra-fluoroethylene	8,30,31	2.2	C	6000	-0.240183
			F	9000	-0.759817
Concrete Wall	23	2.3	H	1000	-0.022100
			C	6000	-0.002484
			O	8000	-0.574930
			Na	11000	-0.015208
			Mg	12000	-0.001266
			Al	13000	-0.019953
			Si	14000	-0.304627
			K	19000	-0.010045
			Ca	20000	-0.042951
			Fe	26000	-0.006435

iii. Pulse Height Tally of MCNP

The detector response of $LaBr_3$ crystal to different sources was simulated in MCNP by using the pulse height F8 tally. The F8 tally determines both the number of particle energies entering and leaving the specified cell. From that information, it calculates the total number of particle energies deposited within the specified cell by subtracting the amount of particle energies leaving the cell from the amount of particle energies entering that cell. The calculated

score is then assigned to an energy bin. [135] The E8 card within the F8 tally card was used to create energy bins manually based on the experimental energy calibration obtained from the pulse-height spectrum of the $LaBr_3$ detector. As discussed in the experimental procedure section, a fixed energy calibration curve was not applicable since the MCA settings differed from source to source. Table 5.5 shows the E8 card definition parameters of each source used within the pulse-height simulations.

Table 5.5 E8 card entries used within pulse-height simulations

Source	**Energy Range [MeV]**	**Number of Channels**	**Energy Resolution**
^{137}Cs-seed	0.052-1.45	1024	1.365 keV/bin
Multi-nuclide	0-2.210	1222	1.809 keV/bin
^{99m}Tc-^{123}I	0-0.4482	1024	0.438 keV/bin

The F8 tally of the MCNP input file also includes the *FT8* Gaussian Energy Broadening GEB card, which allows replication of the energy resolution characteristics of the detector acquired experimentally. One should use this card within the F8 tally in order to have an agreement between the FWHM widths of the energy peaks obtained experimentally and computationally. If this function is not defined within the *F8* tally card, the detected events under the area of the energy peaks will be distributed in a single energy bin. *The FT8 GEB* card is defined by three user provided coefficients: a, b and c. The MCNP code defines the broadening effect of the peaks by an FWHM fit, given in Equation 5.5: [135]

$$FWHM(E) = a + b\sqrt{E + cE^2}\,. \tag{5.5}$$

where *E* is the energy of the photon. The coefficients a, b and c were calculated separately for each simulation by fitting Equation 5.5 to the experimental measurements and using the solver add-in of Microsoft Excel (Microsoft Corporation, Redmond WA) with the spreadsheets for FWHM as a function of energy using the least square fit method. The General Reduced Gradient (GRG) Nonlinear Solving Method in Excel was used to calculate the coefficients, and the resulting values are tabulated in Table 5.6.

Table 5.6 FT8 GEB card coefficients calculated from the FWHM as a function of energy plots.

MCNP Source	**a**	**b**	**c**
^{137}Cs-seed	0.027±0.003	0.0000	0.0000
Multin-nuclide	0.035±0.004	−0.0015±0.0003	29±3.2
^{99m}Tc-^{123}I	0.00856±0.0007	−0.00175±0.0002	−0.57±0.006

5.2.3. Uncertainty Assessment in Experimental Measurements

The uncertainty in photopeak efficiency, percent energy resolution and distance measurements of the detector were calculated based on the propagation of uncertainty principle. Type A components of uncertainty for percentage photopeak efficiency values and the net number of counts detected for distance measurements included: statistical uncertainty

in count rate, uncertainty due to the detector's dead time, which were provided by MCA software. Type B components included: uncertainty in the activity of the source, uncertainty in the half-life of the source and uncertainty in the source-to-detector distance. The contribution to the percent uncertainty of the percentage energy resolution values of the detector was from uncertainty due to the dead time of the detector and statistical uncertainty in count rate which were provided by MCA software.

5.3. Results

5.3.1. Dark Current and Background Measurement

In Figure 5.6 shows how the area under the background counts, indicated by tan color, and relates to the total counts for the multi-nuclide source. The area under the total counts obtained from the source and minus the background yields the net counts, shown by the green area. The background subtraction was applied to all spectra acquired experimentally.

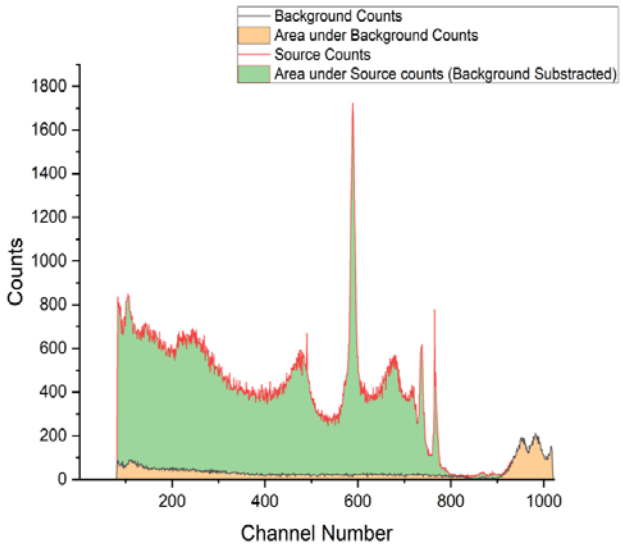

Figure 5.6 The spectrum of the multi-nuclide source and background. The figure is drawn to show the background (in tan) that is subtracted from the total counts to give the net counts (in green).

5.3.2. Experimental Curve for the Energy Resolution

The percentage energy resolution of the detector as a function of the incoming photon energy is shown in Figure 5.7 (a). The measured points fitted to Power-law equation by using least-squares method is shown with a dashed line. The Power law equation is expressed in ($a*E^b$) and the coefficients a and b were calculated as 659.6 and -0.929, respectively.

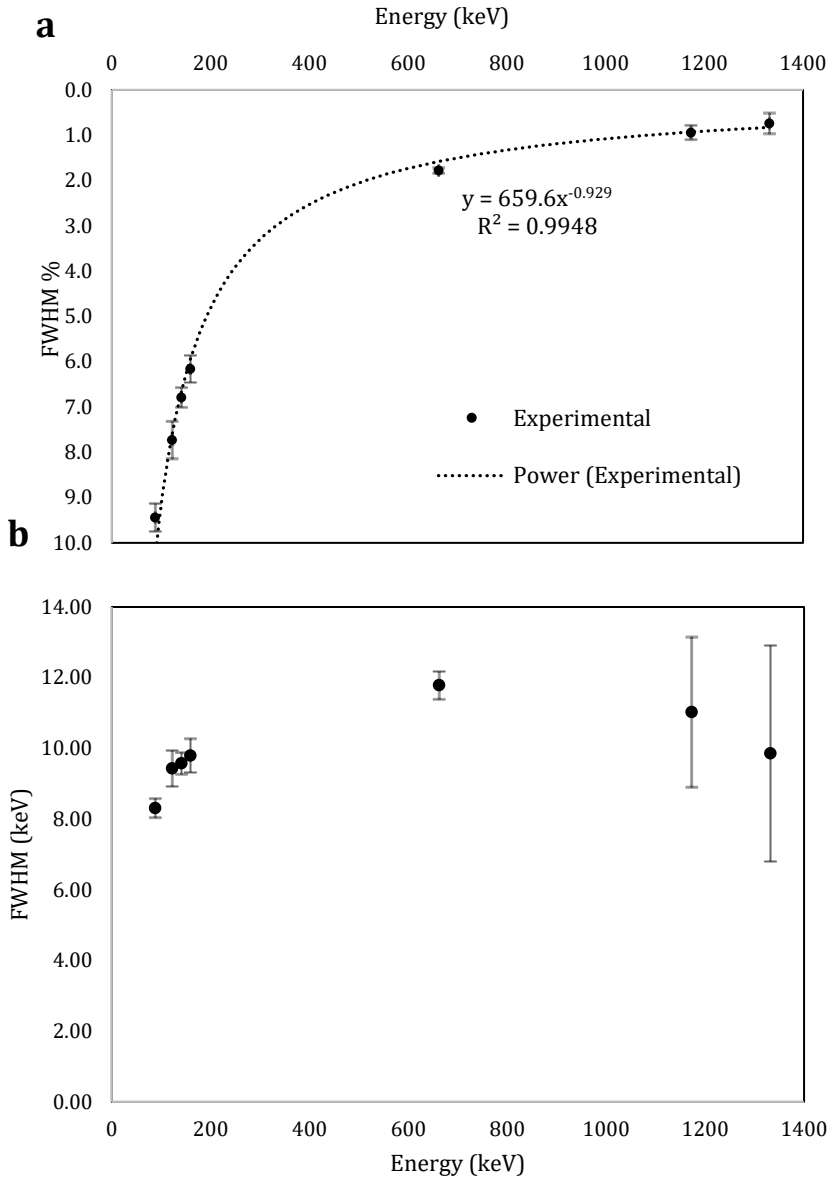

Figure 5.7 The detector's energy resolution (FWHM) as a function of incident photon energy: (a.) in terms of the percentage energy resolution, (b) in terms of energy.

The 1.78%±0.06% energy resolution at 662 keV energy compares favorably with commercial detectors, which run between 3% and 10%, except for the very small volume

CdZnTe detectors, which fall about 1.8%. [137, 119, 112, 113]Figure 5.7 (b) shows the same data as Figure 5.7 (b) but in units of *keV*. Below 200 keV for the incident photon energy, the energy resolution of the detector remains under 10 keV. This energy resolution will allow differentiation between the ^{123}I and ^{99m}Tc radiation.

5.3.3. Experimental Curve of the Photopeak Efficiency

The plot in Figure 8 shows the absolute photopeak efficiency of the $LaBr_3$(Ce) detector as a function of the incident photon energy. The curve in Figure 5.8 was fitted to a power law equation, expressed by Equation 5.6.:

$$\varepsilon = a * E^b. \tag{5.6}$$

In Equation 5.6, ε is the absolute percentage photopeak efficiency of the detector, *E* is the energy of the incident photon in keV, and a, b are the fit coefficients, which were calculated as a= 176.65 and b= -1.374, using the least-squares method. The efficiency curve in Fig.8 follows the trend of inverse power of the energy, as expected since the interaction probability of the photoelectric effect is inversely proportional to the power of the energy.

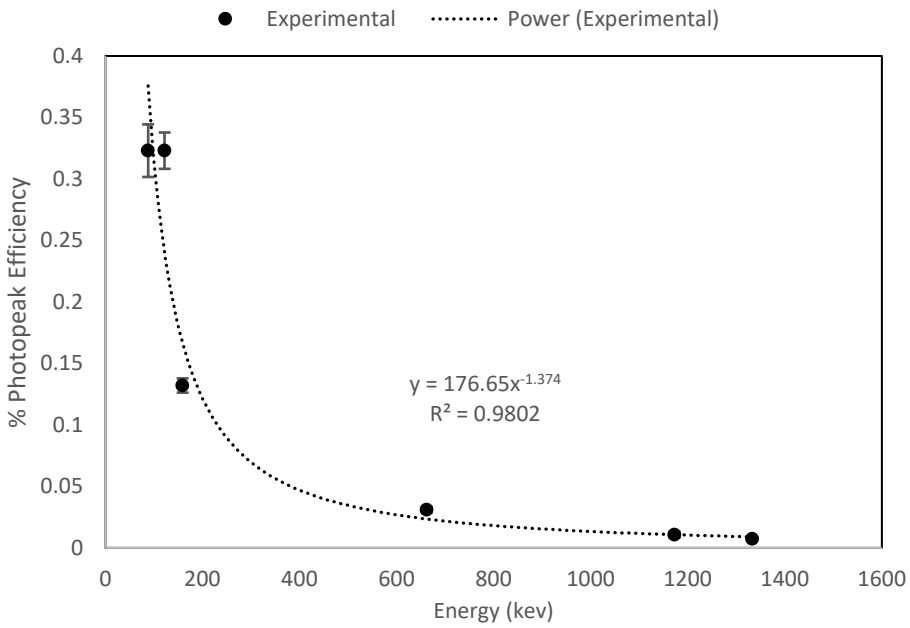

Figure 5.8 The plot of the percentage photopeak efficiency of the detector as a function of the incident photon energy.

5.3.4. Distance Measurements

The response of the detector as a function of source-to-detector distances is shown by the curve plotted in Figure 5.9. The curve is fitted to power equation as illustrated by Equation 5.7 in which *N* is the number of net counts detected per unit time (cps), *x* is the SSD in cm, a and b are fitting coefficients, which were calculated by the least-squares method. :

$$N = a * x^{b} . \qquad (5.7)$$

The coefficients a and b are found to be 11583 and -1.992, respectively. The curve closely follows the expected inverse-square law trend.

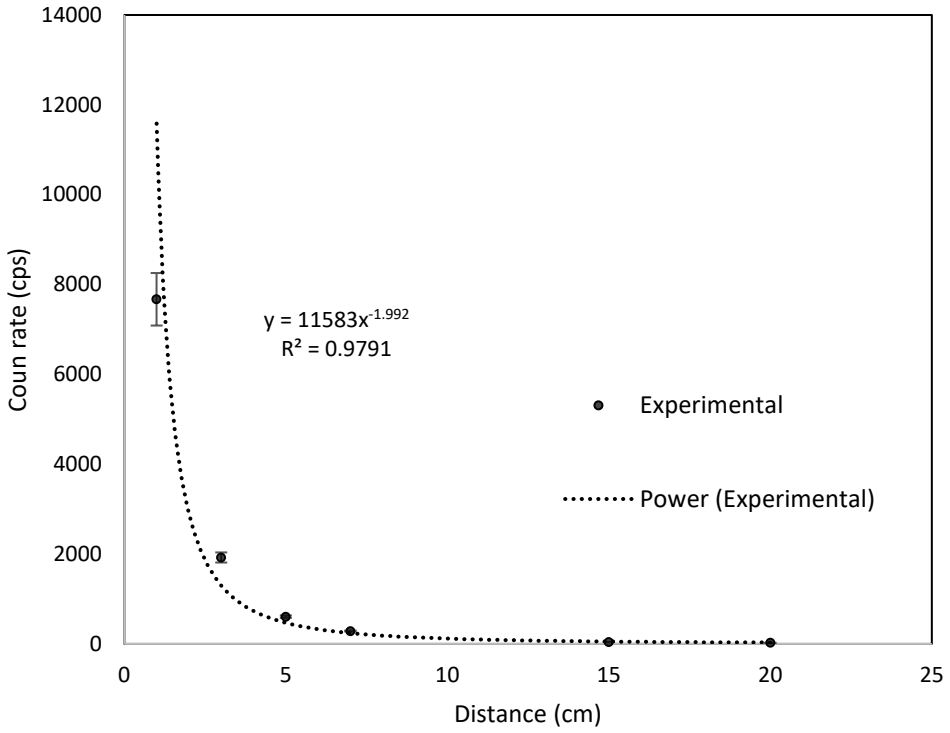

Figure 5.9 Graphical presentation of the count rate of the detector as a function of distance for the ^{57}Co source.

5.3.5. Monte Carlo Simulations

The spectra of the combined ^{99m}Tc and ^{123}I, the multi-nuclide and ^{137}Cs sources acquired experimentally were compared to those obtained in MCNP simulations for the validation, as seen in Figure 5.10, Figure 5.11 and Figure 5.12.

Before the comparison of the experimental and computational curve in Figure 5.10, it should be highlighted that 141 keV energy of the ^{99m}Tc is clearly resolved from the 159 keV energy of the ^{123}I, as seen on the experimental curve of Figure 5.10.

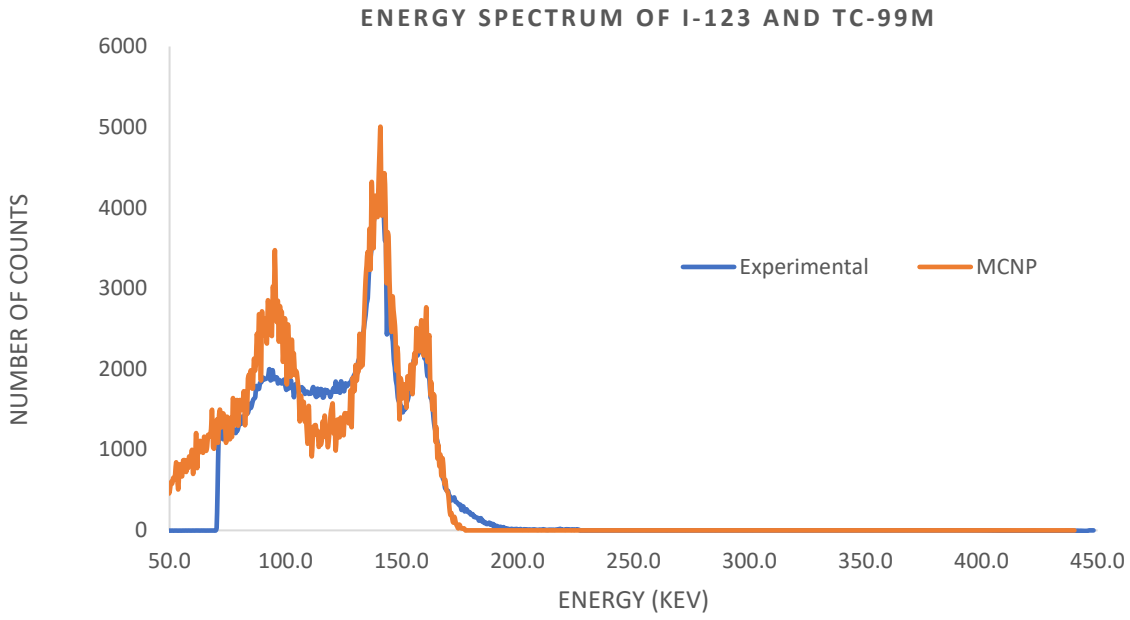

Figure 5.10 The energy spectrum of the combined ^{123}I and ^{99m}Tc source, experimentally and simulated with MCNP.

The curves in Figure 5.10 are in agreement with each other except in the Compton valley region and at extremely low energies. The difference in the Compton valley is because MCNP tallies one photon at a time and does not allow for multiple events simultaneously, resulting in a clean shape for the curve. In the experiment, the summed Compton events appear shifted to the higher energy of their combination.

Experimental and MCNP curves in Figure 5.11 have a good agreement at photopeak energies of 662 keV from ^{137}Cs, and 1173 and 1333 keV from ^{60}Co source. The discrepancy observed between two curves at the energy values below ~200 keV is due, again to summation events as well as the scattering of the photons from the surrounding materials in the environment in which the experiments was performed. [138] Since it was not feasible to model every detail of the geometry and material compositions of the room in MCNP, the scatter from the surrounding materials are not represented in the MCNP curve.

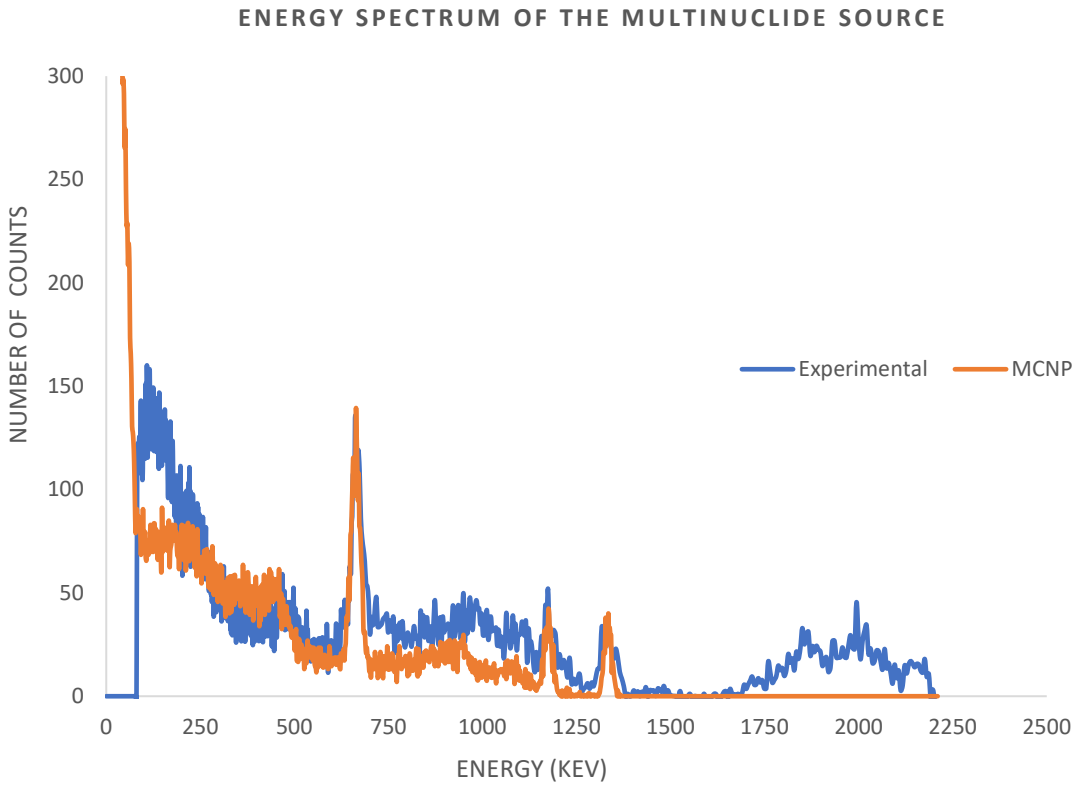

Figure 5.11 The energy spectrum of the multi-nuclide source, experimentally and simulated with MCNP.

Figure 5.12 shows the energy spectrum for a ^{137}Cs source. In general, the two curves match well in the peak and Compton regions. The two bumps on each side of the photopeak present in the experimental curve come from the detection of the summed events in the experiment, and again do not show up in MCNP simulations. Scattering from the surrounding materials in the room of experiments caused a rise in the region of the experimental curve having energies below 200 keV, which was not represented in the MCNP curve.

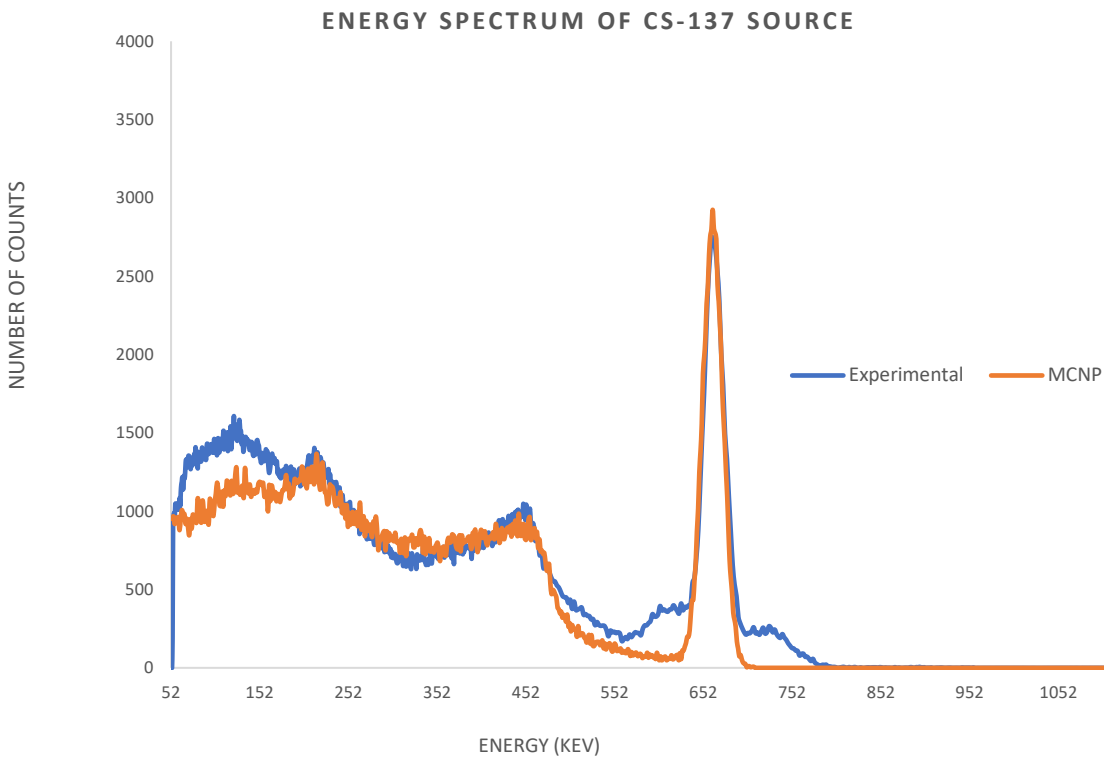

Figure 5.12 The energy spectrum of the ^{137}Cs source, experimentally and simulated with MCNP.

5.3.6. Uncertainty in Experimental Results

The total percent standard uncertainty in energy resolution values in Section 5.3.2 was found to vary between 1.2-3.8% for the energy range of 88-662 keV. However, above 662 keV, for at 1173 and 1333 keV photopeak energies of the ^{60}Co source, the percent standard uncertainty in energy resolution varied between 14.4-23%. This is due to the low activity of the ^{60}Co source within the multi-nuclide causing high count statistics uncertainties even for long acquisition times.

The total percent standard uncertainty in photopeak efficiency values in Section 5.3.3, on the other hand, changed between 4.-7.6% for the energy range of 88-662 keV. For higher energies, large uncertainties in photopeak efficiency values were observed because of the low activity of the ^{60}Co source during the experiments.

The total percent uncertainty in the net count rates as a function of the source-to detector distance that varied between 1-20 cm ranged between 3.9-7.6%. Further uncertainty justification can be found in Table B.1, Table B.2 and Table B.3 in Appendix B.

5.4. Conclusion

By having an energy resolution of 1.78±0.06 % at 662 keV energy and having a capability to distinguish between 141 keV and 159 keV energy, the detector was found to have the necessary characteristics for the imaging procedures that need to differentiate between ^{123}I and ^{99m}Tc, such as in a surgical setting. Overall, very good agreement between experimental and MCNP curves of the energy spectrum was observed. The desirable detector's characteristics

that were ascertained in this work along with the detectors compact mobile design supported the design and development of a system for radio-guided surgery.

6. Collimation Design for the Detector

6.1. Introduction

The overall sensitivity of a detector is the ability to detect a radioactive source placed at a certain distance along the center axis of the probe tip, which is often reported in the units of counts per second per unit activity of the radioactive source (cps/MBq). [58] In radio-guided surgery applications, specifically to image the 3D radioactivity distribution of the radioactive sources, the sensitivity of the radiation detector must be high enough, so that each radiation type coming from each source can be detected separately.

Spatial resolution, or lateral sensitivity, of a detector is the ability to determine the location of a target radioactive source placed at a certain longitudinal and lateral distance from the tip of the detector, which is often given as the full-width half maximum (FWHM) in mm. [58] It is a crucial characteristic of a detector when localizing and resolving deep-seated lymph nodes, specifically when they are close to each other at depth.

Both sensitivity and spatial resolution are dependent on the collimation type and collimation geometry used with the detector. As discussed in previous chapters, this project aims to localize and image whole breast tumor and SLN intraoperatively, by localizing tumor containing ^{123}I and SLN containing ^{99m}Tc. The approximate activity of SLNs was reported as 1 MBq in a clinical study. The SNs had a median diameter of 1 cm at a maximum depth of 4.3 cm from the skin. [54, 55] [56] No clinical study was found in the literature that reports the uptake of the breast tumor masses after the injection of the CLR1404 labeled with any radioisotpoe of Iodine. However, the clinical study performed by *Weichert et. al* showed that the radioactivity uptake of the CLR1404 pharmaceutical in breast cells was considerably high. [104] A typical non-palpable breast tumor is expected to have more than 1 MBq ^{123}I residual radioactivity uptake and have a median spherical diameter of 1 cm at a median depth of 3.3 cm from the skin. [50] [51] The minimum center-to-center separation between two clusters of nodes at depth is reported as 10 mm. [54] This data indicates that a detector needs a spatial resolution of about 5 mm at a source to collimator surface distance (SCD) of 3.3 cm to identify the edges of a breast tumor or a minimum 10 mm spatial resolution at an SDD of 4.3 cm to resolve lymph nodes.

The freehand SPECT system discussed previously is unable to resolve the clustered nodes separated by 10 mm at 40 mm depth. [54] This chapter focuses on the collimation design for the handheld radiation detector built and characterized in Chapters 4 and 5. The required spatial resolution and sensitivity values, discussed above, should be met for the precise localization of both SLNs and breast tumors. Since there is a known trade-off between sensitivity and spatial resolution of a detector, a double layer collimation design is proposed in

this work to optimize spatial resolution and sensitivity while minimizing weight. The geometric model parameters of the collimation were varied one at a time in both experiments and Monte Carlo simulations to investigate the change in the spatial resolution and sensitivity and thereby to determine the optimum values for both characteristics of the detector. The resulted optimum values are then compared to existing literature.

6.2. Materials and Methods

6.2.1. Proposed Collimation Design

As prevoiusly discussed in the introduction section, the sensitivity and spatial resolution of a detector go hand in hand. Based on the specific task required, one should define the approximate values needed. In our case, we are trying to find a spatial resolution about 5 mm or less at a source-to-detector distance of 3.3 cm based on the characteristics and geometry of the tumor and SLNs as explained above. However, in order to make measurements easier for the surgeon a spatial resolution between 5-7 mm at a source-to-detector distance of 10 cm is desired. That means our target is going to require the spatial resolution (~5mm) but for larger SCD (10 cm). Since having this resolution alone is not enough, the second requirement was to achieve the minimum detectable activity of 1 MBq which is accompanying a spatial resolution of 5 mm at 10 cm SCD. Collimation material and geometry are the key parameters that will determine these two goals. Hence, we proposed a double collimator, as seen in Figure 6.1. From two options for the collimator's material that both have high atomic numbers, lead and tungsten, lead was chosen due to the expense of tungsten and its brittle nature. The advantage

of tungsten would have been that the collimator would be thinner, but that was not a high priority. Figure 6.1 shows the detector with two separate collimators attached. The rear collimator is attached to the detector and front collimator fits snugly over the rear collimator. Each collimator has its own aperture. The *x1*,*x2*,*t1*,*t2*, *d1*and *d2* intervals are named as geometric model parameters of the collimation, which are: *x1* is the distance between rear collimation and detector surface, *x2* is the distance between front and rear collimation, *d1* and *d2* aperture hole diameters of the front and rear collimator respectively, and *t1* and *t2* are the thicknesses of the front and rear collimators, respectively. Sensitivity and spatial resolution ofthe detector were investigated both experimentally and in MCNP simulations by changing each model parameter one at a time, or varying two of the parameters and keeping the others fixed.

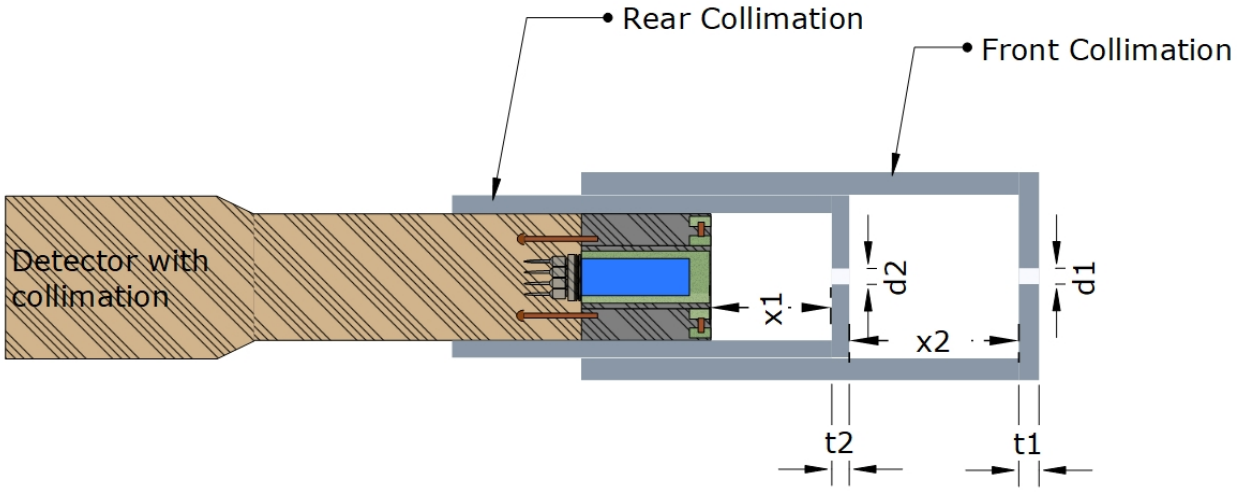

Figure 6.1 Schematic drawing of the detector with proposed double layer colllimation attached.

6.2.2. Experimental Procedure

i. Experimental Setup

The detector in this study was described in detail in the previous chapter, and used a 10mm diameter x 25mm long $LaBr_3$(5%-Ce) cylindrical scintillation crystal sealed in a 4.75mm diameter (top) x 2 mm long (side) thick reflector of polytetrafluoroethylene, all of which was hermetically sealed in a 0.25 mm diameter (top) x 0.25 mm long (side) thick aluminum housing. The bottom of the housing was coupled to a 12.46 mm x 12.46 mm silicon photomultiplier.

ii. Sensitivity Measurements

A ^{99m}Tc source was placed at a source-to-front collimator distance (SCD) of 10 cm as seen in Figure 6.2. The sensitivity of the detector was calculated from Equation 6.1 for each set of parameters. :

$$Sensitivity\ (cps/MBq) = \frac{\left(\frac{N}{T}\right)(cps)\ \times\ 10^6\left(\frac{Bq}{MBq}\right)}{A_0(\mathrm{Bq}) * \exp\left(-\frac{ln2}{t_{1/2}}\ \times t\right) * BR} \qquad (6.1)$$

In Equation 6.1; N is the number of net counts detected under the photopeak after background subtraction, A_0 is the initial activity of the ^{99m}Tc source, $t_{1/2}$ is the half-life of the ^{99m}Tc, t is the

decay time, *BR* is the gamma emission probability of the ^{99m}Tc source at 141 *keV* photopeak energy and *T* is the acquisition time.

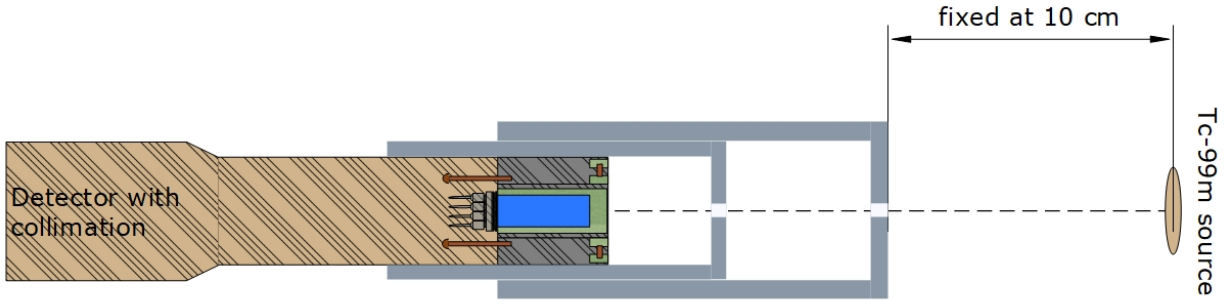

Figure 6.2 Schematic drawing of the experimental setup for sensitivity measurements.

iii. Spatial Resolution Measurements

As in Figure 6.3, the ^{99m}Tc source was placed along the axis of the detector at 10 cm SCD and was moved along the horizontal plane in 0.5-10 mm increments to get the horizontal count profile of the detector as a function of distance from the axis. The net counts detected under photopeak of each position was obtained and the net count rate as a function of x distance was plotted. Figure 6.4 presents an example curve from the data. The resultant count profile was fitted to a Gaussian curve by using Origin Pro® 9.1 Data Analysis and Graphing Software (Origin Lab Corporation, DPR Group, Inc. Northampton, MA) which uses the Levenberg Marquardt iteration algorithm to determine full-width-at-half-maximum (FWHM) of the

Gaussian function. FWHM values provided by the software were noted as the spatial resolution of the detector at a specific scenario having specific model parameters in Figure 6.1.

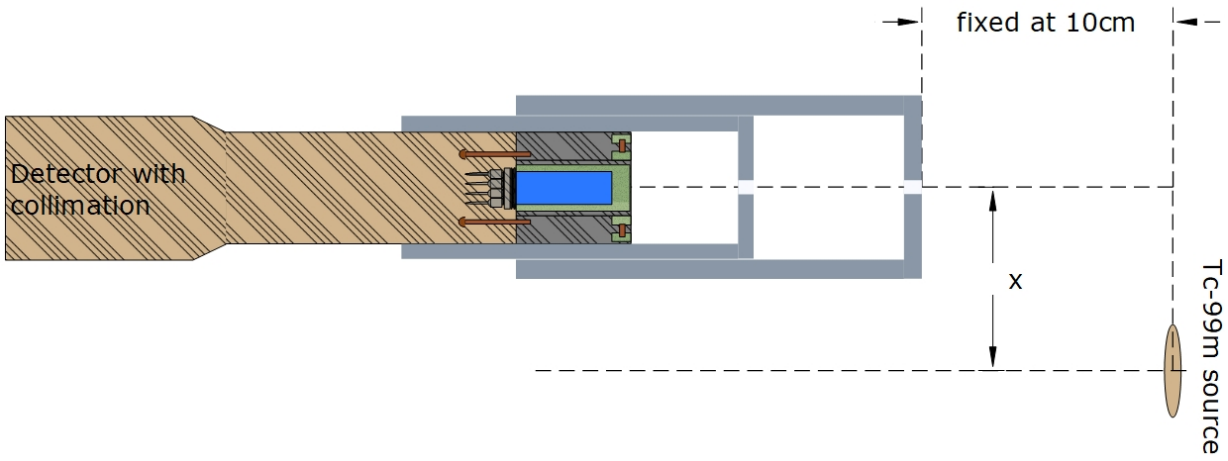

Figure 6.3 Schematic drawing of the experimental and MCNP setup for spatial resolution measurements.

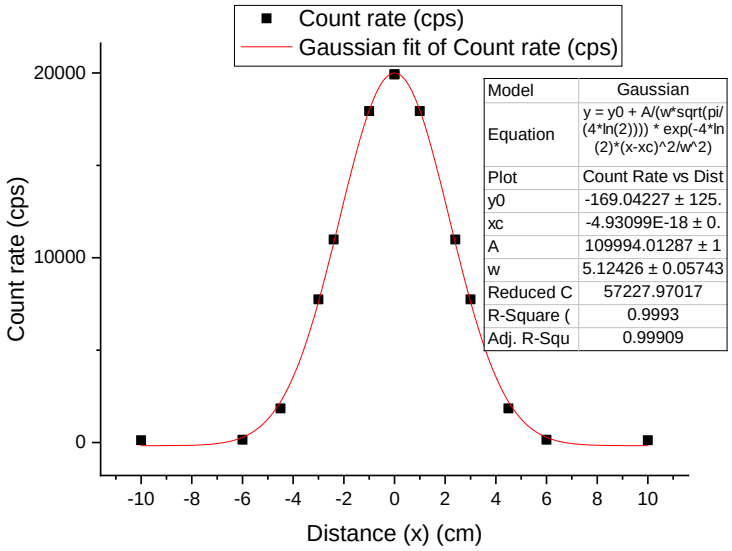

Figure 6.4 Count profile of the detector that is used to fit Gaussian curve for spatial resolution determination.

iv. Spectrum Measurement

Following the determination of the optimum model parameters that provided optimum sensitivity and resolution based on the interpretation of the results of the experiments, the energy spectrum of the ^{99m}Tc source at 10 cm SCD was acquired.

6.2.3. Monte Carlo Simulations

The detector geometry with optimum collimation geometry that was determined based on the experimental results was simulated by using Monte Carlo MCNP6/MCNPX software [Triad National Security, LLC, manager, and operator of LANL, Los Alamos, NM] in order to compare and validate experimental energy spectrum of the source with the one simulated in MCNP. Different scenarios for geometric model parameters, which were not performed in experiments, were simulated in MCNP to get a wider range of values for sensitivity and spatial resolution pair.

i. Modeling of the Geometry of the Detector and Materials Composition

The collimated detector with the optimum model parameters was simulated in MCNP. The same detector geometry, as in Figure 5.5 (c) in Chapter 5, was modeled in MCNP by defining surface, cell and data cards except the lead collimation added as seen in Figure 6.5. The gray areas in Figure 6.5 (a) and the read areas in Figure 6.5 (b) represent the lead filled front and rear collimations. The composition of materials for each cell is defined within the data card of the MCNP input as seen in Table 5.3 of Chapter 5 except new cells, cell 32 and

33, were defined for front and rear lead collimations. The cells 32 and 33 was filled with pure lead having a density of 11.35 g/cm^3, a label number of 82000 and a mass fraction of 1.0. [136]

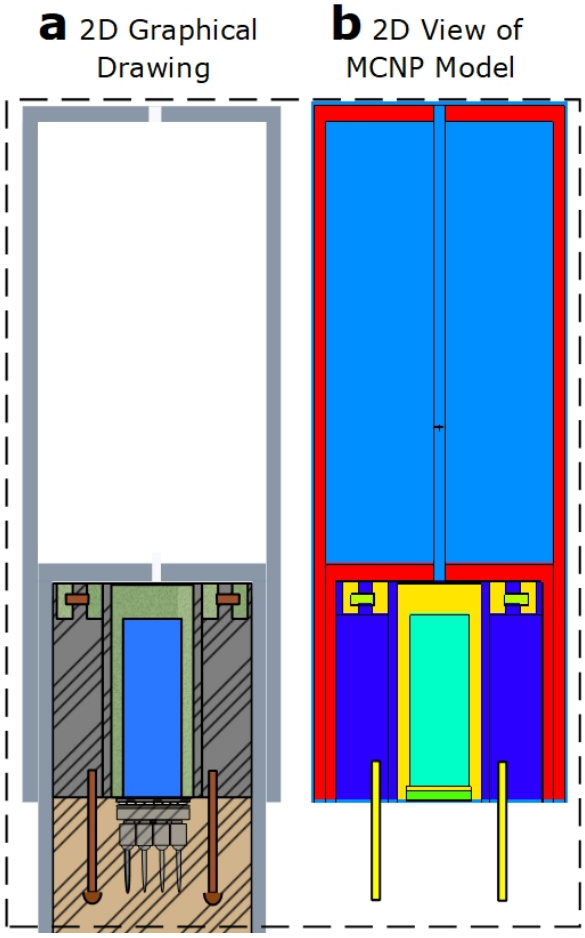

Figure 6.5 The geometry of the collimated detector that is shown in a (a) graphical 2D drawing (b) modeled in MCNP.

ii. The Source and Pulse Height Tally Definition

As described in Section 5.2.2 (iii) of Chapter 5, a point source approximation was used for ^{99m}Tc source sitting at 10 cm of SCD. SDEF card of the MCNP was defined as having a

^{99m}Tc source which is emitting photons (*PAR=2*) with energy of photons (*erg)* of 141 keV, at a position of (*POS=0 0 20.37*) 10 cm from the surface of the front collimation. Pulse Height (*F8*) tally was defined in terms of two parameters: *E8* and *FT8* cards as explained in the previous chapter. The input values for *E8* card within the pulse height tally included: energy range of the spectrum, number of channels in the spectrum and energy resolution of each bin of the spectrum which were determined as 0-0.679 MeV, 1024 channels and 0.663 keV/bin, respectively. The Gaussian Energy Broadening *(GEB)* cofficients of the *FT8* card were calculated as a=0.0122 b=-0.007 and c=0 by using least-least squares fit method as discussed earlier in Section 5.2.2 (iii) of Chapter 5. .

iii. Sensitivity Simulations

The sensitivity of a detector in MCNP can be determined by using Surface Current (*F1)* tally. As seen in Figure 6.6, In MCNP, Surface 12.3 represents the cylindrical front surface of the detector. If a specified particle crosses a specified surface in the geometry of the detector, the weight of this particle counted in the the total weight and reported as *F1* tally. [135] This is basically the fraction of the total number of the particles crossing the specified surface to the total number of particle energies simulated *(NPS*). Using the source and detector geometry in Figure 6.2 and Figure 6.5 (b), the sensitivity of the detector crossing the surface 12.3 in Figure 6.6 for each scenario, in which one or two model parameters were changed, was calculated by using Equation 6.2:

$$S[cps/MBq] = w\left[\frac{counts}{particles}\right] \times NPS[particles/sec]\ X\ 10^{6}\left[\frac{Bq}{MBq}\right] . \qquad (6.2)$$

where; *w* is the total weight of the peak energy particles crossing the surface 12.3 in Figure 6.6, or namely, the fraction of the photons with the peak energy crossing the surface 12.3 divided by the total number of particles simulated (*NPS).* (10^6 Bq/MBq) was added in Equation 6.4 in order to convert the unit of the sensitivity from (counts detected/photons simulated) to (cps/MBq).

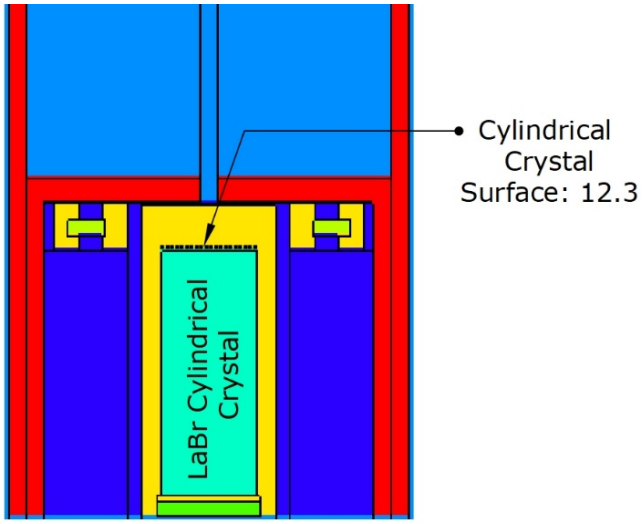

Figure 6.6 Schematic of the active surface area of the detection crystal tallied in MCNP.

iv. Spatial Resolution Simulations

Average surface Flux tally *(F2)* is the another output option of the MCNP which defines fluence at the specified surface. The weight of each particle with phopeak energy that crosses the specified surface and contributes to the fluence at that surface is summed and reported as the *F2* tally in the ouput. [135] The weight of the fluence at the surface 12.3 in Figure 6.6 was

provided by the MCNP for different x distances along the horizantal plane in Figure 6.3. The average flux at surface 12.3 for each case is then calculated by using Equation 6.3:

$$Flux\ \left[\frac{counts}{cm^2}\right] = W\ \left[\frac{counts/cm^2}{particles}\right] \times NPS\ [particles]\ . \qquad (6.3)$$

where, *W* is the weight of the flux at the surface 12.3 provided by MCNP, or it is the flux detected on the surface 12.3 divided by (*NPS)* which is the number of particles simulated. The flux profile of the detector as a function of x distances is then plotted as illustrated in Figure 6.4. The resulted flux profile was fitted to a Gaussian curve by using Origin Pro® 9.1 Data Analysis and Graphing Software discussed previously. FWHM values provided by the Origin Pro 9.1 software were then noted as the spatial resolution of the detector at a specific scenario having a unique combination of model parameters in Figure 6.1.

6.2.4. Uncertainty Assessment

i. Experimental Uncertainty

The contribution to the total percent standard uncertainty in experimantal sensitivity and spatial resolution was from uncertainty in the activity of the source, uncertainty in the half-life, uncertainty in the distance as the Type B components, and uncertainty due to the count statistics and dead time as the Type A components. However, the uncertainty provided by Origin Pro

9.1 software in determing FWHM of the Gaussian curve was added to the Type A uncertainty in spatial resolution. The quadratic sum of each components was taken seperately for Type A and Type B and resulted values were quadratically combined to determine the total percent uncertainty in the sensitivity and spatial resolution.

ii. Uncertainty of the Simulations

Total percent uncertainity in the sensitivity and spatial resolution of the detector was provided by MCNP except uncertainity in spatial resolution included the uncertainty in FWHM provided by Origin Pro 9.1 software.

Table 6.1 The sensitivity and spatial resolution of detector obtained in experiments.

SCD (cm)	t1 mm	t2 mm	d1 mm	d2 mm	x1 mm	x2 mm	Spatial Res (mm)	Sensitivity (cps/MBq)	SCD cm	t1 mm	t2 mm	d1 mm	d2 mm	x1 mm	x2 mm	Spatial Res (mm)	Sensitivity (cps/MBq)
10	2.2	2.2	2.0	2.0	0	0	22.0	10.98	10	2.2	2.2	2.8	3.3	0	25	15.0	10.29
10	2.2	2.2	2.0	2.0	0	2	20.0	9.26	10	2.2	2.2	0.5	0.5	0	0	17.0	0.34
10	2.2	2.2	2.0	2.0	0	4	17.0	9.22	10	2.2	2.2	1.8	1.8	0	12.5	16.0	7.11
10	2.2	2.2	0.8	0.8	17	0	22.0	1.53	10	2.2	2.2	1.8	1.8	0	25	10.0	3.91
10	2.2	2.2	0.8	0.8	17	5	15.0	1.41	10	2.2	2.2	1.8	0.5	0	35	6.0	1.82
10	2.2	2.2	0.8	0.8	17	10	13.0	1.41	10	2.2	2.2	1.2	1.2	0	10	16.0	3.13
10	2.2	2.2	0.8	0.9	0	10	13.0	1.53	10	2.2	2.2	1.2	1.2	0	25	8.5	1.99
10	2.2	2.2	0.8	0.9	0	15	9.0	1.22	10	2.2	2.2	1.8	1.8	0	35	8.5	4.46
10	2.2	2.2	1.0	1.0	0	10	13.0	2.19	10	2.2	2.2	1.8	1.8	0	45	7.0	2.80
10	2.2	2.2	1.2	1.0	0	10	13.0	1.28	10	2.2	2.2	1.4	1.5	0	25	8.0	1.63
10	2.2	2.2	1.2	1.0	0	15	9.0	1.03	10	2.2	2.2	1.8	1.8	0	45	6.0	2.22
10	2.2	2.2	0.5	0.5	0	0	14.0	0.98	10	2.2	2.2	1.8	1.8	0	40	6.0	3.97
10	2.2	2.2	0.5	0.5	0	5	8.0	0.88	10	2.2	2.2	1.8	3.2	0	40	10.0	9.77
10	2.2	2.2	0.5	0.5	0	10	6.0	0.69	10	2.2	2.2	3.5	3.2	0	40	15.0	14.73
10	2.2	2.2	0.5	0.5	0	15	3.5	0.21	10	2.2	2.2	4.4	4.8	0	40	20.0	32.73
10	2.2	2.2	0.5	0.5	5	0	13.0	0.76	10	2.2	2.2	4.4	4.8	0	65	13.0	24.68
10	2.2	2.2	0.5	0.5	10	0	13.0	0.82	10	2.2	2.2	4.4	4.8	0	85	11.0	24.16
10	2.2	2.2	0.5	0.5	15	0	13.0	0.77	10	2.2	2.2	4.4	4.8	0	100	7.0	10.58
10	2.2	2.2	0.5	0.5	5	5	6.0	0.61	10	2.2	2.2	4.8	4.8	0	85	10.0	22.18
10	2.2	2.2	0.5	0.5	10	10	3.0	0.11	10	2.2	2.2	4.8	4.8	0	100	9.0	18.87
10	2.2	2.2	0.5	0.5	10	5	3.5	0.21	10	2.2	2.2	5.2	5.2	0	85	8.5	22.20
10	2.2	2.2	0.5	0.8	0	0	19.0	1.19	10	2.2	2.2	5.2	5.2	0	100	9.0	14.89
10	2.2	2.2	0.5	0.8	0	5	10.0	1.08	10	2.2	2.2	5.9	6.7	0	85	14.0	32.05
10	2.2	2.2	0.5	0.8	0	10	7.0	0.87	10	2.2	2.2	6.7	6.7	0	85	15.0	42.39
10	2.2	2.2	0.5	0.8	0	15	4.0	0.39	10	2.2	2.2	7.6	7.6	0	85	18.0	54.52
10	2.2	2.2	0.5	0.8	5	0	15.0	0.88	10	2.2	2.2	7.6	8.4	0	85	15.0	56.03
10	2.2	2.2	0.5	0.8	10	0	14.0	0.94	10	2.2	2.2	9.4	8.4	0	85	15.0	58.05
10	2.2	2.2	0.5	0.8	15	0	14.0	0.83	10	1.8	1.8	1.8	1.7	0	65	5.5	1.57
10	2.2	2.2	0.5	0.8	5	5	10.0	0.82	10	1.8	1.8	1.8	1.8	0	65	5.0	3.49
10	2.2	2.2	0.5	0.8	7.5	7.5	7.0	0.48	10	1.8	1.8	1.8	1.9	0	65	5.5	4.40

Table 6.1 Continued.

10	2.2	2.2	1.0	0.8	7.5	7.5	11.0	1.30	10	1.8	1.8	2.3	1.9	0	65	6.5	5.52
10	2.2	2.2	1.0	0.8	5	5	14.0	1.95	10	1.8	1.8	2.3	2.3	0	65	8.0	7.08
10	2.2	2.2	1.0	0.8	0	5	11.0	2.28	10	1.8	1.8	2.3	2.3	0	85	7.0	5.02
10	2.2	2.2	1.0	0.8	0	10	9.5	2.13	10	1.8	1.8	2.3	2.3	0	110	6.0	4.99
10	2.2	2.2	1.0	0.8	0	15	6.0	1.12	10	1.8	1.8	3.0	2.3	0	65	8.0	8.40
10	2.2	2.2	1.0	0.8	15	0	16.0	2.53	10	1.8	1.8	3.4	4.8	0	65	11.0	17.91
10	2.2	2.2	1.0	0.8	10	0	19.0	2.55	10	1.8	1.8	3.4	4.8	0	105	7.0	17.31
10	2.2	2.2	1.0	0.8	0	0	27.0	2.64	10	1.8	1.8	4.8	4.8	0	105	9.0	21.35
10	2.2	2.2	1.2	1.5	0	0	29.0	4.95	10	1.8	1.8	4.8	5.9	0	105	9.0	24.02
10	2.2	2.2	1.2	1.5	0	5	19.0	3.88	10	1.8	1.8	7.1	5.9	0	105	13.0	29.08
10	2.2	2.2	1.2	1.5	0	10	13.0	3.11	10	1.8	1.8	7.1	7.1	0	105	12.0	38.86
10	2.2	2.2	1.2	1.5	0	15	10.0	2.04	10	2.2	2.2	2.8	2.8	0	25	17.0	19.29
10	2.2	2.2	1.2	1.5	10	15	10.0	0.89	10	2.2	2.2	4.4	4.4	0	25	25.0	44.65
10	2.2	2.2	1.2	1.5	10	0	25.0	3.88	10	1.8	1.8	1.6	1.6	0	65	5.0	2.47
10	2.2	2.2	1.2	1.5	5	0	26.0	4.01	10	1.8	1.8	1.8	1.6	0	65	6.0	2.72
10	2.2	2.2	1.5	2.5	0	0	32.0	4.67	10	1.8	1.8	1.8	1.8	0	65	6.5	3.20
10	2.2	2.2	2.0	2.5	0	0	40.0	8.76	10	1.8	1.8	1.8	2.2	0	65	6.0	3.58
10	2.2	2.2	2.0	2.5	0	10	21.0	7.00	10	1.8	1.8	2.2	2.2	0	65	7.0	7.24
10	2.2	2.2	2.0	2.5	0	10	15.0	5.58	10	1.8	1.8	2.8	2.2	0	65	8.0	8.49
10	2.2	2.2	2.0	2.5	0	25	10.0	1.00	10	1.8	1.8	2.8	2.2	0	85	6.3	6.80
10	2.2	2.2	2.5	2.5	0	10	25.0	8.47	10	1.8	1.8	2.8	2.8	0	85	7.0	10.49
10	2.2	2.2	2.5	2.5	0	25	10.0	2.42	10	1.8	1.8	2.8	3.2	0	85	7.5	14.27
10	2.2	2.2	2.5	2.8	0	25	8.0	4.11	10	1.8	1.8	3.0	3.2	0	85	8.0	14.49
10	2.2	2.2	2.7	2.8	0	25	10.0	5.02	10	2.5	2.5	1.6	1.6	0	65	5.5	2.08
10	2.2	2.2	2.8	2.8	0	25	11.0	4.44	10	2.5	2.5	1.8	1.6	0	65	5.2	2.43
10	2.2	2.2	2.8	3.3	0	25	9.5	3.97	10	2.5	2.5	1.8	1.8	0	65	4.5	2.84
10	2.2	2.2	2.8	3.6	0	25	12.0	7.32	10	2.5	2.5	2.0	1.8	0	65	6.0	4.00
10	2.2	2.2	3.6	3.6	0	20	22.0	14.39	**10**	**2.5**	**2.5**	**2.0**	**2.0**	**0**	**65**	**4.7**	**5.78**

6.3. RESULTS

6.3.1. Experimental Results

Table 6.1 tabulates the sensitivity and spatial resolution values obtained in the experiments. Experiments consisting of a total of 116 combinations, which had ~1000 measurements points, were performed for various scenarios of model parameters shown in Table 6.1. The combination with the highest sensitivity was selected from the combinations of model parameters providing a spatial resolution value of 7 mm or better at 10 cm SCD. This setting was deemed the optimum collimation geometry, which provided a sensitivity of 5.78±0.24 cps/MBq and a spatial resolution of 4.7±0.22 mm at 10 cm SCD.

6.3.2. MCNP Results

i. Validation of the Pulse Height Spectrum

Although 116 different model parameter combinations were used in the experiments, untested combinations remained to be evaluated by Monte Carlo simulation. The energy spectrum of the ^{99m}Tc source measured with the optimum collimator in place was simulated in MCNP and compared to that obtained in the experiment. Figure 6.7 shows this comparison.

There is a very good agreement between two curves in Figure 6.7, except the MCNP curve is cleaner on the lower sides of the photopeak. As explained in Chapter 5, that is because summed events cannot be represented in MCNP pulse height tally.

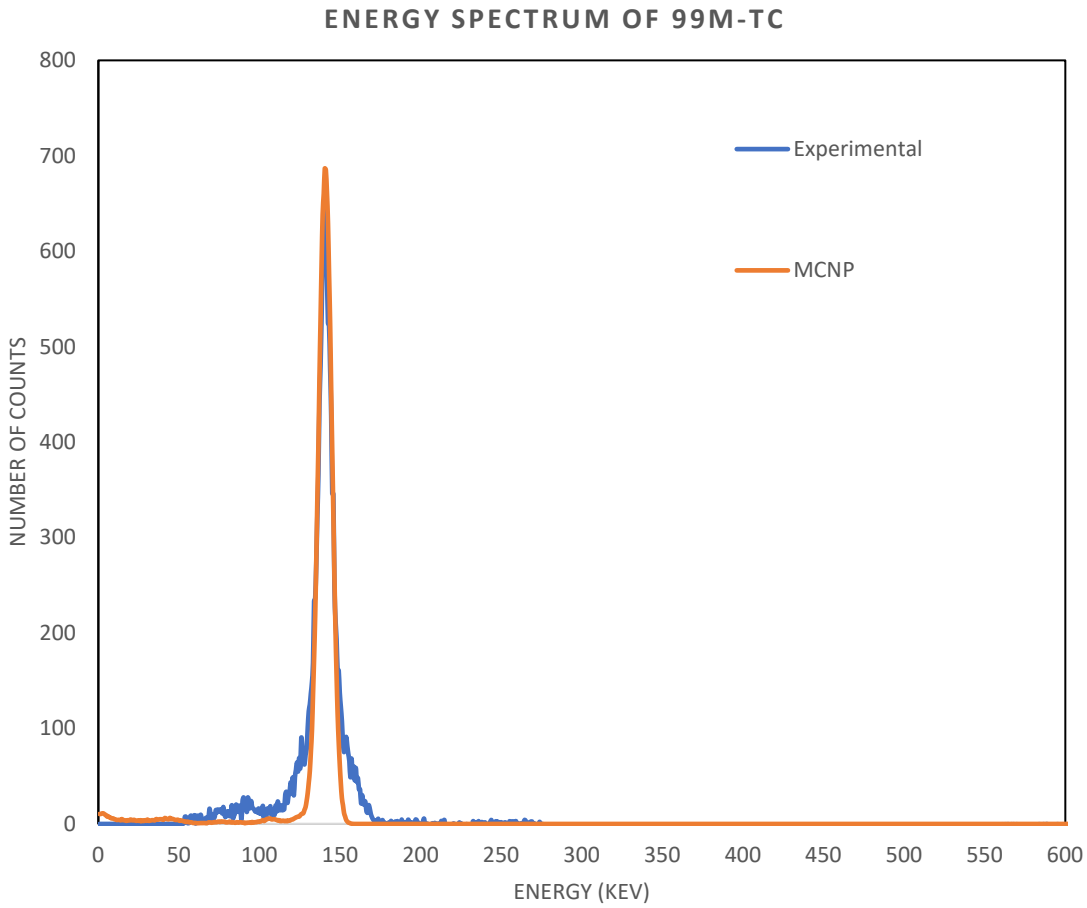

Figure 6.7 The plot of the energy spectrum of the ^{99m}Tc source acquired in the experiments and MCNP.

ii. Sensitivity and Spatial Resolution Simulations

Table 6.2 shows the sensitivity and spatial resolution values of the detector with associated model paramers.

SCD (cm)	t1 (mm)	t2 (mm)	d1 (mm)	d2 (mm)	x1 (mm)	x2 (mm)	Spatial Resolution (mm)	Sensitivity (cps/MBq)
10	1.8	1.8	2	2	0	65	4.5	8.91
10	1.8	1.8	2	2	0	45	5.6	11.25
`10	1.8	1.8	2	2	0	35	6.5	12.84
`10	1.8	1.8	2	2	0	15	10.9	17.42
`10	1.8	1.8	2	2	0	0	52.5	22.65
`10	1.8	1.8	2	2	15	65	5	8.75
10	1.8	1.8	2	2	25	65	4.8	8.72
10	1.8	1.8	2	2	45	65	5	8.65
10	1.8	1.8	2	2	15	50	5.5	10.65
10	1.8	1.8	2	2	25	40	5.5	11.75
10	1.8	1.8	2	2	45	20	9.5	15.86
10	1.8	1.8	2	2	65	0	7.5	22.12
10	**1.5**	**1.5**	**3**	**3**	**100**	**0**	**6.9**	**48.95**

As seen in Figure 6.7, the amplitude of the photopeak and area under the photopeak are much the same for each curve. Hence, further simulations of spatial resolution and sensitivity were performed in MCNP in order to investigate if better values for each charecteristics can be obtained. Starting from the optimum geometric model parameters found in the experiments, a total of 130 additional simulation points were performed for 13 different combination of model parameters the results were tabulated in Table 6.2. Among these simulations, the combination in bold font in Table 6.2 provided the highest sensitivity and finest spatial resolution. Having

geometric model parameters of t1=1.5 mm t2=1.5 mm, d1=3 mm, d2=3mm, x1=100 mm and x2=0 mm, the collimated detector was found to have a spatial resolution of 6.94±0.67 mm and a sensitivity of 48.95±0.81 cps/MBq at 10cm SCD.

In order to compare these values to the literature, more simulations were performed in MCNP to determine the sensitivity and spatial resolution of the detector at 5 cm SCD by using the same optimum model parameters as above. At 5 cm SCD, the spatial resolution of the system was found to be 4.28±0.40 mm and 188.61±1.41 cps/MBq, respectively.

Table 6.3 shows charecteristics of some of the best intraoperative handheld gamma probes that are used for sentinel node localization. Based on the comparision of these characteristics to the values that we obtained with our detector, it can be stated that, the detector used in this study has much finer spatial resolution even at larger SCD. On the other hand, the sensitivity of the detector fell into the middle of the sensitivity values obtained with other gamma probes.

However, as discusesed earlier, the 1MBq activity detectability requirement is still satisfied.

Table 6.3 Comparision of the detector charecteristics with other probes on the market. Values obtained from [69]

Probe Type	Spatial Resolution FWHM (mm) at 3 cm	Sensitivity in Air at (cps/MBq) at 5 cm
C-Trak Omniprobe (Lechner Collimator)	19	380±60
Europrobe (Small Probe with Collimator)	22	140±20
Neoprobe with (Collimator) Used in fhSPECT system	28	390±60
Node Seeker (Straight Probe)	35	930±180
Navigator (without Collimator)	35	210±30
γ-Locator (F8 A1)	38	92±14
The collimated detector in this study	4.3 at (5cm) 6.9 at (10cm)	189±2

6.3.3. Small Detector Design

Using the collimation geometry that provided the optimum values, MCNP simulations were performed again in order to understand how much of the volume detection crystal is used. The MCNPX Visual Editor Software with the Version of X_24E was utilized to visualize the particle tracks in the MCNP simulation and Figure 6.8 was obtained.

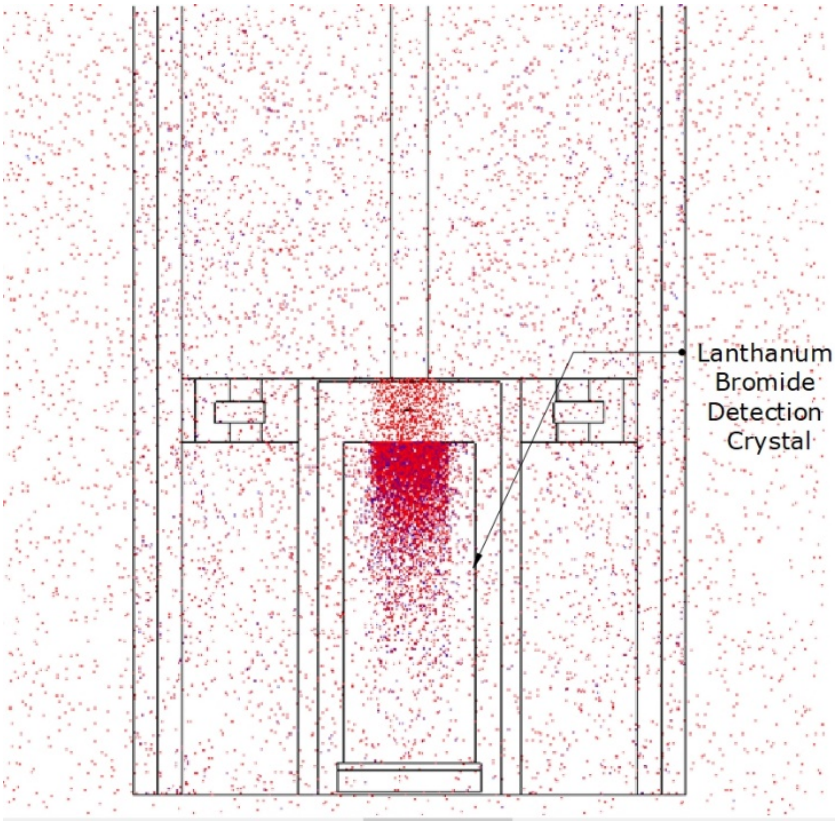

Figure 6.8 Particle tracks within the detector geometry acquired by MCNP simulations.

Red dots in Figure 6.8 represents the peak energy particles deposited within the medium. Based on the Figure 6.8, it can be summarized that with these settings, roughly one-eigth of the crystal volume is used.

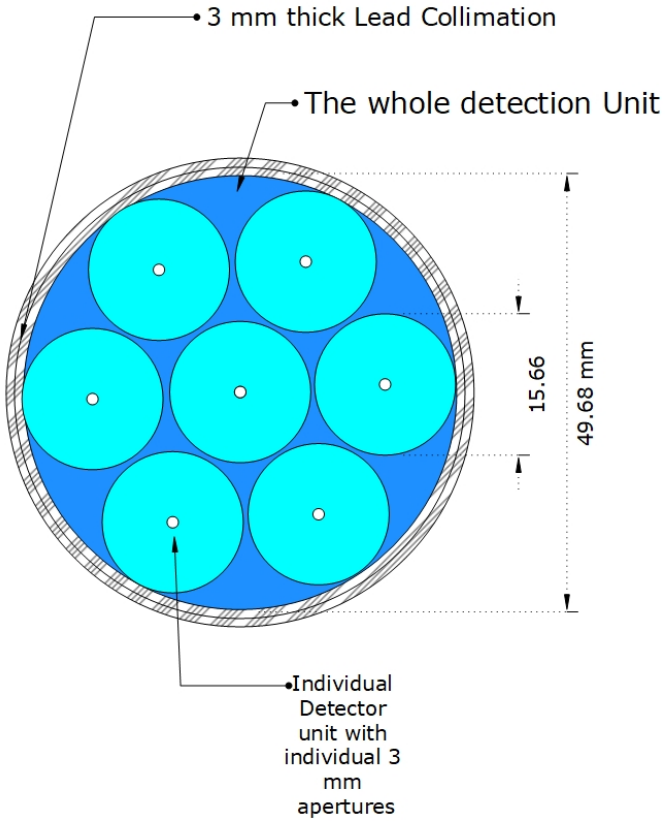

Figure 6.9 Schematic drawing of proposed detection unit with multiple detectors.

Hence, a new more compact design of the detector would allow the use of multiple detectors bundled together with each having its own collimation, as illustrated in Figure 6.9. This would enable faster acqusition and faster mapping of the radiactive distribution in real time. Another simulation in MCNP was performed with a new smaller design of the detector in which the crystal was cut to one-eight of its volume by reducing the diameter of the crystal from 10 mm to 5mm and and the thickness from 25 mm to 12.5 mm. Some portion of the aluminum shielding was cut symmetrically on each side of the crystal and the thickness of the reflector material above the cylindrical surface of the detector was reduced as shown in Figure

6.10. Figure 6.10 shows the geometries of the detector simulated in MCNP in which the two pictures are scaled and (a) and (b) show the geometry of the detector before and after redesign, respectively.

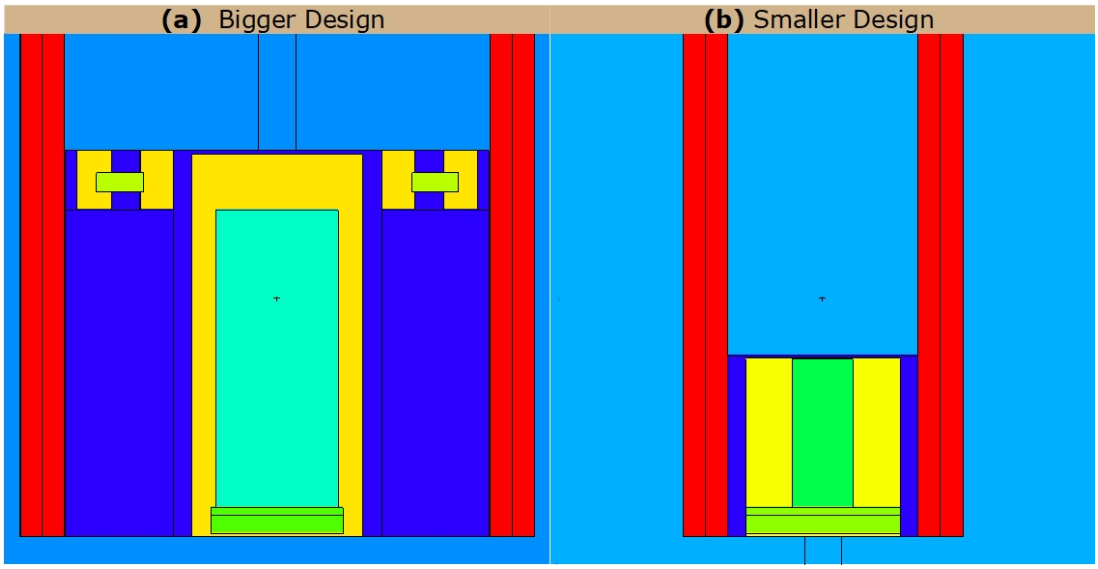

Figure 6.10 The 2D view of the detector geometry provided by MCNP simulations (a) before and (b) after minimization.

The particle track within the geometry of the new detector in Figure 6.10 (b) was simulated in MCNP and Figure 6.11 (b) was obtained in which the peak energy photons were deposited within the entire volume of the detection crystal.

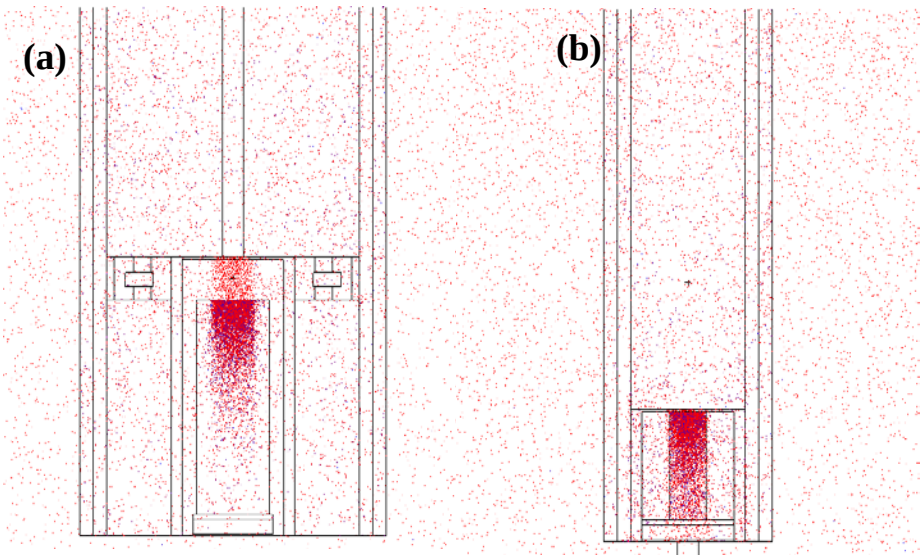

Figure 6.11 Simulation of the photon track within: (a) the geometry of the bigger detector and (b) of the smaller detector geometry.

By using the new geometry of the detector in Figure 6.11 (b), the sensitivity and spatial resolution of the detector were redifened following new MCNP simulations. The sensitivity at 10 cm SCD was slightly decreased to 37.93±0.63 (cps/MBq) from 48.95±0.72 (cps/MBq). This is because, a minority of the peak energy photons deposited at the depth of the crystal in Figure 6.11 (a) were missed in the geometry of the new design in Figure 6.11 (b) due to the reduced thickness of the crystal. The loss of sensitivity is more than compensated by using the multiple detector units. On the other hand, the spatial resolution at 10 cm was increased to 5.12±0.48 mm from 6.94±0.67 mm. The spatial resolution was improved because reducing the thickness of the reflector material above the cylindrical surface of the crystal caused a closer distance between the source and detection crystal so finer spatial resolution as a result.

6.3.4. Uncertainty of the Experimental and MCNP Results

While the total percent standard uncertainty in the sensitivity values of Table 6.1, was found to be varying between 3.4-4.9 %, the percent uncertainty in spatial resolution values of Table 6.1 varied between 3.9-5.3 %. On the other hand, the percent uncertainty in the simulated optimum sensitivity and spatial resolution at 10 cm SCD in Table 6.2 were calculated as 9.29 % and 9.55 % respectively.

6.4. Conclusion

Literature studies reveal that the localization of the deep seated lymph nodes in the body and definition of the edges of the non-palpable tumors had always been problematic which often caused re-excsion procedure of the tumor left behind. This Chapter was intended to give a contribution to the better localization of the SLNs and tumors by designing an optimum collimation geometry for the detector discussed in previous two Chapters. Based on the simulations and experimental results, it was found out that by having a spatial resolution of 4.3±0.4 mm and sensitivty of 189±1 cps/MBq at 5 cm source-to-collimator surface-distance (SCD), and 6.94±0.67 mm and 48.95±0.81 cps/MBq at 10cm SCD, the collimated detector could meet the neeeds for locating the whole of a breast tumor and the deeply-seated SLNs that requires a detector with fine spatial resolution and adequate sensitivity.

7. Conclusion and Future Directions

7.1. Conclusion

According to the results of Chapter 4, Chapter 5 and Chapter 6, where the portable gamma detector with and without collimation was designed, constructed and characterized by both experiments and simulations, the detector is capable of distinguishing between two radioisotopes having low and close photopeak energies, e.g., 141 keV and 159 keV. In addition, thanks to the collimation geometry explained in Chapter 6 that increased spatial resolution while maintaining an adequate sensitivity, the localization and identification of the clustered positive lymph nodes at depth would be possible. Furthermore, when radioactive sources such as ^{123}I with an imaging agent are used to locate the tumor, instead of placing the brachytherapy sources at the tumor site, it could be possible to provide information about the edges of the tumor. The detector was built to have a compact and mobile structure so intraoperative freehand measurements can be performed. Last but not the least, the fast measurements in real time

would be possible thanks to the proposed detector unit design as shown in Figure 6.9 of Chapter 6.

7.2. Recommended Future Directions

This work was solely focused on designing the detector hardware which can be considered as the crucial first step of the overall project. However, as explained in the Chapter 1, the ultimate goal of the overall project is to provide a real-time guidance to the surgeon by creating a 3D image of radiactivity distribution of the radioistopes used to lacate the tumor and sentinel node. Following the creation of 3D radioactivity map of the sources, the image of the radiation fields would be viewable by surgeon on a clear heads-up, augmented reality visor allowing the surgeon to view patient with the reconstructed image of tumor and nodes superimposed in the patient. However,in order to reach this goal of the overall project: a 3D tracking system should be defined and integrated to the detector to track the orientation and the position of the detector on-the-fly, a 3D image reconstruction algorithm needs to be developed and integrated to the tracked detector so the orientation and position data coming from the tracking system is combined with the measurements taken with the detector to create the 3D image of the radiation fields coming from the sources. The finally part of the system is integrating all this information into an augmented reality visor worn by the surgeon so the reconstructed image of the tumor and the nodes would be superimposed on the patient, viewable by the surgeon during the surgery. As the recommended future work, a brief explanation to each of those steps will be given below.

7.2.1. Reconstruction of the Detector

As it was proposed in Figure 6.9, the new design of the detector can be built. Having the same detector with almost same characretistics achieved but in a much more compact size would allow building multiple detectors bundled to each other, which would allow the surgeon to make rapid measurements during the surgery.

7.2.2. Integration of the 3D Tracking System

An accurate position and orientation data is required for the detector. There are several three-dimensional motion tracking techniques which provide motional data including: inertial systems, acoustic systems, optical(radio)-video systems, microwave frequency sensors, electromagnetic tracking systems and mechanically attached encoders. Among these, Inertial measurement units (IMUs) have become a promising technology by having an accelerometer, gyroscope and a magnetometer on a single chip. They are light weight, small size and low-cost units used in most of the smartphones and in virtual reality and augmented reality displays. [139] An IMU attached to our detector would give information about the orientation and position of the probe by integrating linear accelerations and angular velocities data coming from the accelerometer, gyroscope and magnetometer. The rotational and translational movements can be measured by using an IMU which comprises of gyroscopes and accelerometers. Short term movements can be easily tracked by using a background direction from the accelerometer which caused by gravity. However, using an IMU consisting of only 3 axis accelerometers and 3 axis gyroscopes is not sufficient to track the accurate position and orientation of the probe in space since small errors build up in each axis caused by the double

integration of accelerometer data to get the position information. These errors can add up to a drift in the absolute direction over time. The drift problem can be solved by using another directional sensor: a 3-axis magnetometer (compass). The sensing algorithm can compensate for small drifts for longer periods of time thanks to extra magnetic field information coming from 3-axis magnetometer. [140] Hence, the use of an IMU comprising of a 3-axis accelerometer, 3- axis gyroscope and a 3-axis magnetometer is being proposed to track the absolute change in the position and orientation of the detector in space.

7.2.3. Determination of the 3D Reconstruction Algorithm.

The preoperative imaging techniques to localize SLNs are not applicable for use during surgery because the position and anatomy of the patient during acquisition of the images is different than the position and anatomy present during the surgery. For that reason, the real-time information about the location of SLNs for breast conserving surgery is of high value. Our detector system will combine readings from a handheld radiation detector with an IMU tracking system to determine its position and the orientation in space so the three-dimensional image of radioactivity distribution of the radiotracers injected to the body can be reconstructed in real time to be used as the guidance for the surgeon during the surgery.

Based on the overall goals of this study, the handheld gamma detector will be scanned around the target to detect radiation coming from the source volume. A one-dimensional reading in count per second (cps) for each three-dimensional pose of the detector will be acquired. The reconstruction problem is transforming this one-dimensional data into a three-dimensional radioactivity distribution in a finite volume in space based on the readings of the

detector accompanied with orientation and position data from the tracking system. This reconstruction problem can be expressed by Equation 7.1:

$$g_i = \sum_{j=1}^{M} H_{ij} f_j . \qquad (7.1)$$

Assuming the projected target volume X is composing of M volume elements (voxels) each expressed as xj and j= 1, ……. M, the number of projection bins is denoted as i where i= 1, …….M and gi is the detector reading in cps at projection bin i and fj is the radioactivity to be reconstructed in voxel j (xj). Each entrie H_{ij} is called a system matrix coefficient, which includes the detector's response functions and describes the influence of radioactivity in voxel *j* to the detector reading g_i. In other words, it is the system matrix that describes radiation propagation through the volume to the detector positions. In traditional nuclear medicine imaging modalities, such as SPECT, PET, the coefficients of the system matrix can be pre-determined from the CT scan, since the relative position and orientation of the detector are fixed and do not depend on the scan. However, in our model, measurements will be taken at arbitrary, on the fly, positions. Hence, the system matrix coefficients H_{ij} should be calculated during runtime and each detector reading g_i should be accompanied with an orientation and position vector pair.

7.2.4. Augmented Reality System

The use of a heads-up, augmented reality display is the last step of this overall project. A three-dimensional image of radioactive distribution can be projected on to a head-mounted clear visor registered to the patient as the surgeon's angle of view changes. Augmented reality systems are widely used in medical applications for teaching and guidance purposes. The integration of an augmented reality system to this detector unit seems to be feasible.

Bibliography

[1] A. Assmus, "Early History of X-rays," Summer 1995. [Online]. Available: https://www.slac.stanford.edu/pubs/beamline/25/2/25-2-assmus.pdf. [Accessed 1 8 2019].

[2] Contemporary Physics Education Project (CPEP), "Radioactivity," in *Nuclear Science—A Guide to the Nuclear Science Wall Chart*, 4th ed., J. C. J. O. K. K. M. M. E. N. Howard Matis, Ed., 2018, pp. 3-6.

[3] M. Cabellero, "19-Mar-2016. [Online]. Available: http://large.stanford.edu/courses/2016/ph241/caballero2/. [Accessed: 01-Aug-2019].Marie Curie and the Discovery of Radioactivity," 2016.

[4] M. Kemerink, T. J. Dierichs, J. Dierichs, H. J. Huynen, J. E. Wildberger, J. M. A. van Engelshoven and G. J. Kemerink, "Characteristics of a First-Generation X-Ray System," *Radiology*, 2011.

[5] American Cancer Society, "Breast Cancer Facts & Figures 2017-2018," American Cancer Society, Inc, Atlanta, 2017.

[6] L. E. McCahill, R. M. Single, E. J. Aiello Bowles, H. S. Feigelson, T. A. James, T. Barney, J. M. Engel and A. A. Onitilo, "Variability in reexcision following breast conservation surgery," *JAMA - Journal of the American Medical Association*, 2012.

[7] G. A. Khuwaja and A. N. Abu-Rezq, "Bi-modal breast cancer classification system," *Pattern Analysis and Applications*, vol. 7, no. 3, pp. 235-242, 12 2004.

[8] The American Cancer Society medical and editorial content, "What Is Breast Cancer? | Breast Cancer Definition", Cancer.org, 2019. [Online]. Available: https://www.cancer.org/cancer/breast-cancer/about/what-is-breast-cancer.html. [Accessed: 11- Jul- 2019].," [Online].

[9] "M. Kosir, "Breast Cancer - Women's Health Issues - MSD Manual Consumer Version", MSD Manual Consumer Version, 2019. [Online]. Available: https://www.merckmanuals.com/home/women-s-health-issues/breast-disorders/breast-cancer. [Accessed: 12- Jul- 2019].".

[10] ""“Mastectomy,” Mayo Clinic, 18-May-2018. [Online]. Available: https://www.mayoclinic.org/tests-procedures/mastectomy/about/pac-20394670. [Accessed: 13-Jul-2019].".

[11] "UW Health. (2019). Breast-Conserving Surgery (Lumpectomy or Partial Mastectomy) for Breast Cancer | UW Health | Madison, WI. [online] Available at: https://www.uwhealth.org/health/topic/surgicaldetail/breast-conserving-surgery-lumpectomy-or-partial-mastec".

[12] A. M. Cotlar, J. J. Dubose and D. M. Rose, "History of surgery for breast cancer: Radical to the sublime," *Current Surgery*, 2003.

[13] M. Loukas, R. S. Tubbs, N. Mirzayan, M. Shirak, A. Steinberg and M. M. Shoja, "The history of mastectomy," *American Surgeon*, 2011.

[14] R. J. Gray, C. E. Cox and E. L. Dauway, "Radioguided Surgery for Non-palpable Breast Lesions: I-125 Radioactive Seed Localization," in *Radioguided Surgery: Current Applications and Innovative Directions*, N. O. P. S. Herrmann K., Ed., Springer, Cham, 2016, pp. 125-137.

[15] W. Pavlicek, H. A. Walton, P. J. Karstaedt and R. J. Gray, "Radiation Safety With Use of I-125 Seeds for Localization of Nonpalpable Breast Lesions," *Academic Radiology*, 2006.

[16] Y. E. van Riet, A. J. Maaskant, G. J. Creemers, L. J. van Warmerdam, F. H. Jansen, C. J. van de Velde, H. J. Rutten and G. A. Nieuwenhuijzen, "Identification of residual breast tumour localization after neo-adjuvant chemotherapy using a radioactive 125 Iodine seed," *European Journal of Surgical Oncology*, vol. 36, no. 2, pp. 164-169, 2 2010.

[17] R. J. Gray, B. A. Pockaj, P. J. Karstaedt and M. C. Roarke, "Radioactive seed localization of nonpalpable breast lesions is better than wire localization," *American Journal of Surgery*, 2004.

[18] R. J. Gray, C. Salud, K. Nguyen, E. Dauway, J. Friedland, C. Berman, E. Peltz, G. Whitehead and C. E. Cox, "Randomized Prospective Evaluation of a Novel Technique for Biopsy or Lumpectomy of Nonpalpable Breast Lesions: Radioactive Seed Versus Wire Localization," *Annals of Surgical Oncology*, 2001.

[19] C. E. Cox, B. Furman, N. Stowell, M. Ebert, J. Clark, E. Dupont, A. Shons, C. Berman, J. Beauchamp, M. Gardner, M. Hersch, P. Venugopal, M. Szabunio, J. Cressman, N. Diaz, V. Vrcel and R. Fairclough, *Radioactive seed localization breast biopsy and lumpectomy: Can specimen radiographs be eliminated?*, 2003.

[20] L. J. McGhan, S. C. McKeever, B. A. Pockaj, N. Wasif, M. E. Giurescu, H. A. Walton and R. J. Gray, "Radioactive seed localization for nonpalpable breast lesions: Review of 1,000 consecutive procedures at a single institution," in *Annals of Surgical Oncology*, 2011.

[21] R. P. Graham, J. W. Jakub, J. J. Brunette and C. Reynolds, "Handling of Radioactive Seed Localization Breast Specimens in the Pathology Laboratory," *The American Journal of Surgical Pathology,* 2012.

[22] B. Pouw, M. Peeters and R. Valdes Olmos, "Radioguided Surgery for Non- palpable Breast Lesions: I-125 Radio Occult Lesion Localization (ROLL)," in *Radioguided Surgery: Current Applications and Innovative Directions*, N. O. P. S. (. Herrmann K., Ed., Springer, Cham, 2016, pp. 139-148.

[23] R. A. Audisio, R. Nadeem, O. Harris, S. Desmond, R. Thind and L. S. Chagla, "Radioguided occult lesion localisation (ROLL) is available in the UK for impalpable breast lesions," *Annals of the Royal College of Surgeons of England*, 2005.

[24] J. Kim, D. Chung and A. Spillane, "Combined radioguided occult lession and sentinel node localization for breast cancer," *ANZ Journal of Surgery,* 2004.

[25] M. C. Van Rijk, P. J. Tanis, O. E. Nieweg, C. E. Loo, R. A. Olmos, H. S. Oldenburg, E. J. Rutgers, C. A. Hoefnagel and B. B. Kroon, "Sentinel node biopsy and concomitant probe-guided tumor excision of nonpalpable breast cancer," *Annals of Surgical Oncology*, 2007.

[26] C. De Cicco, M. Pizzamiglio, G. Trifirò, A. Luini, M. Ferrari, G. Prisco, V. Galimberti, E. Cassano, G. Viale, M. Intra, P. Veronesi and G. Paganelli, "Radioguided occult lesion localisation (ROLL) and surgical biopsy in breast cancer. Technical aspects.," *The quarterly journal of nuclear medicine : official publication of the Italian Association of Nuclear Medicine (AIMN) [and] the International Association of Radiopharmacology (IAR),* 2002.

[27] C. De Cicco, G. Trifirò, M. Intra, G. Marotta, A. Ciprian, A. Frasson, G. Prisco, A. Luini, G. Viale and G. Paganelli, "Optimised nuclear medicine method for tumour marking and sentinel node detection in occult primary breast lesions," *European Journal of Nuclear Medicine and Molecular Imaging*, 2004.

[28] D. Sarlos, L. D. Frey, H. Haueisen, G. Landmann, L. A. Kots and G. Schaer, "Radioguided occult lesion localization (ROLL) for treatment and diagnosis of malignant and premalignant breast lesions combined with sentinel node biopsy: A prospective clinical trial with 100 patients," *European Journal of Surgical Oncology*, 2009.

[29] V. Lavoué, C. Nos, K. B. Clough, F. Baghaie, E. Zerbib, B. Poulet, M. A. Lefrère Belda, A. Ducellier and F. Lecuru, "Simplified technique of radioguided occult lesion localization (ROLL) plus sentinel lymph node biopsy (SNOLL) in breast carcinoma," *Annals of Surgical Oncology*, 2008.

[30] S. Monti, V. Galimberti, G. Trifiro, C. DeCicco, N. Peradze, F. Brenelli, J. Fernandez-Rodriguez, N. Rotmensz, A. Latronico, A. Berrettini, M. Mauri, L. Machado, A. Luini and G. Paganelli, "Occult breast lesion localization plus sentinel node biopsy (SNOLL): Experience with 959 patients at the European Institute of Oncology," *Annals of Surgical Oncology,* 2007.

[31] I. M. Van Der Ploeg, O. E. Nieweg, B. B. Kroon, E. J. Rutgers, M. J. T. Baas-Vrancken Peeters, W. V. Vogel, C. A. Hoefnagel and R. A. Valdés Olmos, "The yield of SPECT/CT for anatomical lymphatic mapping in patients with breast cancer," *European Journal of Nuclear Medicine and Molecular Imaging,* 2009.

[32] C. H. Barrio A.V., "Radioguided Sentinel Lymph Node Mapping and Biopsy in Breast Cancer," in *Radioguided Surgery: Current Applications and Innovative Directions*, N. O. P. S. Herrmann K., Ed., Springer, Cham, pp. 115-123.

[33] R. C. Martin, M. J. Edwards, S. L. Wong, T. M. Tuttle, D. J. Carlson, C. M. Brown, R. D. Noyes, R. L. Glaser, D. J. Vennekotter, P. S. Turk, P. S. Tate, A. Sardi, P. B. Cerrito and K. M. McMasters, "Practical guidelines for optimal gamma probe detection of sentinel lymph nodes in breast cancer: Results of a multi-institutional study," *Surgery,* 2000.

[34] D. C. Linehan, A. D. Hill, K. N. Tran, H. Yeung, S. D. Yeh, P. I. Borgen and H. S. Cody, "Sentinel lymph node biopsy in breast cancer: unfiltered radioisotope is superior to filtered11No competing interests declared.," *Journal of the American College of Surgeons*, 2002.

[35] P. J. Tanis, "UvA-DARE (Digital Academic Repository) Methodology and implications of lymphatic mapping and sentinel lymphadenectomy".

[36] M. D. McCarter, H. Yeung, S. Yeh, J. Fey, P. I. Borgen and H. S. Cody, "Localization of the sentinel node in breast cancer: Identical results with same-day and day-before isotope injection," *Annals of Surgical Oncology,* 2001.

[37] R. C. Martin, A. M. Derossis, J. Fey, H. Yeung, S. D. Yeh, T. Akhurst, A. S. Heerdt, J. Petrek, K. J. VanZee, L. L. Montgomery, P. I. Borgen and H. S. Cody, "Intradermal isotope injection is superior to intramammary in sentinel node biopsy for breast cancer," *Surgery,* 2001.

[38] T. Kim, A. E. Giuliano and G. H. Lyman, *Lymphatic mapping and sentinel lymph node biopsy in early-stage breast carcinoma: A metaanalysis,* 2006.

[39] R. C. Martin, J. Fey, H. Yeung, P. I. Borgen and H. S. Cody, "Highest isotope count does not predict sentinel node positivity in all breast cancer patients," *Annals of Surgical Oncology*, 2001.

[40] K. M. McMasters, D. S. Reintgen, M. I. Ross, S. L. Wong, J. E. Gershenwald, D. N. Krag, R. D. Noyes, V. Viar, P. B. Cerrito and M. J. Edwards, "Sentinel lymph node biopsy for melanoma: How many radioactive nodes should be removed?," *Annals of Surgical Oncology*, 2001.

[41] T. Wendler, U. Eberlein and M. Lassmann, "Physics of Radioguided Surgery: Basic Principles and Methods of Radiation Detection," in *Radioguided Surgery: Current Applications and Innovative Directions*, O. E. N. a. S. P. P. K. Hermann, Ed., Springer-Cham, 2016, pp. 15-33.

[42] H. L. Byrne, Y. Gholami and Z. Kuncic, "Impact of fluorescence emission from gold atoms on surrounding biological tissue - Implications for nanoparticle radio-enhancement," *Physics in Medicine and Biology*, 2017.

[43] C. Broyles, A. Thomas and S. Haynes, "Phys Rev., 89,715," 1953.

[44] S. R. Cherry, J. A. Sorenson and M. E. Phelps, Physics in nuclear medicine, Elsevier/Saunders, 2012, p. 523.

[45] F. A. Scannavino and P. E. Cruvinel, "A graphical tool for an analytical approach of scattering photons by the Compton effect," *Nuclear Instruments and Methods in Physics Research, Section A: Accelerators, Spectrometers, Detectors and Associated Equipment*, 2012.

[46] "U. F. O. Themes,“Basic Radiation Protection and Radiobiology,” Radiology Key, 02-Jan-2017," [Online]. Available: https://radiologykey.com/basic-radiation-protection-and-radiobiology-2/. [Accessed: 22-Jul-2019].

[47] R. D. Evans, The Atomic Nucleus, New Delhi: McGraw-Hill Book Company, 1955.

[48] S. W. Herbert Bardach, "The Evolution of a Radiological Measuring Technique," in *Innovative Metrology -Key to Progress*, Columbus, Ohio, 1970.

[49] L. Katz and A. S. Penfold, "Range-energy relations for electrons and the determination of beta-ray end-point energies by absorption," *Reviews of Modern Physics*, 1952.

[50] C. B. Hruska and M. K. O'Connor, "Quantification of lesion size, depth, and uptake using a dual-head molecular breast imaging system," *Medical Physics*, 2008.

[51] C. Gajdos, P. Ian Tartter, I. J. Bleiweiss, G. Hermann, J. De Csepel, A. Estabrook and A. W. Rademaker, "Mammographic appearance of nonpalpable breast cancer reflects pathologic characteristics," *Annals of Surgery*, 2002.

[52] L. Fortunato, R. Penteriani, M. Farina, C. E. Vitelli and F. R. Piro, "Intraoperative ultrasound is an effective and preferable technique to localize non-palpable breast tumors," *European Journal of Surgical Oncology*, 2008.

[53] W. A. Waddington, M. R. Keshtgar, I. Taylor, S. R. Lakhani, M. D. Short and P. J. Eli, "Radiation safety of the sentinel lymph node technique in breast cancer," *European Journal of Nuclear Medicine*, 2000.

[54] T. Engelen, B. M. Winkel, D. D. Rietbergen, G. H. Kleinjan, S. Vidal-Sicart, R. A. V. Olmos, N. S. Van Den Berg and F. Wb Van Leeuwen, "The next evolution in radioguided surgery: breast cancer related sentinel node localization using a freehandSPECT-mobile gamma camera combination," 2015.

[55] G. Mariani, P. Erba, G. Villa, M. Gipponi, G. Manca, G. Boni, F. Buffoni, F. Castagnola, G. Paganelli and H. W. Strauss, *Lymphoscintigraphic and Intraoperative Detection of the Sentinel Lymph Node in Breast Cancer Patients: The Nuclear Medicine Perspective*, vol. 85, 2004, pp. 112-122.

[56] G. C. Bentel, L. B. Marks, P. H. Hardenbergh and L. R. Prosnitz, "Variability of the depth of supraclavicular and axillary lymph nodes in patients with breast cancer: Is a posterior axillary boost field necessary?," *International Journal of Radiation Oncology Biology Physics*, 2000.

[57] S. Povoski, "The History of Radioguided Surgery: Early Historical Milestones and the Development of Later Innovative Clinical Applications," in *Radioguided Surgery: Current Applications and Innovative Directions*, N. O. P. S. Herrmann K., Ed., Springer, Cham, 2016, pp. 3-12.

[58] S. R. Povoski, R. L. Neff, C. M. Mojzisik, D. M. O'Malley, G. H. Hinkle, N. C. Hall, D. A. Murrey, M. V. Knopp and E. W. Martin, *A comprehensive overview of radioguided surgery using gamma detection probe technology*, 2009.

[59] E. A. Gould, T. Winship, P. H. Philbin and H. H. Kerr, "Observations on a “sentinel node” in cancer of the parotid," *Cancer*, 1960.

[60] R. M. Cabanas, "An approach for the treatment of penile carcinoma," *Cancer*, 1977.

[61] J. C. Alex, D. L. Weaver, J. T. Fairbank, B. S. Rankin and D. N. Krag, "Gamma-probe-guided lymph node localization in malignant melanoma," *Surgical Oncology*, 1993.

[62] D. N. Krag, D. L. Weaver, J. C. Alex and J. T. Fairbank, "Surgical resection and radiolocalization of the sentinel lymph node in breast cancer using a gamma probe," *Surgical Oncology,* 1993.

[63] C. E. Cox, M. Hyacinthe, C. Berman and A. Wagner, "Localization of an occult primary breast cancer with technetium-99m sestamibi scan and an intraoperative gamma probe," *Cancer Control,* 1996.

[64] A. Luini, S. Zurrida, P. Paganelli, V. Galimberti, V. Sacchini, S. Monti, P. Veronesi, G. Viale and U. Veronesi, "Comparison of radioguided excision with wire localization of occult breast lesions," *British Journal of Surgery,* 1999.

[65] R. Gennari, V. Galimberti, C. De Cicco, S. Zurrida, F. Zerwes, F. Pigatto, A. Luini, G. Paganelli and U. Veronesi, "Use of technetium-99m-labeled colloid albumin for preoperative and intraoperative localization of nonpalpable breast lesions," *Journal of the American College of Surgeons,* 2000.

[66] E. Dauway, R. Sanders, F. J. C. Berman, N. Ku, D. Reintgen, T. Yeatman, R. Falcone, S. Crawford and C. Cox, "Innovative diagnostics for breast cancer: new frontiers for the new millennium using radioactive seed localization," *Surg Forum.,* no. 9, pp. 5--348, 1999.

[67] R. J. Gray, R. Giuliano, E. L. Dauway, C. E. Cox and D. S. Reintgen, "Radioguidance for nonpalpable primary lesions and sentinel lymph node(s)," *American Journal of Surgery,* 2001.

[68] D. Hellingman and S. Vidal-Sicart, "The Use of Intraoperative Small and Large Field of View Gamma Cameras for Radioguided Surgery," in *Radioguided Surgery*, N. O. P. S. Herrmann K., Ed., Springer Cham, 2016, pp. 35-56.

[69] M. Zamburlinia, K. Keymeulen, M. Bemelmans, B. Bransa and G. J. Kemerinka, "Comparison of sentinel gamma probes for 99mTc breast cancer surgery based on NEMA NU3-2004 standard," *Nuclear Medicine Communications,* 2009.

[70] T. Tiourina, B. Arenas, D. Huysmans, H. Rutten, B. Lemaire and S. Muller, "Evaluation of surgical gamma probes for radioguided sentinel node localisation," *European Journal of Nuclear Medicine,* 1998.

[71] P. Zanzonico and S. Heller, "The intraoperative gamma probe: basic principles and choices available.," *Seminars in nuclear medicine,* vol. 30, no. 1, pp. 33-48, 1 2000.

[72] H. Wengenmair and J. Kopp, "Gamma Probes for Sentinel Lymph Node Localization: Quality Criteria, Minimal Requirements and Quality of Commercially Available Systems".

[73] G. Mariani, A. Vaiano, O. Nibale and D. Rubello, "Is the "ideal" gamma-probe for intraoperative radioguided surgery conceivable?," *Journal of nuclear medicine : official publication, Society of Nuclear Medicine,* vol. 46, no. 3, pp. 388-90, 3 2005.

[74] I. Sarikaya, A. Sarikaya and R. C. Reba, *Gamma probes and their use in tumor detection in colorectal cancer,* 2008.

[75] S. Kaviani, N. Zeraatkar, S. Sajedi, N. Gorjizadeh, M. H. Farahani, P. Ghafarian, G. E. Fakhri, H. Sabet and M. R. Ay, "Development and characterization of a compact hand-held gamma probe system, SURGEOGUIDE, based on NEMA NU3-2004 standards," *Journal of Instrumentation,* 2016.

[76] C. W. E. Van Eijk, "REVIEW To cite this article: Carel W E van Eijk," 2002.

[77] C. W. Van Eijk, P. Dorenbos, E. V. Van Loef, K. Krämer and H. U. Güdel, "Energy resolution of some new inorganic-scintillator gamma-ray detectors," *Radiation Measurements,* 2001.

[78] C. W. Van Eijk, "Inorganic-scintillator development," *Nuclear Instruments and Methods in Physics Research, Section A: Accelerators, Spectrometers, Detectors and Associated Equipment,* 2001.

[79] P. Dorenbos, J. T. de Haas and C. W. van Eijk, "Non-Proportionality in the Scintillation Response and the Energy Resolution Obtainable with Scintillation Crystals," *IEEE Transactions on Nuclear Science,* 1995.

[80] N. Garnier, A. Christophe & Belsky, C. drini, J. Moy, H. Wieczorek, P. Chevallier and A. Firsov, "Spectroscopy of CsI(Tl) layers.," 2000.

[81] A. Syntfeld, R. Arlt, V. Gostilo, A. Loupilov, M. Moszyński, A. Nassalski, M. Swoboda and D. Wolski, "Comparison of a LaBr3(Ce) scintillation detector with a large volume CdZnTe detector," in *IEEE Transactions on Nuclear Science,* 2006.

[82] D. Alexiev, L. Mo, D. Prokopovich, M. Smith and M. Matuchova, "Comparison ofLaBr3:CeandLaCl3:CeWith NaI(Tl) and Cadmium Zinc Telluride (CZT) Detectors," *IEEE Transactions on Nuclear Science,* vol. 55, no. 3, pp. 1174-1177, June 2008.

[83] T. Alharbi, "Energy resolution improvement of CdTe detectors by using the principal component analysis technique," *Nuclear Instruments and Methods in Physics Research, Section A: Accelerators, Spectrometers, Detectors and Associated Equipment,* 2018.

[84] C. Bluemel, P. Matthies, K. Herrmann and S. P. Povoski, *3D scintigraphic imaging and navigation in radioguided surgery: Freehand SPECT technology and its clinical applications,* 2016.

[85] S. Vidal-Sicart, M. E. Rioja, P. Paredes, M. R. Keshtgar and R. A. Valdés Olmos, "Contribution of perioperative imaging to radioguided surgery.," *The quarterly journal of nuclear medicine and molecular imaging : official publication of the Italian Association of Nuclear Medicine (AIMN) [and] the International Association of Radiopharmacology (IAR), [and] Section of the Society of...,* vol. 58, no. 2, pp. 140-60, 6 2014.

[86] S. Heller and P. Zanzonico, *Nuclear probes and intraoperative gamma cameras,* 2011.

[87] N. C. Hall, S. D. Nichols, S. P. Povoski, I. A. O. James, C. L. Wright, R. Harris, C. R. Schmidt, P. Muscarella, N. Latchana, E. W. Martin and E. C. Ellison, "Intraoperative Use of a Portable Large Field of View Gamma Camera and Handheld Gamma Detection Probe for Radioguided Localization and Prediction of Complete Surgical Resection of Gastrinoma: Proof of Concept.," *Journal of the American College of Surgeons,* vol. 221, no. 2, pp. 300-8, 8 2015.

[88] S. Vidal-Sicart, L. Vermeeren, O. Solà, P. Paredes and R. A. Valdés-Olmos, "The use of a portable gamma camera for preoperative lymphatic mapping: a comparison with a conventional gamma camera.," *European journal of nuclear medicine and molecular imaging,* vol. 38, no. 4, pp. 636-41, 4 2011.

[89] M. Tsuchimochi and K. Hayama, *Intraoperative gamma cameras for radioguided surgery: Technical characteristics, performance parameters, and clinical applications,* 2013.

[90] T. Wendler, M. Feuerstein, J. Traub, T. Lasser, J. Vogel, F. Daghighian, S. I. Ziegler and N. Navab, "Real-Time Fusion of Ultrasound and Gamma Probe for Navigated Localization of Liver Metastases," 2007.

[91] T. Wendler, A. Hartl, T. Lasser, J. Traub, F. Daghighian, S. I. Ziegler and N. Navab, "Towards Intra-operative 3D Nuclear Imaging: Reconstruction of 3D Radioactive Distributions Using Tracked Gamma Probes," 2007.

[92] T. Wendler, K. Herrmann, A. Schnelzer, T. Lasser, J. Traub, O. Kutter, A. Ehlerding, K. Scheidhauer, T. Schuster, M. Kiechle, M. Schwaiger, N. Navab, S. I. Ziegler and A. K. Buck, "First demonstration of 3-D lymphatic mapping in breast cancer using freehand SPECT.," *European Journal of Nuclear Medicine and Molecular Imaging,* 2010.

[93] R. A. Valdés Olmos, S. Vidal-Sicart and O. E. Nieweg, *Technological innovation in the sentinel node procedure: Towards 3-D intraoperative imaging,* 2010.

[94] "declipse®SPECT; SurgicEye Munich Germany (cited 2019 August 04)," Available from: http://www.surgiceye.com/m/declipseSPECT/, Munich Germany.

[95] B. Pouw, L. J. W. v. der Veen, D. Hellingman, O. R. Brouwer, M. J. T. V. Peeters, M. P. Stokkel and R. A. Olmos, "Feasibility of preoperative 125I seed-guided tumoural tracer injection using freehand SPECT for sentinel lymph node mapping in non-palpable breast cancer," *EJNMMI Research,* 2014.

[96] M. Freesmeyer, T. Opfermann and T. Winkens, "Hybrid integration of real-time US and freehand SPECT: proof of concept in patients with thyroid diseases.," *Radiology,* vol. 271, no. 3, pp. 856-61, 6 2014.

[97] B. Pouw, *Integrating new imaging modalities in breast cancer management.,* Amsterdam: PhD Thesis University of Amsterdam, 2016.

[98] P. Matthies, K. Sharma, A. Okur, J. Gardiazabal, J. Vogel, T. Lasser and N. Navab, "First use of mini gamma cameras for intra-operative robotic SPECT reconstruction," in *Lecture Notes in Computer Science (including subseries Lecture Notes in Artificial Intelligence and Lecture Notes in Bioinformatics)*, 2013.

[99] M. Thill and K. Baumann, *New technologies in breast cancer surgery,* 2012.

[100] B. Pouw, L. J. De Wit-Van Der Veen, F. Van Duijnhoven, E. J. Rutgers, M. P. Stokkel, R. A. Valdés Olmos and M. J. T. Vrancken Peeters, "Intraoperative 3D navigation for single or multiple125I-seed localization in breast-preserving cancer surgery," *Clinical Nuclear Medicine,* 2016.

[101] B. Fisher, S. Anderson, J. Bryant, R. G. Margolese, M. Deutsch, E. R. Fisher, J.-H. Jeong and N. Wolmark, "Twenty-Year Follow-up of a Randomized Trial Comparing Total Mastectomy, Lumpectomy, and Lumpectomy plus Irradiation for the Treatment of Invasive Breast Cancer," *New England Journal of Medicine,* vol. 347, no. 16, pp. 1233-1241, 17 10 2002.

[102] M. Barry and M. R. Kell, *Radiotherapy and breast reconstruction: A meta-analysis,* vol. 127, 2011, pp. 15-22.

[103] D. Sharek, M. L. Zuley, J. Y. Zhang, A. Soran, G. M. Ahrendt and M. A. Ganott, "Radioactive seed localization versus wire localization for lumpectomies: A comparison of outcomes," *American Journal of Roentgenology,* 2015.

[104] J. P. Weichert, P. A. Clark, I. K. Kandela, A. M. Vaccaro, W. Clarke, M. A. Longino, A. N. Pinchuk, M. Farhoud, K. I. Swanson, J. M. Floberg, J. Grudzinski, B. Titz, A. M. Traynor, H. E. Chen, L. T. Hall, C. J. Pazoles, P. J. Pickhardt and J. S. Kuo, "Alkylphosphocholine analogs for broad-spectrum cancer imaging and therapy," *Science Translational Medicine,* 2014.

[105] Karlsruhe Nuclide Chart 8th Edition, " Decay Schemes - NucleonicaWiki. [Online]. Available: http://www.nucleonica1.com/wiki/index.php?title=Decay_Schemes. [Accessed: 10-Aug-2019].," © European Union, 1995-2019, 2012.

[106] M. B. Chadwick, M. Herman, P. Obložinský, M. E. Dunn, Y. Danon, A. C. Kahler, D. L. Smith, B. Pritychenko, G. Arbanas, R. Arcilla, R. Brewer, D. A. Brown, R. Capote, A. D. Carlson, Y. S. Cho, H. Derrien, K. Guber, G. M. Hale, S. Hoblit, S. Holloway, T. D. Johnson, T. Kawano, B. C. Kiedrowski, H. Kim, S. Kunieda, N. M. Larson, L. Leal, J. P. Lestone, R. C. Little, E. A. McCutchan, R. E. MacFarlane, M. MacInnes, C. M. Mattoon, R. D. McKnight, S. F. Mughabghab, G. P. Nobre, G. Palmiotti, A. Palumbo, M. T. Pigni, V. G. Pronyaev, R. O. Sayer, A. A. Sonzogni, N. C. Summers, P. Talou, I. J. Thompson, A. Trkov, R. L. Vogt, S. C. van der Marck, A. Wallner, M. C. White, D. Wiarda and P. G. Young, "ENDF/B-VII.1 nuclear data for science and technology: Cross sections, covariances, fission product yields and decay data," *Nuclear Data Sheets,* 2011.

[107] "Hpschapters.org. (2019). Nuclide Safety Data Sheet Iodine-123. [online] Available at: http://www.hpschapters.org/northcarolina/NSDS/123IPDF.pdf [Accessed 10 Aug. 2019].".

[108] LNHB-KRI/C.Morillon, M.M.Be, V.Chechev, A.Egorov, "LNE-LNHB/CEA-Table de Radionucleides 99m-Tc," LNE-LNHB/CEA, 2004.

[109] T. Watanabe, I. Kimijima, T. Ohtake, A. Tsuchiya, F. Shishido and S. Takenoshita, "Sentinel node biopsy with technetium-99m colloidal rhenium sulphide in patients with breast cancer," *British Journal of Surgery,* 2001.

[110] R. Pani, R. Pellegrini, M. N. Cinti, M. Longo, R. Donnarumma, A. D'Alessio, C. Borrazzo, A. Pergola, S. Ridolfi and G. De Vincentis, "Development of a novel gamma probe for detecting radiation direction," in *Journal of Instrumentation,* 2016.

[111] E. M. Becker and A. T. Farsoni, "Wireless, low-cost, FPGA-based miniature gamma ray spectrometer," *Nuclear Instruments and Methods in Physics Research, Section A: Accelerators, Spectrometers, Detectors and Associated Equipment,* 2014.

[112] L. J. Mitchell and B. Phlips, "Characterization of strontium iodide scintillators with silicon photomultipliers," *Nuclear Instruments and Methods in Physics Research, Section A: Accelerators, Spectrometers, Detectors and Associated Equipment,* 2016.

[113] E. V. Van Loef, C. M. Wilson, N. J. Cherepy, G. Hull, S. A. Payne, W. S. Choong, W. W. Moses and K. S. Shah, "Crystal growth and scintillation properties of strontium iodide scintillators," *IEEE Transactions on Nuclear Science,* 2009.

[114] E. I. Prosper, O. J. Abebe and U. J. Ogri, "Characterisation of Cerium-Doped Lanthanum Bromide scintillation detector," *Am. J. Phys. Educ,* vol. 6, no. 1, p. 162, 2012.

[115] M. A. Saizu and G. Cata-Danil, "LANTHANUM BROMIDE SCINTILLATION DETECTOR FOR GAMMA SPECTROMETRY APPLIED IN INTERNAL RADIOACTIVE CONTAMINATION MEASUREMENTS," *U.P.B. Sci. Bull., Series A,* vol. 73, 2011.

[116] "Brillance™ Scintillators Performance Summary," Saint Gobain Crystals and Detectors, Newberry, OH, USA, 2009.

[117] ©2004-2016 Saint-Gobain Ceramics & Plastics, "Brillance®380 Scintillation Material," Saint Gobain Crystals and Detectors, Newberry, OH, USA , 2009.

[118] F. G. Quarati, I. V. Khodyuk, C. W. Van Eijk, P. Quarati and P. Dorenbos, "Study of 138La radioactive decays using LaBr 3 scintillators," *Nuclear Instruments and Methods in Physics Research, Section A: Accelerators, Spectrometers, Detectors and Associated Equipment,* 2012.

[119] D. Alexiev, L. Mo, D. A. Prokopovich, M. L. Smith and M. Matuchova, "Comparison of LaBr 3 : Ce and LaCl 3 : Ce with NaI(T1) and Cadmium Zinc Telluride (CZT) detectors," in *IEEE Transactions on Nuclear Science*, 2008.

[120] B. Bearden, H. C. C. Lu, T. A. Carlson, F. B. Malik, T. C. Tucker, C. W. Nestor, J. A. Bearden and A. F. Burr, "Atomic Binding Energies for Each Subshell for Elements Z = 1-106," 1967.

[121] M. Berger, J. Coursey, M. Zucker and J. and Chang, "ESTAR, PSTAR, and ASTAR: Computer Programs for Calculating Stopping-Power and Range Tables for Electrons, Protons, and Helium Ions (version 1.2.3).," National Institute of Standards and Technology, Gaithersburg, MD., 2005.

[122] U. E. M. L. T. Wendler, "Physics of Radioguided Surgery: Basic Principles and Methods of Radiation Detection," in *Radioguided Surgery:*

Current Applications and Innovative Directions, O. E. N. a. S. P. P. K. Hermann, Ed., Springer-Cham, 2016, pp. 15-33.

[123] First Sensor, "Introduction to silicon photomultipliers (SiPMs)," First Sensor Available Online at https://www.first-sensor.com/cms/upload/appnotes/AN_SiPM_Introduction_E.pdf, Berlin-Oberschöneweide, Version 03-12-15.

[124] Slamowir Piatek, "Physics and operation of the MPPC silicon photomultiplier," Hamamatsu Corporation & New Jersey Institute of Technology, New Jersey, 2014.

[125] A. Osovizky, D. Ginzburg, I. Cohen-Zada, M. Ghelman, E. Marcus, E. Vulasky, A. Manor, N. Ankry, V. Pushkarsky, M. Lefevre, Y. Kadmon and Y. Cohen, "New radiation sensor embedded in a metal detection unit," *IEEE Transactions on Nuclear Science,* vol. 57, no. 5 PART 2, pp. 2758-2761, 10 2010.

[126] B. Sanaei, M. T. Baei and S. Z. Sayyed-Alangi, "Characterization of a New Silicon Photomultip-lier in Comparison with a Conventional Photomultiplier Tube," *Journal of Modern Physics,* vol. 6, pp. 425-433, 2015.

[127] sensL, "J-Series High PDE and Timing Resolution, TSV Package Date Sheet," SensL © Available online from https://sensl.com/downloads/ds/DS-MicroJseries.pdf, 2017.

[128] K. E. Mesick, L. C. Stonehill, J. T. Morrell and D. D. S. Coupland, "Performance of Several Solid State Photomultipliers with CLYC Scintillator".

[129] © Semiconductor Components Industries, LLC, "ArrayJ Series Silicon Photomultiplier (SiPM) High Fill-Factor Arrays," © Semiconductor Components Industries, LLC, Aurora, Colorado, 2018.

[130] Saint-Gobain Crystals, Scintillation Products, "SGC WP Performance Summary: BrilLanCe Scintillators," Saint-Gobain Ceramics & Plastics, Hiram,Ohio, ©2006-16.

[131] M. M. Bé, V. Chisté, C. Dulieu, M. A. Kellett, X. Mougeot, A. Arinc, V. P. Chechev, N. Kuzmenko, T. Kibedi, A. Luca and A. Nichols, Table of Radionuclides (Vol. 8 – A = 41 to 198), vol. 8, 2016.

[132] G. F. Knoll, "General Properties of Radiaition Detectors," in *Radiation Detection and Measurement*, New Delhi, John Wiley & Sons, Inc, 2000, pp. 103-128.

[133] I. Mouhti, A. Elanique, M. Messous, B. Belhorma and A. Benahmed, " Validation of a NaI(Tl) and LaBr 3 (Ce) detector's models via measurements and

Monte Carlo simulations," *Journal of Radiation Research and Applied Sciences*, vol. 11, no. 4, pp. 335-339, 10 2018.

[134] Eckert&Zigler Isotope Products, "Certification of Calibration Multinuclide Standard Source," Valencia, California, 2012.

[135] D. Pelowitz, "MCNPX User's Manual. Version 2.7.0, Los Alamos National Laboratory, LA-CP-11-00438.".

[136] R. J. Mcconn, C. J. Gesh, R. T. Pagh and R. A. Rucker, "Radiation Portal Monitor Project: Compendium of Material Composition Data for Radiation Transport Modeling," 2011.

[137] C. W. E. v. Eijk, "Inorganic scintillators in medical imaging," *Physics in Medicine and Biology*, 2002.

[138] M. J. Berger and S. M. Seltzer, "Response functions for sodium iodide scintillation detectors," *Nuclear Instruments and Methods*, vol. 104, no. 2, pp. 317-332, 15 10 1972.

[139] Y. Shen, K. S. Tseng and F. Wu, "A motion tracking and inertial measurement unit-distance sensor fusion module for medical simulation," *Journal of Medical Devices, Transactions of the ASME*, vol. 10, no. 2, 1 6 2016.

[140] K. D. Oberlander, "Inertial Measurement Unit (IMU) Technology. Inverse Kinematics: Joint Considerations and the Maths for Deriving Anatomical Angles," 2015.

[141] M. Lautner, H. Lin, Y. Shen, C. Parker, H. Kuerer, S. Shaitelman, G. Babiera and I. Bedrosian, "Disparities in the use of breast-conserving therapy among patients with early-stage breast cancer," *JAMA Surgery*, 2015.

[142] Y. V. Riet, A. Maaskant, G. C. -. E. J. o. … and u. 2010, "Identification of residual breast tumour localization after neo-adjuvant chemotherapy using a radioactive 125 Iodine seed," *Elsevier*.

[143] C. Mathelin, S. Salvador, V. Bekaert, S. Croce, N. Andriamisandratsoa, P. Liégeois, E. Prados, J. L. Guyonnet, D. Grucker and D. Brasse, "A new intraoperative gamma camera for the sentinel lymph node procedure in breast cancer," *Anticancer Research*, 2008.

[144] D. L. Morton, D. R. Wen, J. H. Wong, J. S. Economou, L. A. Cagle, F. K. Storm, L. J. Foshag and A. J. Cochran, "Technical Details of Intraoperative Lymphatic Mapping for Early Stage Melanoma," *Archives of Surgery*, 1992.

[145] M. E. Casey and R. Nutt, "A multicrystal two dimensional bgo detector system for positron emission tomography," *IEEE Transactions on Nuclear Science*, 1986.

[146] H. Ishibashi, K. Shimizu, K. Susa and S. Kubota, "Cerium doped gso scintillators and its application to position sensitive detectors," *IEEE Transactions on Nuclear Science,* 1989.

[147] E. V. Van Loef, P. Dorenbos, C. W. Van Eijk, K. Krämer and H. U. Güdel, "High-energy-resolution scintillator: Ce3+ activated LaBr3," *Applied Physics Letters,* 2001.

[148] J. Weidner, "Physics and Chemistry of Luminescent Materials: Proceedings of The...," 1999.

[149] E. N. Itikawa, L. A. Santos, A. C. Trevisan, F. A. Pitella, M. Kato, E. R. Moraes and L. Wichert-Ana, "Characterization of resolution, sensitivity, and shielding of a gamma-probe for sentinel lymph node localization: An experimental study," *Nuclear Medicine Communications,* 2017.

[150] D. Hellingman and S. Vidal-Sicart, "The Use of Intraoperative Small and Large Field of View Gamma Cameras for Radioguided Surgery," in *Radioguided Surgery,* 2016.

[151] R. A. Valdés Olmos, L. Vermeeren, W. M. Klop, M. W. Van Den Brekel, A. J. Balm and O. E. Nieweg, *Sentinel node detection in head and neck malignancies: Innovations in radioguided surgery,* 2009.

[152] C. Mathelin, S. Salvador, D. Huss and J.-L. Guyonnet, "Precise localization of sentinel lymph nodes and estimation of their depth using a prototype intraoperative mini gamma-camera in patients with breast cancer.," *Journal of nuclear medicine : official publication, Society of Nuclear Medicine,* vol. 48, no. 4, pp. 623-9, 4 2007.

[153] C. Mathelin, S. Salvador, S. Croce, N. Andriamisandratsoa, D. Huss and J. L. Guyonnet, "Optimization of sentinel lymph node biopsy in breast cancer using an operative gamma camera," *World Journal of Surgical Oncology,* 2007.

[154] J. Ortega, J. Ferrer-Rebolleda, N. Cassinello and S. Lledo, "Potential role of a new hand-held miniature gamma camera in performing minimally invasive parathyroidectomy.," *European journal of nuclear medicine and molecular imaging,* vol. 34, no. 2, pp. 165-9, 2 2007.

[155] S. L. Bugby, J. E. Lees, B. S. Bhatia and A. C. Perkins, "Characterisation of a high resolution small field of view portable gamma camera.," *Physica medica : PM : an international journal devoted to the applications of physics to medicine and biology : official journal of the Italian Association of Biomedical Physics (AIFB),* vol. 30, no. 3, pp. 331-9, 5 2014.

[156] P. Knoll, S. Mirzaei, K. Schwenkenbecher and T. Barthel, "Performance Evaluation of a Solid-State Detector Based Handheld Gamma Camera System," 2014.

[157] N. C. Hall, R. L. Plews, A. Agrawal, S. P. Povoski, C. L. Wright, J. Zhang, E. W. Martin and J. Phay, "Intraoperative scintigraphy using a large field-of-view portable gamma camera for primary hyperparathyroidism: initial experience.," *BioMed research international*, vol. 2015, p. 930575, 2015.

[158] A. Abe, N. Takahashi, J. Lee, T. Oka, K. Shizukuishi, T. Kikuchi, T. Inoue, M. Jimbo, H. Ryuo and C. Bickel, "Performance evaluation of a hand-held, semiconductor (CdZnTe)-based gamma camera.," *European journal of nuclear medicine and molecular imaging*, vol. 30, no. 6, pp. 805-11, 6 2003.

[159] J. N. Aarsvod, C. M. Greene, R. A. Mintzer, S. F. Grant, T. M. Styblo, N. P. Alazraki, B. E. Patt, G. M. Caravaglia, J. Li and J. S. Iwanczyk, "Intraoperative gamma imaging of axillary sentinel lymph nodes in breast cancer patients.," *Physica medica : PM : an international journal devoted to the applications of physics to medicine and biology : official journal of the Italian Association of Biomedical Physics (AIFB)*, vol. 21 Suppl 1, pp. 76-9, 2006.

[160] A. Bartolazzi, C. D'Alessandria, M. G. Parisella, A. Signore, F. Del Prete, L. Lavra, S. Braesch-Andersen, R. Massari, C. Trotta, A. Soluri, S. Sciacchitano and F. Scopinaro, "Thyroid cancer imaging in vivo by targeting the anti-apoptotic molecule galectin-3," *PLoS ONE*, 2008.

[161] D. Kopelman, I. Blevis, G. Iosilevsky, A. Reznik, A. Chaikov, N. Weiner, O. Israel and M. Hashmonai, "A newly developed intra-operative gamma camera: performance characteristics in a laboratory phantom study.," *European journal of nuclear medicine and molecular imaging*, vol. 32, no. 10, pp. 1217-24, 10 2005.

[162] D. Kopelman, I. Blevis, G. Iosilevsky, O. A. Hatoum, A. Zaretzki, R. Shofti, T. Salmon, O. Israel and M. Hashmonai, "Sentinel node detection in an animal study: evaluation of a new portable gamma camera.," *International surgery*, vol. 92, no. 3, pp. 161-6.

[163] A. Ferretti, S. Chondrogiannis, A. Marcolongo and D. Rubello, "Phantom study of a new hand-held γ-imaging probe for radio-guided surgery.," *Nuclear medicine communications*, vol. 34, no. 1, pp. 86-90, 1 2013.

[164] P. Russo, G. Mettivier, R. Pani, R. Pellegrini, M. N. Cinti and P. Bennati, "Imaging performance comparison between a LaBr3: Ce scintillator based and a CdTe semiconductor based photon counting compact gamma camera.," *Medical physics*, vol. 36, no. 4, pp. 1298-317, 4 2009.

[165] P. Russo, A. S. Curion, G. Mettivier, M. Esposito, M. Aurilio, C. Caracò, L. Aloj and S. Lastoria, "Evaluation of a CdTe semiconductor based compact γ camera for sentinel lymph node imaging.," *Medical physics,* vol. 38, no. 3, pp. 1547-60, 3 2011.

[166] P. Olcott, F. Habte, C. Levin and A. Foudray, "Characterization of performance of a miniature, high sensitivity gamma ray camera," 2005.

[167] L. Menard, Y. Charon, M. Solal, P. Laniece, R. Mastrippolito, L. Pinot, L. Ploux, M. Ricard and L. Valentin, "POCI: a compact high resolution γ camera for intra-operative surgical use," *IEEE Transactions on Nuclear Science,* 1998.

[168] S. Pitre, L. Ménard, M. Ricard, M. Solal, J.-R. Garbay and Y. Charon, "A hand-held imaging probe for radio-guided surgery: physical performance and preliminary clinical experience.," *European journal of nuclear medicine and molecular imaging,* vol. 30, no. 3, pp. 339-43, 3 2003.

[169] F. Sánchez, J. M. Benlloch, B. Escat, N. Pavón, E. Porras, D. Kadi-Hanifi, J. A. Ruiz, F. J. Mora and A. Sebastià, "Design and tests of a portable mini gamma camera.," *Medical physics,* vol. 31, no. 6, pp. 1384-97, 6 2004.

[170] M. Tsuchimochi, H. Sakahara, K. Hayama, M. Funaki, R. Ohno, T. Shirahata, T. Orskaug, G. Maehlum, K. Yoshioka and E. Nygard, "A prototype small CdTe gamma camera for radioguided surgery and other imaging applications.," *European journal of nuclear medicine and molecular imaging,* vol. 30, no. 12, pp. 1605-14, 12 2003.

[171] M. Tsuchimochi, K. Hayama, T. Oda, M. Togashi and H. Sakahara, "Evaluation of the efficacy of a small CdTe gamma-camera for sentinel lymph node biopsy.," *Journal of nuclear medicine : official publication, Society of Nuclear Medicine,* vol. 49, no. 6, pp. 956-62, 6 2008.

[172] T. Oda, K. Hayama and M. Tsuchimochi, "[Evaluation of small semiconductor gamma camera--simulation of sentinel lymph node biopsy by using a trial product of clinical type gamma camera].," *Kaku igaku. The Japanese journal of nuclear medicine,* vol. 46, no. 1, pp. 1-12, 3 2009.

[173] L. R. MacDonald, B. E. Patt, J. S. Iwanczyk, Y. Yamaguchi, D. P. McElroy, E. J. Hoffman, J. N. Aarsvold, R. A. Mintzer and N. P. Alazraki, "High-resolution hand-held gamma camera," in *Penetrating Radiation Systems and Applications II,* 2003.

[174] B. Minkov, "Promising new Lutetium based single crystals for fast scintillators.," *Functional materials. 1.* , pp. 103-105, 1994.

[175] G. Blasse and B. C. Grabmaier, "A General Introduction to Luminescent Materials," in *Luminescent Materials*, Berlin, Heidelberg, Springer Berlin Heidelberg, 1994, pp. 1-9.

[176] C. Greskovich and S. Duclos, "CERAMIC SCINTILLATORS," *Annual Review of Materials Science*, 2002.

[177] P. Guss, M. Reed, D. Yuan, M. Cutler, C. Contreras and D. Beller, "Comparison of CeBr 3 with LaBr 3 :Ce, LaCl 3 :Ce, and NaI:Tl detectors," 2010.

[178] U. Happek, S. A. Basun, J. Choi, J. K. Krebs and M. Raukas, "Electron transfer processes in rare earth doped insulators," *Journal of Alloys and Compounds*, 2000.

[179] R. Hupke, "The new UFC detector for CT imaging," *RBM - Revue Europeenne de Technologie Biomedicale*, 1998.

[180] J. S. Karp and M. E. Daube-Witherspoon, "Depth-of-interaction determination in NaI(Tl) and BGO scintillation crystals using a temperature gradient," *Nuclear Inst. and Methods in Physics Research, A*, 1987.

[181] C. Melcher, M. Schmand, M. Eriksson, L. Eriksson, M. Casey, R. Nutt, J. Lefaucheur and B. Chai, "Scintillation properties of LSO:Ce boules," *IEEE Transactions on Nuclear Science*, 2000.

[182] N. Miura, "Phosphors for X-ray and ionizing radiation," in *Phosphor Handbook*, CRC Press, 2006.

[183] W. W. Moses, S. E. Derenzo, A. Fyodorov, M. Korzhik, A. Gektin, B. Minkov and V. Aslanov, "LuAlO3:Ce – A HIGH DENSITY, HIGH SPEED SCINTILLATOR FOR GAMMA DETECTION," *IEEE Transactions on Nuclear Science*, 1995.

[184] A. Saoudi and R. Lecomte, "A novel apd-based detector module for multi-modality pet/spect/ct scanners," *IEEE Transactions on Nuclear Science*, 1999.

[185] E. Browne and J. K. Tuli, "Nuclear Data Sheets for A = 99," *Nuclear Data Sheets*, vol. 145, pp. 25-340, 1 11 2017.

[186] S. Ohya, "Nuclear data sheets for A = 123," *Nuclear Data Sheets*, vol. 102, no. 3, pp. 547-718, 2004.

[187] Eckert&Zigler Isotope Products, "Certification of Calibration Cd-109 Standard Source," Valencia, California, 2014.

[188] Eckert&Zigler Isotope Products, "Certificate of Calibration Gamma Standard Source Co-57," Valencia, California, 2014.

[189] Sanchez, F; Fernandez, M M; Gimenez, M; Benlloch, J M; Rodriguez-Alvarez, M J; Garcia de Quiros, F; Lerche, C h W; Pavon, N; Palazon, J A; Martinez, J; Sebastia, A, "Performance tests of two portable mini gamma cameras for medical applications," *Medical Physics*, 2006.

[190] K. S. Shah, R. Farrell, R. Grazioso, Y. Shao and S. R. and Cherry, "APD arrays for medical imaging," in *6th Int. Conf. on Inorganic Scintillators and their use in Scientific and Industrial Applications SCINT2001*, Chamonix, France, 2001.

[191] P. Dorenbos, C. Van't Spijker J and C. Van Eijk, "Luminescence and scintillation mechanisms inCe3+ activated Gd-compounds Proc," in *Int.Conf.on Inorganic Scintillators and their Applications SCINT97*, Shanghai.

[192] Yamada, H;Susuk,i A; Uchida,; Yoshida, M.Y., "A scintillator Gd sub 2 O sub 2 S:Pr, Ce, F for x-ray computed tomography," 1989.

[193] Rossner, W; Ostertag, M; Jermann, F., "Properties and applications of gadolinium oxysulfide based ceramic scintillators," *Electrochem. Soc. Proc*, pp. 98-24 187–94, 1999.

[194] W. Rossner and M. Ostertag, "Properties and Application of Gadolinium Oxysulfide Based Ceramic Scintillators," in *MEETING ABSTRACTS-ELECTROCHEMICAL SOCIETY -ALL DIVISIONS*, Boston; MA, 1998.

[195] C. Dujardin, A. Garcia-Murillo, C. P´edrini, C. Madej, C. Goutaudier, A. Koch, A. G. Petrosyan, K. L. Ovanesyan, G. O. Shirinyan and M. Weber, "Synthesis and scintillation properties of somedende x-ray phosphors," Moscow: M V Lomonosov Moscow State University, 2000.

[196] A. Lempicki, C. Brecher, H. Lingertat, P. Szupryczynski, V. V. Nagarkar, S. V. pnis and S. R. Miller, "A new scintillator for digital x-ray radiography," in *Book of abstracts of the 6th Int. Conf. on Inorganic Scintillators and Their usein Scientific and Industrial Applications SCINT2001*, Chamonix, France, 2001.

[197] E. V. Van Loef, P. Dorenbos, C. W. Van Eijk, K. Krämer and H. U. Güdel, "High-energy-resolution scintillator: Ce3+ activated LaBr3," *Applied Physics Letters*, 2000.

Appendix A

Table A. 1 Informational data of the sources used in the experiments and MCNP simulations.

Single Nuclide Sources									
Nuclide	**Half Life $t1_{/2}$ (h)**	**Uncertainty in Half Life (h)**	**Source ID**	**Energy (keV)**	**Activity (A_0) (Bq)**	**Reference A_0 date**	**Branching Ratio**	**Total Uncertainty in the Activity**	**Exp Evaluation**
^{09}Cd	1.11E+04	16.8	048-88-1	88	3.61E+05	2/15/2019 2:00 PM UTC	0.0363	3.00%	ES[a,] ER[b],PE[d]
^{7}Co	6.52E+03	2.16	048-88-12	122	3.86E+05	2/15/2019 2:00 PM UTC	0.856	3.00%	ES[a],ER[b], DM[c] PE[d]
^{9m}Tc	6.01E+00	0.0001	n/a	141	1.74E+08	2/16/2019 2:12 PM UTC	0.89	4.00%	MC,ES[a], ER[b]
^{23}I	1.32E+01	1.9	n/a	159	8.58E+06	2/16/2019 11:47 AM UTC	0.833	4.00%	MC,ES[a], ER[b],PE[d]
^{37}Cs (Seed)	2.64E+05	1402.368	n/a	662	7.08E+07	4/1/2005 12:00 PM UTC	0.851	4.00%	MC,ES[a], ER[b],PE[d]
Multi-Nuclide Source									
^{10}Pb	1.96E+05	1752.96	1592-24	47	9.34E+04	5/1/2012 2:00 PM UTC	0.0418	4.10%	ES[a]
^{09}Cd	1.11E+04	16.8	1592-24	88	1.19E+05	5/1/2012 2:00 PM UTC	0.0363	3.10%	ES[a]
^{37}Cs	2.64E+05	1402.368	1592-24	662	2.06E+04	5/1/2012 2:00 PM UTC	0.851	3.00%	MC,ES[a],PE[d]
^{0}Co	4.62E+04	8.76	1592-24	1173	2.44E+04	5/1/2012 2:00 PM UTC	0.9986	3.00%	MC,ES[a],PE[d]
^{0}Co	4.62E+04	8.76	1592-24	1333	2.44E+04	5/1/2012 2:00 PM UTC	0.9998	3.00%	MC,ES[a],PE[d]

n/a: Not applicable, or missing information
[a] Energy Spectrum,
[b] Energy Resolution,
[c] Distance Measurements,
[d] PhotoPeak Efficiency
MC: Monte Carlo Simulations

Appendix B

Table B.1 The parameters contributed to the total % standard uncertainty in the % energy resolution for experimental calculations.

Component	**E=88 kev**		**E=122 keV**		**E=159 keV**		**E=662 keV**		**E=1173 keV**		**E=1333 keV**	
	Type A %	Type B %	Type A %	Type B %	Type A %	Type B %	Type A %	Type B %	Type A %	Type B %	Type A %	Type B %
Count statistics and Dead-time provided by MCA	1.2		4.5		3.8		1.5		16.7		30.9	
Quadratic Sum	1.2	0.0	4.5	0.0	3.8	0.0	1.5	0.0	16.7	0.0	30.9	0.0
Combined Uncertainty %	**1.2**		**4.5**		**3.8**		**1.5**		**16.7**		**30.9**	

Table B.2 The parameters contributed to the total % standard uncertainty in experimental photopeak efficiency calculations.

Component	**E=88 kev**		**E=122 keV**		**E=159 keV**		**E=662 keV**		**E=1173 keV**		**E=1333 keV**	
	Type A %	Type B %	Type A %	Type B %	Type A %	Type B %	Type A %	Type B %	Type A %	Type B %	Type A %	Type B %
Activity		3.1		3.0		3.0		3.0		3.0		3.0
Half Life		0.2		0.0		0.0		0.5		0.0		0.0
Distance		3.0		3.0		3.0		3.0		3.0		3.0
MCA (Count Statistics and dead time)	4.9		0.9		0.2		6.2		22.6		13.8	
Quadratic Sum	4.9	4.3	0.9	4.2	0.2	4.2	6.2	4.3	22.6	4.2	13.8	4.2
Combined Uncertainty %	**6.5**		**4.3**		**4.2**		**7.6**		**23.0**		**14.4**	

Table B.3 The parameters contributed to the total % standard uncertainty in the net count rate detected for distance measurements for experimental calculations.

Component	**SDD=1cm**		**SDD=3 cm**		**SDD=5 cm**		**SDD=7 cm**		**SDD=15 cm**		**SDD=20 cm**	
	Type A %	Type B %	Type A %	Type B %	Type A %	Type B %	Type A %	Type B %	Type A %	Type B %	Type A %	Type B %
Activity		3.0		3.0		3.0		3.0		3.0		3.0
Half Life		0.0		0.0		0.0		0.0		0.0		0.0
Distance		7.0		5.0		3.0		2.1		1.0		0.8
MCA (Count Statistics and dead time)	0.3		0.5		0.9		1.3		3.9		5.9	
Quadratic Sum	0.3	7.6	0.5	5.8	0.9	4.2	1.3	3.7	3.9	3.2	5.9	3.1
Combined Uncertainty %	**7.6**		**5.9**		**4.3**		**3.9**		**5.0**		**6.7**	